THE INFLUENCE OF BLAST FURNACE SLAG AS A FUNCTIONAL FILLER ON POLYPROPYLENE COMPOUNDS

by

ABDELHAMID MOSTAFA

A Dissertation in Candidacy for the Degree of Doktor der montanistischen Wissenschaften

Montanuniversitaet Leoben
Department of Polymer Engineering and Science

Chair of Polymer Processing
Head: Prof. Dr. Clemens Holzer

June 2017

AFFIDAVIT

I declare on lieu of oath, that I wrote this thesis and performed the associated research myself, using only literature cited in this volume.

_____ _____

Datum Unterschrift

Acknowledgements

I am grateful to the support, facilities and encouragement of the Polymer Competence Center Leoben GmbH (PCCL), the Chair of Polymer Processing, the Chair of Mineral processing, the Chair of Chemistry of Polymers and the Chair of Material Science and Testing of Polymers, Montanuniversitaet Leoben (MUL). I would like to express my gratitude to our industrial partner, company voestalpine Stahl GmbH, Austria for the great support and funding of this research. This dissertation was accomplished within the framework of a three-year project titled “Blast Furnace and Steel Slags as Functional Fillers for Thermoplastics – Polyslag”, funded by the FFG-Bridge program.

My special gratitude goes to Mr. Univ.-Prof. Dipl.-Ing. Dr.mont. Clemens Holzer, Head of Chair of Polymer Processing (LKV-MUL), for the encouragement and mentoring, guidance and instructive discussions along this journey.

I want to acknowledge the valuable support of Mr. Mag. Martin Payer MBA, Mr. Assoz.Prof. Dipl.-Ing. Dr.mont. Thomas Lucyshyn, Head of the injection molding and compounding group (LKV-MUL). My gratitude goes to Mr. Dipl,-Ing Dr.mont. Gernot Pacher and Mr. Dipl.-Ing Dr.mont. Stephan Laske, the present- and former ‘Polyslag’ project leaders, PCCL, for their valuable collaboration and insightful discussions. I would also like to thank Univ.-Prof. Dipl.-Ing. Dr.mont. Helmut Flachberger and Ass.Prof. Dipl.-Chem. Dr.rer.nat. Gisbert Rieß for their valuable guidance and support.

I am thankful to Mr. Dipl.-Ing. Dr.mont. Ivica Duretek, Mr. Ing. Rudolf Schatzer, Ms. Sabrina Winkler, Mr. Mag. Dr.rer.net Thomas Ules, Ms. MSc. Andrea Wanner, Ms. Astrid Rauschenbach, Mrs. DI Bettina Ottersböck, Ms. MSc. Dr. tech. Sandra Pötz, Mr. Herbert Fladenhofer, Mr. Dipl.-Ing. Dr.mont. Florian Arbeiter, Mr. Bernd Haar, Mr. DDI Matthias Katschnig and Mr. Robert Hinterberger for their kind cooperation.

My first and foremost gratitude goes to my wife Mrs. Ghadeer Omar, my soul mate and everlasting source of unconditional love, support and encouragement. I am always indebted to my parents’ love and moral support.

Leoben, 2017

Abdelhamid Mostafa

To Ghadeer and Farida

June 2017

Abstract

Blast furnace slag (BFS) is a secondary byproduct of the steel industry. When appropriately tailored, BFS could be an effective functional filler that improves the property profile of widely-applied thermoplastics like polypropylene (PP). This work proposes BFS as tailored filler, which might provide a functional influence on the structure-property profile of PP beyond just being an inexpensive filler material compared to the common commercial fillers in the polymer industry such as calcium carbonate. Furthermore, the possibility to reach promising functional performance for BFS could be a valuable step toward saving significant amounts of energy, that are otherwise devoted to the extraction and processing of commercially utilized mineral fillers such as calcium carbonate. Hence, the main target of the current PhD thesis was to investigate the influence of BFS as a functional filler on the rheological, thermal and mechanical properties of a typical PP copolymer.

This research was systematically divided into basic and advanced stages. In the basic stage, the investigation of the influence of BFS filler parameters (distribution, type and loading), kneading process parameters (speed and duration) and compounding technique (kneading versus TSC) on the properties of PP was accomplished. With the evolution of the ‘basic study’ findings, the number of the investigated BFS filled PP compounds was reduced to only two compounds. For each compound, two coupling agents, VES and MPS were compared with respect to the compound properties, where the coupling agent reflecting better compound properties was selected. To produce the final BFS – PP compounds, the better coupling agent, MPS, was hence utilized to modify the BFS for TSC compounding runs followed by subsequent compression-/ injection molding. Based on their properties, the final BFS - PP compounds were investigated for candidacy in automotive interior trim applications. Therefore, the properties of the final BFS - PP compounds were compared with a compression-/ injection molded commercial compound that is industrially applicable for interior trim applications. As a final step, carbon footprint screening analyses were carried out to compare the environmental life cycle impact of the BFS – PP compounds to a conventional limestone – PP one.

The investigation of unmodified BFS filled PP compounds showed that their complex shear viscosity and tensile stiffness linearly increased up to 35 and 20 % at BFS loading of 30 wt.-%, respectively. The degree of crystallinity, however, showed a linear decrease up to 40 % as the BFS loading increased. At 20 wt.-% loading, it was noticed that BFS increased the thermal conductivity of PP by 40 – 50 %. The twin-screw compounding and injection molding of the modified-BFS with PP surprisingly increased the strain at break of PP beyond 350 %. That was not possible with unmodified BFS, where premature failure was dominant. After testing their candidacy for interior-trim applications, the BFS compounds achieved 800 % higher strain at break as well as comparable tensile stiffness and toughness levels compared to a commercial mineral filled PP compound that is tailor-made for interior-trim applications. Finally, the carbon footprint screening analyses suggested a ‘best for slag’ scenario, where one ton of unmodified-BFS filled PP compound was shown to generate a little less CO_2 than its limestone filled PP counterpart. It is important, however, to emphasize that while limestone was modified and compounding-ready, the BFS was not. Accordingly, the modification process for BFS is expected to emit extra CO_2 into the atmosphere, which might move the BFS toward the ‘50,50’ scenario.

Kurzfassung

Hochofenschlacke (BFS) ist ein sekundäres Nebenprodukt der Stahlindustrie und besteht aus einer Kombination aus sauren und basischen Oxiden. Gezielt modifizierte Hochofenschlacken zeigen großes Potential, das Eigenschaftsprofil thermoplastischer Kunststoffe wie beispielsweise Polypropylen (PP) deutlich zu verbessern. Im Rahmen dieser Arbeit wurde ein BFS-Füllstoff entwickelt, welcher darüber hinaus eine Reduktion der Produktionskosten erlaubt, da BFS in großen Mengen verfügbar ist. Die Möglichkeit des Einsatzes zur Verbesserung des Eigenschaftsprofils bietet gegenüber herkömmlichen mineralischen Füllstoffen den Vorteil, dass große Mengen an Energie eingespart werden können, da Abbau und Aufbereitung entfallen. Daher war die Untersuchung des Einflusses zweier BFS-Typen auf rheologische, thermische und mechanische Eigenschaften eines PP-Copolymers das Hauptziel dieser Arbeit.

Dabei wurden im Rahmen von systematischen Experimenten BFS Partikel im Mikro-Maßstab modifiziert und mittels eines Labormesskneters in die Thermoplastschmelze eingebracht. Nach grundlegenden Untersuchungen wurden zwei BFS-PP Rezepturen ausgewählt, durch einen Doppelschneckencompounder gemischt, formgepresst und spritzgegossen. Basierend auf ihren mechanischen Eigenschaften könnten BFS-PP Compounds vermutlich im Automotive-Bereich als Innenaustattungsmaterial zum Einsatz kommen. Dazu wurden die BFS-PP Rezepturen mit einem industriellen Compound im Rahmen der rheologischen, thermischen und mechanischen Eigenschaften verglichen. Außerdem wurde eine CO_2-Fußabdruckanalyse durchgeführt. Hierzu wurde der ökologische CO_2-Fußabdruck eines repräsentativen BFS-PP Produkts bewertet und mit einem Kreide-PP Compound vergleichen wurde.

Die Untersuchung von den unmodifizierten BFS-PP Compounds zeigte, dass bei 30 Gew.-% BFS-Anteil die komplexe Scherviskosität um 35 % und die Zugsteifigkeit fast linear bis zu 20 % anstieg. Der Kristallinitätsgrad zeigte eine lineare Abnahme bis zu 40 % mit Erhöhung der Füllmenge. Bei einer Füllmenge von 20 Gew.-%, erhöhte BFS die Wärmeleitfähigkeit von PP um ca. 40 – 50 %. Das Doppelschneckencompoundieren und Spritzgießen des modifizierten BFS mit PP erhöhten die Bruchdehnung des PP um über 350 %. Das war durch die Nutzung des unmodifizierten BFS Füllstoff nicht möglich, da frühzeitiger Bruch stattfand. Nach der

Prüfung ihrer Verwendbarkeit für automobile Innenraumanwendungen, erreichten die BFS-PP ca. 800 % Bruchdehnungszunahme sowie vergleichbare Zugsteifigkeit und Zähigkeitsniveaus wie ein industriell mineralgefüllter PP Compound, welcher für automobile Innenraumanwendungen benutzt wird. Schließlich schlug die ökologische CO_2-Fußabdruckanalyse ein ‚best for slag' Szenario vor, wo ein Tonne von unmodifiziertem BFS-PP Compound etwas weniger CO_2 als sein Kreide-PP vergleichbares Pendant erzeugt hat. Es ist jedoch wichtig zu betonen, dass BFS nicht wie Kreide bereits modifiziert und zur Compoundierung als Füllstoff bereit liegt. Folglich ist zu erwarten, dass der Modifizierungsvorgang von BFS zusätzlich CO_2 produziert, was die Hochofenschlacke in Richtung ‚50:50' Szenario verschieben könnte.

Publications

Peer-reviewed journal publications:

[1] Mostafa, A., G. Pacher, Lucyshyn T., Holzer, C., E. Krischey, W. Oefner, and Fritz, B. Laske, S. 2017. “Influence of melt compounding on blast furnace slag filled PP compounds: A comparative study.” Int. Polym. Process. Accepted Manuscript

[2] Mostafa, A., S. Laske, G. Pacher, C. Holzer, H. Flachberger, E. Krischey, and B. Fritz. 2016. “Blast furnace slags as functional fillers on rheological, thermal, and mechanical behavior of thermoplastics.” J. Appl. Polym. Sci. 133 (8). doi:10.1002/app.43021.

Conference and other scientific-event publications:

[1] Geissler, B., A. Mostafa, A. Uray, S. Laske, C. Holzer, and G. R. Langecker, eds. 2013. Influence of Chain Extender on the Foaming Behavior and on the Mechanical Properties of Physically Foamed PLA: Article. AIP Conference Proceedings Volume 1593: PPS-29. Nuremberg, Germany.

[2] Mostafa, A., B. Geissler, A. Uray, S. Laske, C. Holzer, and G. R. Langecker, eds. 2013. Influence of Chain Extender on the Foaming Behavior and on the Mechanical Properties of Physically Foamed PLA: Poster. AIP Conference Proceedings Volume 1593: PPS-29. Nuremberg, Germany.

[3] Mostafa, A., G. Pacher, Lucyshyn T., Holzer, C., E. Krischey, W. Oefner, and Fritz, B. Laske, S, eds. 2017. Influence of Compounding Technology on Rheological, Thermal and Mechanical Behavior of Blast Furnace Slag Filled Polystyrene Compounds: Peer-reviewed, Accepted Manuscript. PPS 32, Lyon, Austria.

[4] Mostafa, A., G. Pacher, Lucyshyn T., Holzer, C., E. Krischey, W. Oefner, and Fritz, B. Laske, S, eds. 2017. Influence of Compounding Technology on Rheological, Thermal and Mechanical Behavior of Blast Furnace Slag Filled Polystyrene Compounds: Peer-reviewed, Accepted Manuscript. PPS 32, Lyon, Austria.

[5] Mostafa, A., G. Pacher, Lucyshyn T., Holzer, C., H. Flachberger, W. Oefner, and Fritz, B. Laske, S, eds. 2016. Influence of Kneading Parameters on

Thermal/Mechanical Behavior of Blast Furnace Slag Filled PP Compounds: Poster: 25. Leobener Kunststoff-colloquium, Leoben, Austria.

[6] Mostafa, A., S. Laske, C. Holzer, and E. Krischey, eds. 2015. Influence of Filler Type, Size and Concentration on Rheological and Thermal Behavior of Polypropylene/Blast furnace Slag Compounds: Article. SPE ANTEC Proceedings: SPE ANTEC, Orlando, USA.

[7] Mostafa, A., S. Laske, C. Holzer, H. Flachberger, E. Krischey, and B. Fritz, eds. 2015. Assessment of Compounding Approach upon Rheological, Thermal and Mechanical Behavior of Polypropylene Filled with Blast Furnace Slag: Presentation. PPS 2015, Graz, Austria.

[8] Mostafa, A., S. Laske, C. Holzer, H. Flachberger, E. Krischey, and B. Fritz, eds. 2015. Influence of Filler Type, Size and Concentration on Rheological and Thermal Behavior of Polypropylene/Blast furnace Slag Compounds: Article. 8th European Slag Conference Proceedings: 8th European Slag Conference. www.euroslag.com.

[9] Mostafa, A., S. Laske, I. Duretek, N. Krempl, C. Holzer, A. Brandstaetter, and A. Hoellebauer, eds. 2015. Influence of Chain Extender and Impact Modifier on Rheological and Mechanical Performance of Multilayer PLA films: Presentation. DVS Polymer Meeting, Gmunden, Austria.

Table of Contents

Introduction

1.1 Concepts and definitions

1.1.1 Polymers

The term ‘polymer’ is derived from the combination of the ancient Greek words *πολύς*, pronounced ‘polus’ and means ‘many or much’ and *μέρος*, pronounced ‘meros’ and means ‘parts’. A polymer is a large macromolecule composed of multiples of smaller, repeated subunits with much lower molecular mass, called ‘monomers’. These subunits are combined with each other by means of covalent chemical bonds. Compared to monomers, the considerably high molecular mass of polymers is responsible for their unique physical properties such as viscoelasticity and toughness as well as their tendency to form semicrystalline and glassy structures [78]; [12]. Polymers may be categorized based on the following aspects:

Source: Polymers can be grouped by source into natural and synthetic. From their name, natural polymers are obtained by nature and are originally found in plants and animals. Examples of natural polymers are cellulose, starch, proteins and natural rubber. Synthetic polymers are man-made polymers, synthesized in the laboratory by means of a complicated chemical process called ‘polymerization’. Examples of synthetic polymers are polyethylene, polypropylene and polyvinylchloride [67]; [9].

Backbone of polymer chain: Polymers can be categorized as organic or inorganic. An organic polymer, such as most synthetic polymers, is a polymer whose backbone chain is essentially composed of carbon atoms. Inorganic polymers, such as glass and silicon rubber, have no carbon atoms in their backbone chains [9].

Molecular structure: Polymer molecular structures are classified as linear, branched or cross-linked. Linear polymers, such as high density polyethylene, typically consist of long, straight chains with minimal branches. On the other hand, branched polymers, such as low density polyethylene, consist of linear chains that are heavily branched with small sub-chains. Cross-linked type, such as vulcanized rubber and thermosets form a strong network of covalent bonds among the polymer chains [9].

Composition: Polymers can be categorized into homopolymers and copolymers. A homopolymer results from the polymerization of a repeated unit of a single monomer type. A copolymer, or a heteropolymer, is a polymer synthesized via 'copolymerization' of two (or more) monomeric species. Copolymers could be further grouped into alternating-, block-, random- or graft copolymers. Commercially relevant copolymers include acrylonitrile butadiene styrene and styrene-acrylonitrile [9]. Random- and block PP copolymers will be discussed in more detail later in this work.

Polymerization mode: Polymers may be categorized into addition and condensation polymers. Addition polymers are formed via addition polymerization, where the polymer is produced via the addition of monomer molecules possessing double or triple bonds, an example is the polymerization of polypropylene from propylene monomer. Condensation polymers, on the other hand, are formed via condensation polymerization process, where the polymer is produced via a repeated condensation reaction between bi-functional and tri-functional monomer units, resulting into elimination of small molecules like water. One example of condensation polymers is polyamides [9].

1.1.2 Composite materials

A 'composite material' is a material consisting of two or more constituent materials that are different in structure as well as physical and chemical properties. As the constituent materials are combined together, the formed composite has distinctive characteristics that are different from its constituents. The individual components, however, preserve their own characteristics and do not dissolve or blend into each other, but may rather physically and/or chemically interact with each other within the composite structure. A composite is usually preferred over the neat polymer as the former can be tailored to reflect better rheological, thermal, electrical and mechanical properties compared to the neat polymer [17].

1.1.3 Polymer composites

Polymer composites are multiphase systems, where one or more additives, which usually termed 'filler' or 'reinforcer' according to the application, are incorporated into the continuous polymer matrix. The resulting multiphase system has a unique structure-property profile. Additives are incorporated into the polymer system to induce

property enhancement or modification, decrease overall cost of the composite, or improve/control the processing behavior [107]. The properties of polymer composites are primarily affected by the following interconnected parameters:

- Additive morphology
- Size distribution
- Aspect ratio
- Inherent properties of the additive and matrix such as physical, chemical, mechanical, thermal, electrical and optical properties
- Composite composition and filler loading
- The interaction between different components within the composite system
- The fabrication method of the composite

1.1.4 Functional fillers

The correlation between the terms ‘additives’ and ‘fillers’ has been reported in literature in different ways. For instance, Xanthos [107] noted that “traditionally, most fillers were considered as additives, which, because of their unfavorable geometrical features, surface area, or surface chemical composition, could only moderately increase the modulus of the polymer, whereas strength (tensile, flexural) remained unchanged or even decreased”. Alternatively, plastic additives have been distinguished from plastic fillers in the sense that additives are “typically organic molecules that are added to polymers in small amounts (typically 0.1 – 5.0 wt.-%) during manufacture, processing, or converting so as to improve the inherent properties of the polymer resin.” [57]. According to the last definition, inorganic materials that are incorporated into polymer systems, including minerals, could favorably be categorized as fillers rather than additives, which is the popular terminology that is frequently found in literature.

The term ‘functional filler’ will be systematically associated with BFS throughout this context for two reasons: First, the term ‘functional’ emphasizes that the filler, aside from its polymer-filling and cost-reduction purposes, might positively modify one or more functional properties of the polymer. For instance, mineral fillers such as calcium carbonate do not just have a filling/economic purpose, but rather modify the mechanical properties of the base polymers such as improving its toughness. Second, we will adapt the filler/reinforcement classification criteria reported by Xanthos [107],

where the term ‘filler’ referred to “short, discontinuous fibers, flakes, platelets, or particulates”, while the term ‘reinforcement’, rather described “long, continuous fibers or ribbons”. According to Xanthos [107], functional fillers are usually used in relatively high concentrations (>5 vol.-%) with minor exceptions as coupling agents and processing aids. In addition, functional fillers have diverse chemical structures, forms, sizes, shapes and inherent properties. They are usually solid and rigid materials that are immiscible with the polymer in both molten and solid states. Table 1 shows the functional fillers based on the chemical family of the filler, while Table 2 categorizes them based on their aspect ratios [107].

Table 1: Classification of functional fillers based on their chemical family [107].

Chemical family	Examples
Inorganics	
Oxides	Glass (fibers, spheres, hollow spheres, and flakes), MgO, SiO_2, Sb_2O_3, Al_2O_3, and ZnO
Hydroxides	$Al(OH)_3$ and $Mg(OH)_2$
Salts	$CaCO_3$, $BaSO_4$, $CaSO_4$, phosphates, and hydrotalcite
Silicates	Talc, mica, kaolin, wollastonite, montmorillonite, feldspar, and asbestos
Metals	Boron and steel
Organics	
Carbon, graphite	Carbon fibers, graphite fibers and flakes, carbon nanotubes, and carbon black
Natural polymers	Cellulose fibers, wood flour and fibers, flax, cotton, sisal, and starch
Synthetic polymers	Polyamide, polyester, aramid, and polyvinyl alcohol fibers

Table 2: Classification of functional fillers based on their aspect ratios [107].

Shape	Aspect ratio	Example
Cube	1	Feldspar and calcite
Sphere	1	Glass spheres
Block	1–4	Quartz, calcite, silica, and barite
Plate	4–30	Kaolin, talc, and hydrous alumina
Flake	50–200++	Mica, graphite, and montmorillonite nanoclays
Fiber	20–200++	Wollastonite, glass fibers, carbon nanotubes, wood fibers, asbestos fibers, and carbon fibers

1.2 Dissertation statement and goal

The current dissertation provides a systematic, multi-phase investigation of the influence of BFS as a functional filler on the rheological, thermal, mechanical properties of PP. This research shows a step-wise progression from tailored preparation of unmodified-BFS filler up to the injection molding of properly-selected, semi-industrial compounds compounded with tailored- and modified slag functional filler. The target application for the final slag filled compounds is automotive industrial trims. Accordingly, the mechanical properties and ecological impact of the final compound formulations were compared with an existing commercial compound fabricated for the same application.

1.2.1 Scope

The scope of the current research can be defined with respect to the following aspects:

The base polymer

A polypropylene block copolymer grade will be utilized as a base polymer.

The functional filler

The reason behind the investigation of BFS as a functional filler in this dissertation is four-fold:

- First, from a polymer processing viewpoint, the investigation of BFS as a multi-oxide mineral material is attractive. This is because the structure and composition of the mineral BFS filler could principally trigger a functional influence on PP processing-property profile that is comparable to other commercial mineral fillers such as calcium carbonate.
- Secondly, the extensive utilization of mineral fillers such as calcium carbonate and talc might imposes an ecological concern because such fillers are extracted from mines and quarries, which are natural resources that are susceptible to depletion. On the other hand, an extensive amount of blast furnace slag is landfilled world-wide, which is coupled with high energy- and financial burdens as well as negative impact on the environment [21]; [54]; [4].

- Thirdly, extraction of commercial mineral fillers utilizes high amounts of energy that could be otherwise saved if BFS is used in suitable applications.
- Fourthly, fillers in general have often the economic advantage of being much cheaper compared to the polymer itself. This economic aspect is further emphasized with BFS because it is much cheaper in its as-produced, and arguably modified, form compared to other mineral fillers such as calcium carbonate and talc. According to voestalpine Stahl GmbH, the cost of as-produced BFS is about 10-15 Euro/ton, which is almost 8 to 10-fold lower than that of calcium carbonate filler [11].

The following BFS parameters were chosen for the current research:

- Size range and distribution: <71, <40 and <20 μm
- Type: Granulated blast furnace slag (GBS) and air-cooled blast furnace slag (ACBS)
- Filler loading: 10, 20 and 30 wt.-%

The investigated properties

The investigated compound properties within this research are limited to the following properties

- Rheological: Complex shear viscosity, storage- and loss moduli, loss factor and cross over points
- Thermal: Crystallization and thermal temperatures and enthalpies, degree of crystallization and thermal conductivity
- Mechanical (tensile): Stress-strain, tensile stiffness, ultimate- and fracture strength and strains as well as the impact energy (un/-notched at 23 and -30°C)

The compounding equipment

The compounding equipment utilized in this research are:

- Laboratory scale, twin-rotor blade kneader
- Co-rotating, twin screw compounding extruder (TSC)

The post-compounding processing

Post-compounding processing of BFS-filled PP compounds is limited in this research to the following methods:

- Compression molding (utilized in the basic study)
- Injection molding (utilized in the advanced study)

Throughout this research, a minimum of four sample replicates are averaged pro condition, where the mean value and the standard deviation percentages are recorded.

1.2.2 Research originality and hypotheses

Literature research shows that almost no systematic research endeavors on BFS filled PP systems have been found so far. In addition, the current work emphasizes the necessity of producing an application-oriented compound with improved property profile and ecological significance. For the aforementioned reasons, this PhD is claimed novel and original in terms of materials, structure, phases, approach and findings. Examples of hypothetical questions driving the accomplishment of this research work include:

- What is the influence of the BFS particle size range and distribution, type, loading and modification on the following PP properties:
  - complex shear viscosity, storage- and loss moduli
  - degree of crystallinity, crystallization- and melting temperatures
  - thermal conductivity
  - stiffness, strength, ductility and impact energy
- Would the incorporation of BFS filler affect the processability of PP?
- Is it possible for BFS-filled PP compounds to be applied industrially? If yes, what is a typical application for such compounds?
- What is the ecological influence, i.e. carbon footprint, of a typical product based on BFS-filled PP compound?

1.2.3 Methodology

This research utilized a top-down approach starting from a basic study, where a broad range of unmodified-BFS filled compounds were initially investigated. The basic study experiments was accomplished via laboratory-scale processing equipment, such as a

twin rotor blade laboratory kneader and a compression molding machine. This basic study was based on studying the impact of varying both unmodified BFS, kneading and TSC parameters as well as the mixing technique itself (kneading versus TSC) on the structure-property profile of BFS filled PP compounds. In the advanced study, two coupling agents for BFS were selected and compared and one coupling agent was promoted. The finally-selected slag filled compounds and the promoted coupling agent were utilized via TSC-compounding of modified-BFS with PP followed by compression/injection molding of the compounds. The final slag filled compounds were intended for automotive interior trim applications and therefore compared to a commercial, mineral filled PP copolymer compound designed by the company Borealis for this particular application. Finally, a carbon footprint screening of a life cycle assessment study (CFS-LCA) was conducted to investigate the ecological significance of BFS filled PP compound. This was done via comparing the CO_2 emission of 1 t of a BFS filled PP compound with a limestone filled PP one. Figure 1 shows a schematic diagram illustrating the methodology of the current research. Original dissertation time plan is also illustrated in Figure 2.

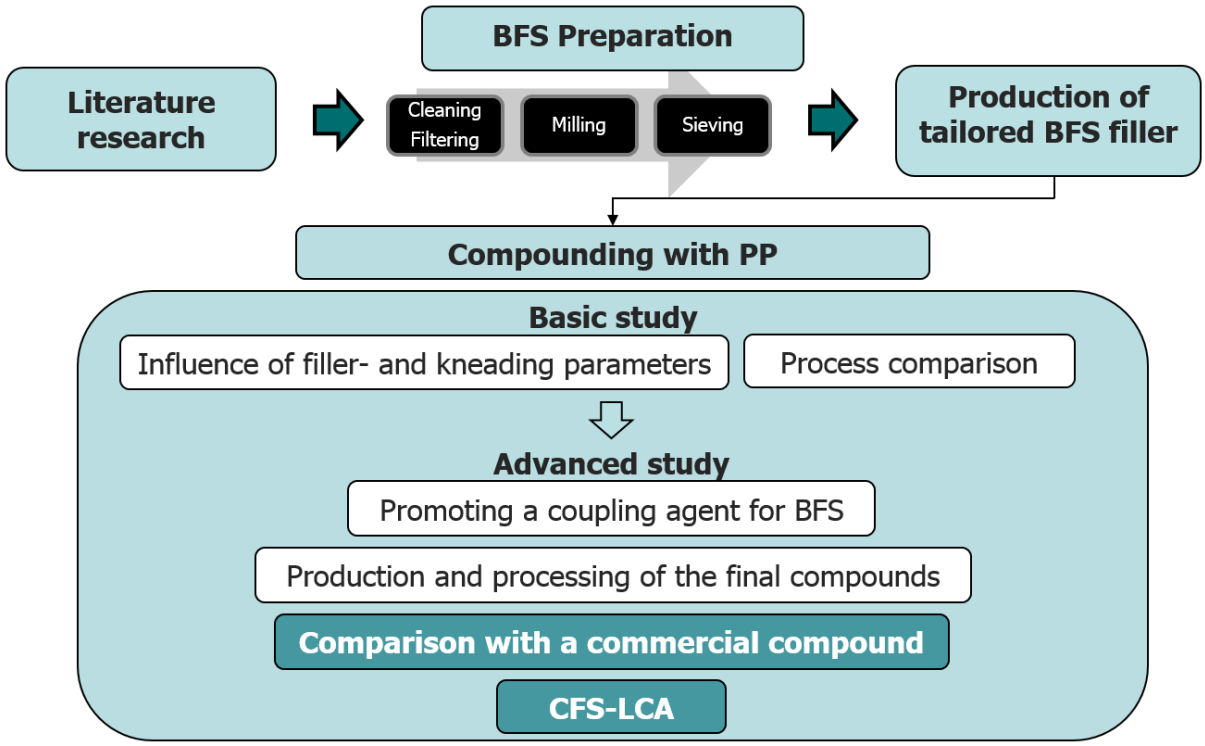

Figure 1: Schematic diagram of the research methodology.

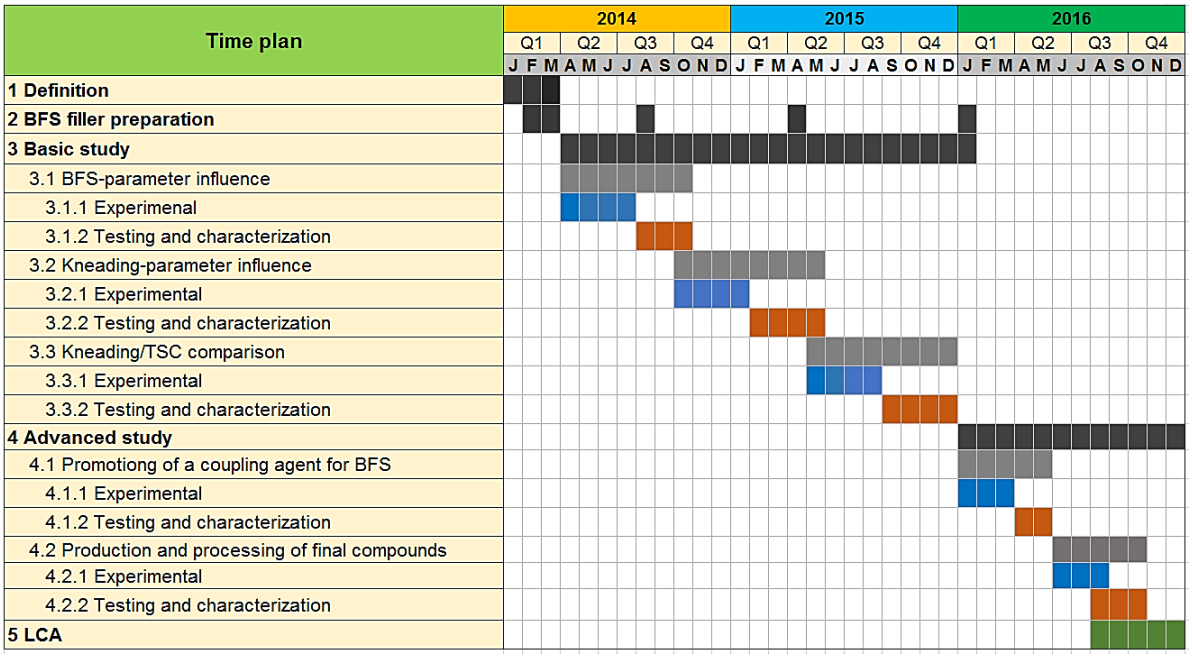

Figure 2: Time plan of the dissertation research.

2 Theoretical Background

2.1 Polypropylene

PP is a thermoplastic polymer produced via polymerization of propylene monomer molecules to produce the polymer's long molecular chains. Among the different ways to link the monomers together, the commercial PP is made with catalysts to form crystallizable polymer chains. There are typically two types of PP. The widely-applied type is usually termed 'crystallizable isotactic', or shortly i-PP. It is a semi-crystalline solid having good physical, thermal and mechanical properties. It has a wide variety of applications, especially in consumer-, automotive- and aero-space industries. The second types are referred to as 'non-crystallizable atactic', or shortly a-PP. These types are rather soft, tacky and mostly used in adhesives and sealants [39]; [96]

Types

Homopolymer: PP homopolymer is a widely applied material, where propylene monomers are linked together in a stereoscopic manner via catalysts. The resulting polymer chains are crystallizable, where the crystallization degree is a function of the conditions under which the entangled chains are transferred from the molten state into the solid one, or upon the straining conditions of a heat-softened solid PP during further processing methods like fiber drawing. PP homopolymer is a two-phase system as it consists of both crystalline and non-crystalline regions. The non-crystalline, or amorphous, regions contain both i-PP and a-PP [39]; [96].

Copolymer: A copolymer is produced via 'copolymerization', a process where two or more monomer units are polymerized together. PP copolymers are applied in more industrial applications compared to the homopolymer. That is because the homopolymer has poor toughness at low temperatures and can easily crack under typical application conditions. The copolymerization of PP usually sacrifices some of the homopolymer rigidity because the crystallinity is decreased. However, the PP copolymer is much tougher than the homopolymer. As shown in Figure 3, there are two major types of polypropylene copolymers: Random and block PP copolymers.

Random PP copolymers typically constitute of a minor chemical phase ranging from 1.5 – 6 wt.-% ethylene or higher alkanes such as butane. The ethylene units are

dispersed in a random manner into the polypropylene unites. The presence of dispersed ethylene unites reduces the crystallization tendency and leads to improved impact strength levels.

A block copolymer is defined by the International Union of Pure and Applied Chemistry (IUPAC) as “a portion of a macromolecule, comprising many constitutional units, that has at least one feature which is not present in the adjacent portions” [37]. In other words, block copolymers are made of blocks of two or more monomer units that are linked together by covalent bonds. For the block PP copolymer, the dispersed ethylene content is much higher than that of random type, causing the copolymerized phase to be slightly rubbery. Hence, PP block copolymers show much higher impact toughness at low temperatures compared to the homopolymer and random copolymer types [39]; [96]; [18].

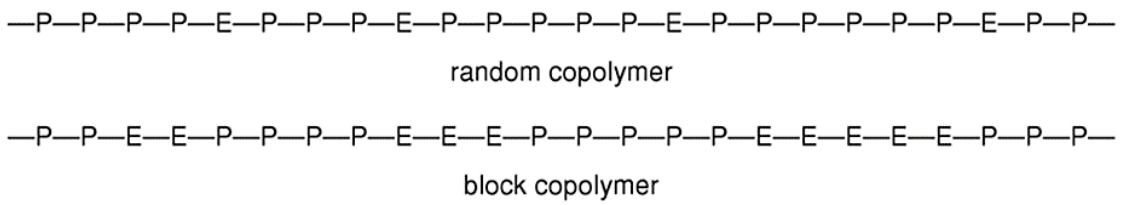

Figure 3: Random- and block PP copolymer structures [96].

Properties of unmodified PP

Table 3 shows dome properties of unmodified PP as compared with competitive thermoplastics. It is demonstrated that PP offers many advantages over other thermoplastics in terms of specific density, heat deflection temperature (HDT), flexural modulus per unit cost and maximum continuous use temperature. Other advantages include low raw material cost, good fatigue- and chemical resistance, easy extrusion- and injection molding processability. Despite these tempting advantages, unmodified PP has some disadvantages such as low impact strength, relatively high mold shrinkage and thermal expansion compared to high-impact polystyrene (HIPS), acrylonitrile butadiene styrene (ABS) and PVC. As a typical semi-crystalline polymer, PP exhibits low UV- and creep resistance compared to amorphous thermoplastics such as ABS or polyvinyl chloride (PVC) [96]; [7].

Table 3: Typical properties of PP as compared with other thermoplastics [96].

Table 1 Comparison of unmodified PP with other materials: Advantages [1]						
Property	**PP**	**LDPE**	**HDPE**	**HIPS**	**PVC**	**ABS**
Flexural modulus (GPa)	1.5	0.3	1.3	2.1	3.0	2.7
Tensile strength (MPa)	33	10	32	42	51	47
Specific density	0.905	0.92	0.96	1.08	1.4	1.05
Specific modulus (GPa)	1.66	0.33	1.35	1.94	2.14	2.57
HDT at 0.45 MPa. (°C)	105	50	75	85	70	98
Maximum continuous use temperature (°C)	100	50	55	50	50	70
Cost (£/tonne)	660	730	660	875	905	1550
Modulus per unit cost (MPa/£)	2.27	0.41	1.97	2.4	3.31	1.74

2.2 Ferrous slags

Ferrous slags, also referred to as iron or steelmaking slags, are co-products of the iron and steel making industries. They are non-metallic materials that form as layers floating above the molten iron or steel. About 87 wt.-% of ferrous slag produced in Europe today are utilized in building roads, bridges and waterways. Ferrous slags can also be used to produce slag wool, a fibrous material used for insulation. They also serve as fertilizers and mixers with Portland cement [95].

2.2.1 History of ferrous slags

The reporting of ferrous slags as an industrial material dates back to 2000 B.C. The earliest reports of utilizing ferrous slags are those of the Greek physician Aristotle, 350 B.C., who stated that slags can be utilized as a medicine for curing wounds. Centuries after, different utilization of slag appeared in Europe like manufacturing of cast cannon balls in Germany (1589) or wharf buildings (1652) and roads (1813) in England. The first discovery of the hydraulic activities and related cementitious properties of slags was recorded by Email Langen in 1862. This discovery started a new era in slag history, which led to a subsequent use of slags in large quantities in different applications of civil and cement industries. Slag utilization has undergone rapid development recently, thanks to the increased environmental awareness and the emergence of the concept of ‘sustainable development’. Many byproducts, including slag, have been hence subject to continuous investigations and modifications to achieve sound environmental and economic standards [93].

2.2.2 Main categories of slags in Europe

Blast furnace slags (BFS)

Due to the relevance of this particular slag type to the current work, a whole chapter later in this context was dedicated to give a detailed overview about BFS. The following two BFS types are relevant in this thesis [94]:

- Air-cooled BFS (ACBS): A crystalline BFS type, resulting upon slow cooling the molten BFS by air and forms into gravel-like particles.
- Granulated BFS (GBS): An amorphous BFS type, resulting upon fast cooling (quenching) of BFS by streams of water and forms into vitrified, sand-like granulates.

Basic oxygen furnace slags (BOS)

BOS are also termed “converter slag” and Linz-Donawitz (LD)-slag. BOS are produced during transformation of liquid iron into steel in the basic oxygen furnace. This type contains oxidized elements such as Fe and Mn [95]; [98]. Based on the European slag association (Euroslag), 21.4 – 24.7 million tons (Mt) of BOS were produced in Europe in 2012 [94].

Electric arc furnace slags (EAF)

EAF slags are formed during melting of either carbon or stainless steel scraps along with other alloys. Cooling of EAF is performed under controlled conditions to form crystalline slag [95]; [98].

Secondary metallurgical slags (SECS)

SECS are produced during refining of crude steel via secondary metallurgical processes. The crude steel from either basic oxygen or electric arc furnaces is treated via different processes to achieve the chemical composition required for casting. Examples of such processes are ladle furnace treatment, vacuum degassing, argon oxygen decarburization and vacuum oxygen decarburization. Different types of slags are produced according to the process used. [95]; [98].

Other Slags

Due to the increasing demand for high quality steel, additional secondary metallurgy systems have emerged, leading to other types of slags such as de-sulfurization slags, resulting from de-sulfurization of hot metals. [95]; [98].

2.2.3 Status of Ferrous slag: Byproduct versus waste

According to The World Steel Association, more than 400 Mt are produced worldwide on daily basis, but the produced slags are not fully utilized in industrial applications [30]. As the slag benefits got wide attention, controversies started to appear regarding the categorization of slag, whether to remain considered as waste, or be promoted into a product or, at least, a byproduct. Communications between the environmental agencies and the EU Commission reached a conclusion that ferrous slag as a material can be regarded as a byproduct rather than waste, as long as it is treated in a way that allows positive involvement in industrial applications. It was stated in the conclusion of the 'Position Paper on the Status of Ferrous Slags' [92], issued in 2012, that "In cases where a slag is initially generated as waste and is then processed in such a way that it can be used for specific purposes, it shall cease to be regarded as waste". It was also stated that "the EU commission already agreed that treatments such as granulation, pelletization, foaming, controlled solidification, separation, crushing, sieving and milling are appropriate industrial processing steps which allow such processed slag to lose the waste status".

Table 4 shows the first time the ferrous slag was declared as a non-waste or a product in different countries in Europe as well as the status declaration year. As previously discussed, the 'modified' ferrous slags have been declared as byproducts. Only the desulfurization slag was excluded from the above description and accepted by the European Steel Industry to be classified as a waste. Meanwhile, some steel companies stopped disposing desulfurization slag and started to process it in a way that it can be utilized as a fertilizer [92].

Table 4: Record for the declaration of BFS as product or non-waste in Europe [92].

Country/year	Slag Type	Classification as
Austria 1991	GBS	non waste
Austria 1999	GBS	product
Germany 1997	EAF-slag produced by BSW	non waste
Germany 1999 North-Rhine-Westphalia	processed BOS	Product
Germany 2006/2007 North Rhine-Westphalia	ABS/GBS/BOS	non waste
Belgium 2007	GBS	by-product (as basic component for cement production)
EU 2007	ABS/GBS	by-product
UK 2007	ABS/GBS	by-product
Finland 2002	ferrous slag	waste
Finland 2008	ABS/GBS and steel slag fertiliser	product

2.3 Blast furnace slag (BFS)

2.3.1 Blast furnace operations

BFS are formed by means of a thermo-chemical reduction in the blast furnace and extracted from the furnace as a byproduct. As shown in Figure 4, Iron pellets as well as fluxes (lime and/or dolomite) are heated under reducing conditions in the presence of injected hot air. Meanwhile, coke and reducing agents are combusted and carbon dioxide is produced, which reduces the iron to a liquid hot metal. Fluxes as well as carbon residues and non-metallic components are chemically combined to produce a non-metallic liquid BFS. The main reactions for each zone are as follows:

- Zone 1: $Fe_2O_3(s) + CO(g) \rightarrow Fe(s) + CO_2(g)$
- Zone 2: $CO_2(g) + C(s) \rightarrow 2CO(g)$
- Zone 3: $C(s) + O_2(g) \rightarrow CO_2(g)$

The molten iron and the liquid slag layer accumulate at the bottom of the furnace. The temperature of liquid BFS reaches 1500 °C when separated from the molten iron. After separation, liquid slag is treated in various ways to yield the different slag variations, discussed in detail at the coming section, where the type of BFS is much dependent upon the raw material and the processing routes [6]; [94].

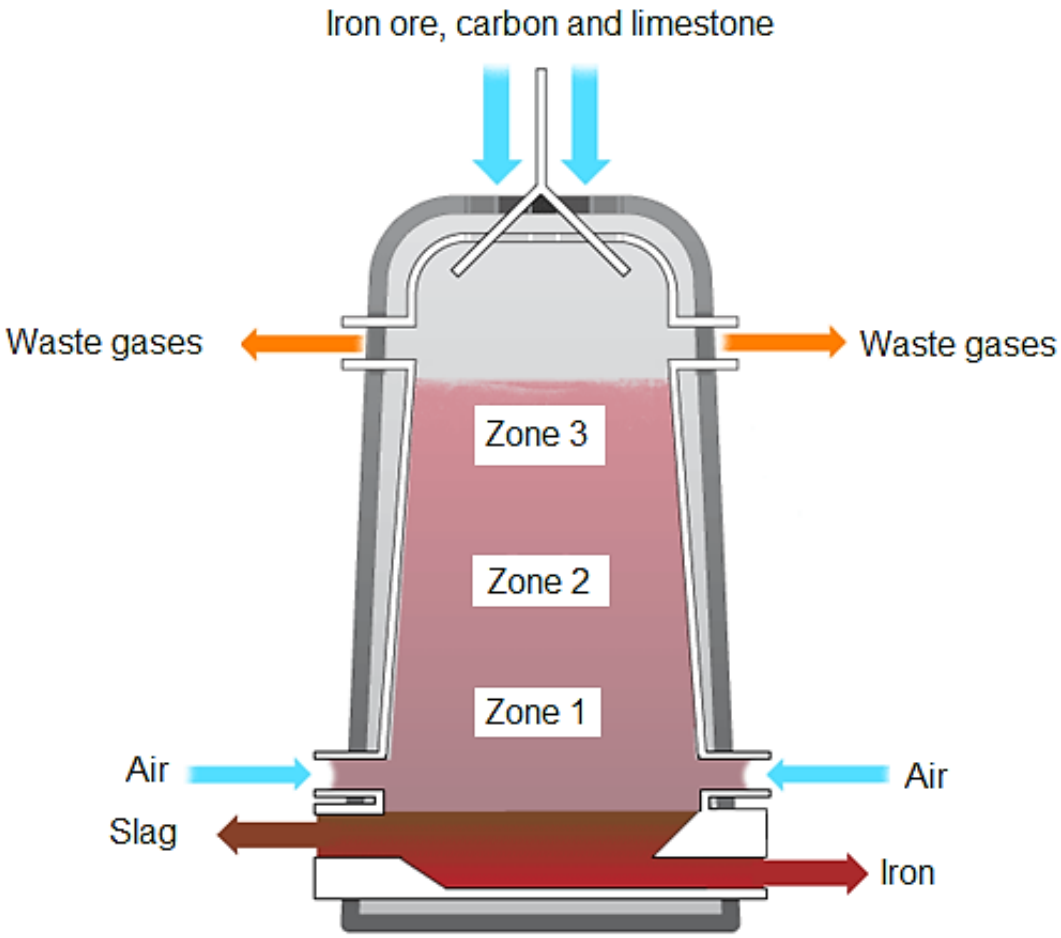

Figure 4: Schematic representation of the blast furnace [6].

2.3.2 BFS types

Upon extraction from the blast furnace, different BFS types are produced depending upon the cooling rate of BFS. Figure 5 categorizes the post-treatment of the liquid blast furnace slag into: Granulation, air-cooling and pelletizing. Table 5 shows how the processing stages of BFS can influence its composition, structure, morphology and properties. A detailed description of each of the three BFS types is as follows:

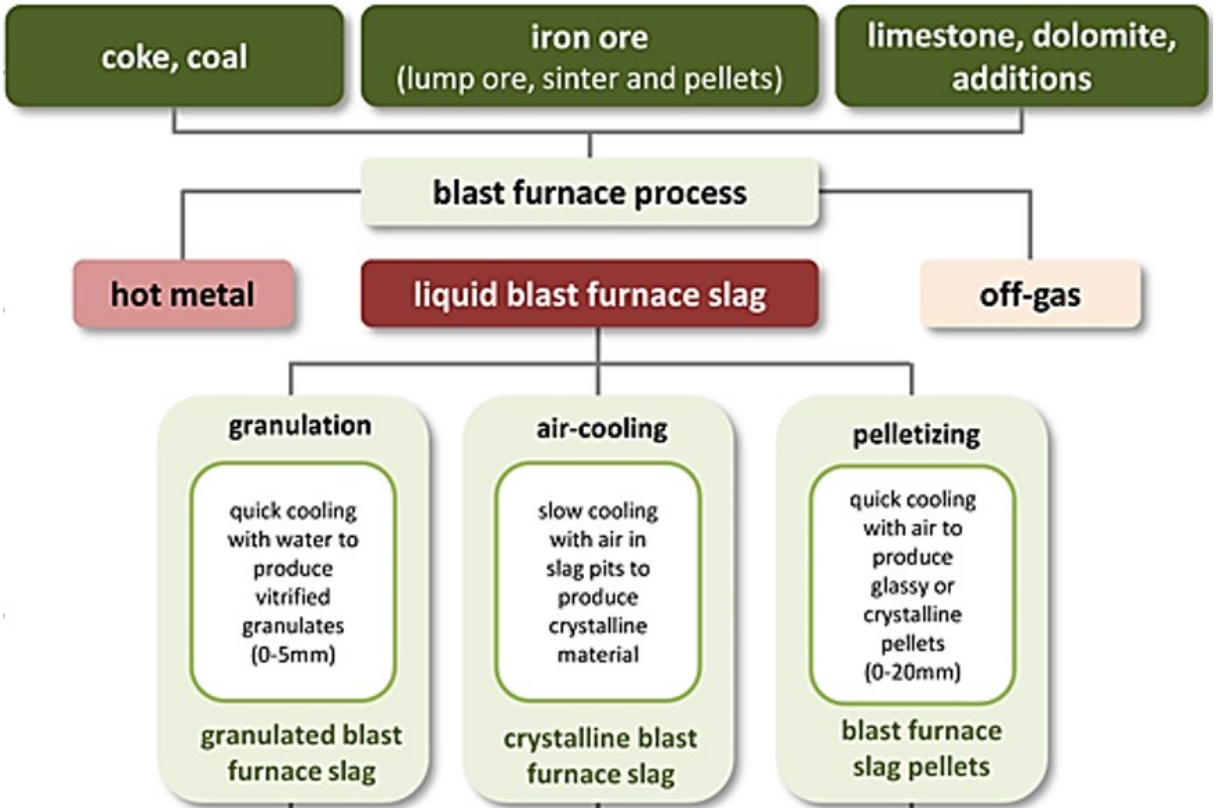

Figure 5: Categorization of blast furnace slags [95].

Granulation

In this process, the molten BFS is rapidly-cooled and chilled with jet streams of water or air below 800 °C to prevent the crystallization and produce a reactive GBS type. [93]; [25]. Ground GBS are also referred to as GGBFS.

Air-cooling

In this process, the molten BFS is subjected to slow cooling rate in air, where BFS is directed into pits or ground bays. When the molten slag flows from the blast furnace, it is a homogeneous liquid. As the slag cools slowly, crystallization starts to take place and crystals of each mineral form as the melt temperature decreased to the crystal's respective formation temperature [93]; [8].

Pelletizing

In this process, the molten BFS is subjected into intermediate cooling rates. The resulting BFS could either be glassy or crystalline [95].

Table 5: Measures to influence the quality of slag [94]

Process stage [1)]	Measures to influence the quality	Influenced properties
Raw material preparation	selection, arrangement and pre-treatment of raw materials related to the chemical comp. of the blast furnace slag	chemical composition e.g. CaO, SiO_2, Al_2O_3, MgO, alkalis
Melting process	selection of suitable process conditions (blast furnace temp., minimization of carbon rate, gas flow, etc ...)	temperature, composition of the products
Heat treatment	different cooling rates a) quick: - blowing - granulation - pelletizing	glass content, structure, porosity
	b) moderate - foaming	bulk density, strength, porosity
	c) slow - air-cooling	strength, porosity, resistance to polishing, grain size
Processing	crushing sieving grading milling	grain size, shape, grain size distribution

[1)] All process stages are subjected to a continous production control

2.3.3 Chemical and mineralogical composition of BFS

Nearly 20 % of total mass produced in the blast furnace is formed into slags. As the chemical properties of BFS principally depend on the specific production processes followed, the final BFS may show a wide variation of properties. It could be “as crystalline as granite or as amorphous as glass; it may have hydraulic properties approaching those of Portland cement or be as inert as basalt” [8]. What is considered common for BFS is that they result from lime and silica based melts. Therefore, BFS is primarily composed of four major oxides constituting more than 90 % of the total

composition: Lime or calcium oxide (CaO), silica or silicon oxide (SiO_2), alumina or aluminum oxide (Al_2O_3) and magnesia or magnesium oxide (MgO). BFS contains other minor oxides such as iron oxide (FeO) and manganese oxide (MnO) as well as minor elements such as sulfur (S) [8]. The composition of BFS varies from one furnace to another according to differences in the "proportions and constituents of the ores, fluxes, coke, scrap and other raw materials; the grade of metal being made; and differences in operating practice" [8]. Table 6 shows the typical composition of blast furnace slag produced at the company voestalpine Stahl GmbH, Austria [103].

Table 6: Composition of BFS in voestalpine Stahl GmbH, Austria [103].

Component	CaO	SiO_2	Al_2O_3	MgO	FeO	K_2O	Na_2O	S	MnO
Amount (%)	37-38	38-39	10-13	8-10	≤ 0.5	1-1.3	0.3	0.7-1.1	0.8-1.5

In general, the ratio of silica to alumina is approximately 3:1 by weight and the ratio of acids (SiO_2 and Al_2O_3) to the bases (CaO and MgO) is roughly 1:1. Air-cooled BFS types are normally gray in color but their shades can vary, i.e. to brown, depending on the colors of the minor constituents and colloidal solutions. Granulated types, on the other hand, are usually lighter in color compared to air-cooled ones and are often distinguished by a yellow-to-brown shades [8]; [103].

BFS is a material characterized with a complex structure, which is a solid solution of combined oxides that constitute one or more phases. Depending on the ratios and types of oxides, different solid solution can emerge. The most notable solid solutions present within BFS are shown in Table 7. The most common mineral in BFS is termed 'melilite', which refers to "a series of solid solutions extending from akermanite to gehlenite" [8]; [49].

Table 7: Notable phases or solid-solutions constituting BFS [49].

Mineral	Formula
Akermanite	$2CaO\text{-}MgO\text{-}2SiO_2$
Gehlenite	$2CaO\text{-}Al_20_3\text{-}SiO_2$
Wollastonite	$CaO\text{-}SiO_2$
Dicalcium silicate	$2CaO\text{-}SiO_2$
Merwinite	$3CaO\text{-}Mgo\text{-}2SiO_2$
Anorthite	$CaO\text{-}Al_2O_3\text{-}2SiO_2$
Monticellite	$CaO\text{-}MgO\text{-}SiO_2$

The whole melilite series show the same form of crystallization, where the crystals are tabular in form and appear in the form of dendrites, laths, octagonal and rectangular plates. Figure 6 shows the development of the dendritic melilite crystals, denoted by a light-gray color, upon crystallization of BFS. This is followed by the development of the anorthite ($CaAl_2Si_2O_8$) mineral phase at the background, denoted by a dark-gray color. The white regions correspond to the sulfide phase [59]. Slags have been studied in the frame of different phase diagrams and systems such as lime-alumina-silica, lime-alumina-magnesia, magnesia-alumina-silica systems as well as akermanite-gehlenite system. Figure 7 shows BFS zone within the lime-alumina-silica ternary system [103]; [8].

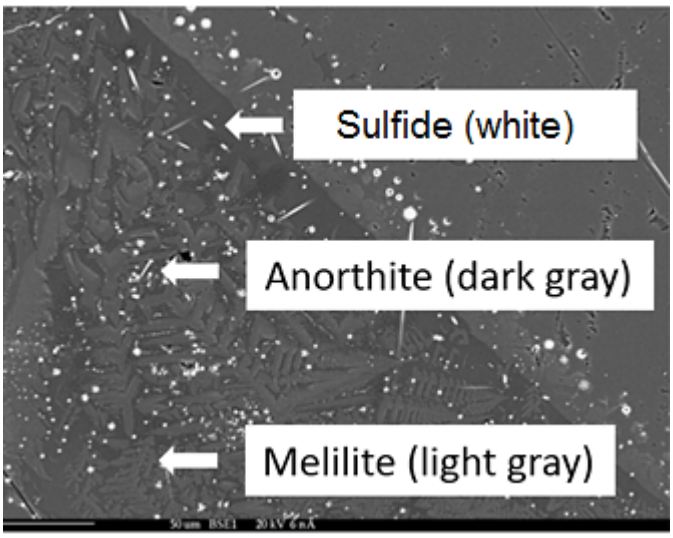

Figure 6: SEM micrograph of blast furnace slag from voestalpine Stahl GmbH showing the dendritic melilite, anorthite and sulfide phases [59].

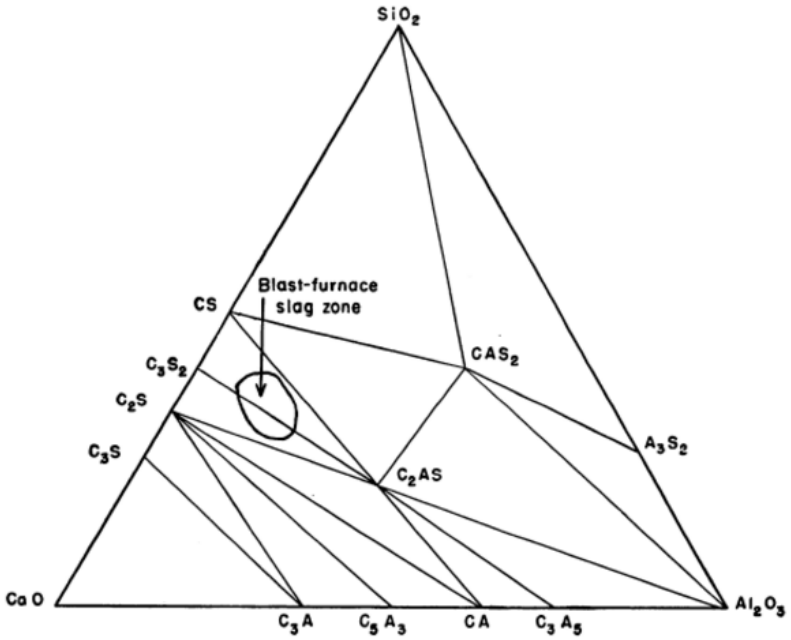

Figure 7: BFS-Zone within the lime-alumina-silica ternary system [8].

2.3.4 Properties of BFS

Table 8 shows the properties of BFS compared with steel slag, basalt and greywacke. The chemical, mineralogical and physical properties of BFS and steel slags are similar to those of natural rocks. The high compressive strength and good polishing and freeze resistance make BFS and steel slags ideal candidates for road construction applications [94].

Table 8: Some properties of iron and steel slags compared to natural rocks [94].

Property	Blast furnace slag	Steel slag	Basalt	Greywacke
particle density (g/cm3)	2,4	3,6	3,0	2,7
compressive strength (N/mm2)	100	200	300	200
impact value (%)	27	17	17	20
resistance to polishing (PSV)	50	57	50	56
water absorption (%)	2	1	<0.5	<0.5
resistance to freeze/thaw (%)	<0.5	<0.5	<0.5	<0.5

BFS properties were collected and tabulated in comparison to the respective properties of common mineral fillers, as illustrated in Table 9. It is observed that the water absorption of BFS is comparable to that of calcium carbonate, but lower than that of mica and talc. The specific gravity of BFS is also comparable to that of calcium carbonate, talc and silica, while less than that of mica. In addition, the hardness of BFS has an intermediate value between calcium carbonate and silica [62]; [94].

2.3.5 Global production and applications of BFS in 2010

BFS production reached 23.5 Mt in 2010. About 82 % of this amount was granulated and 18 % air-cooled, as shown in Figure 8. The use of blast furnace slags exceeded the manufactured amount because the slag from deposits was also utilized. The largest area of applications for slag in 2010 is cement production/concrete addition, where 66 % of slag is employed, followed by applications road construction with 23 %. [92].

Table 10 and Figure 9 show the typical application of BFS in Europe, where the European Slag Association (Euroslag) reported that “the use of blast furnace and steel slag – crystalline or vitrified – is as environmentally sound as that of similar natural primary products and does not present any increased risk to human health or the environment” [92].

Table 9: Properties of BFS as compared to common mineral fillers [94]; [62]

Filler	Mica	Calcium carbonate	Wollast-onite	Glass Beads	Alumina Hydrate	Talc	Silica	Franklin Fiber	Clay	BFS
Water content (%)	<5	<2	0.5	<0.1	34.6	4.8	<0.1	<1	<0.5	2
Specific gravity	2.74 – 2.95	2.6 – 2.75	2.9	2.48	2.42	2.7 – 2.8	2.65	3	2.5	2.4-2.8
Hardness (Mohs)	2.4 – 3	3	4.5	5.5	2.3 - 3.5	1	7	2	4 - 6	4 - 5
Melting point (°C)	1300	900	1540	1200	200 – 600	Stable to 380	Stable to 573	-	1810	1150 - 1430
Color	Gold-brown	White	White	Clear	White	Gray-White	White	White	White	Gray/ brown
Resistance to Acids/ Alkalis	Good/ Good	Poor/Fair	Good/ Poor	Good/ Poor	Good/ Good	Good/ Good	Excellent/ Good	Good/ Good	Good/ Good	Good/ Good

Figure 8: GBS and ACBS production in Europe-2010 [92]

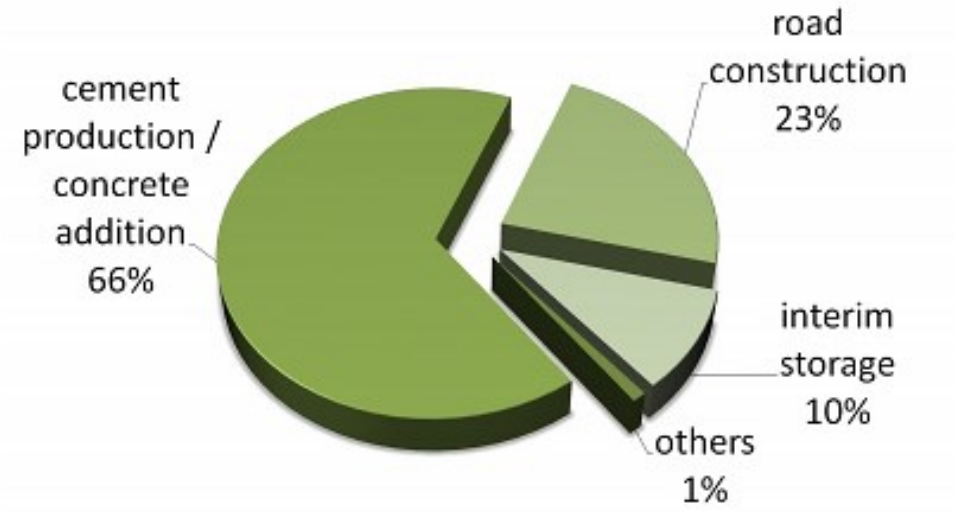

Figure 9: Different applications of BFS in Europe-2010 [92].

Table 10: Applications of ACBS and GBS [92].

Slag	Nomenclature	Manufacturing Process	Applications (examples)
Blast Furnace Slag, air – cooled - ABS	Slag, ferrous metal, blast furnace (air-cooled)	Crushing and screening of the air cooled slag. Also available as uncrushed slag.	**As aggregate for:** - bituminous and hydraulically bound mixtures (asphalt, concrete, road binder etc.) - unbound mixtures (unbound surface layers and wearing courses etc.) - waste water treatment - embankments and fill - railway ballast - roofing - ground stabilisation **For the manufacture of:** - stone wool - glass (blended with other components) - fertilizer
Blast furnace slag, granulated – GBS or GGBS	Slag, ferrous metal, blast furnace (granulated or ground granulated)	Rapid quenching of the molten slag with high pressure, high volume water sprays, grinding of the granulated slag to cement fineness	**As aggregate for:** - bituminous and hydraulically bound mixtures (asphalt, concrete, road binder etc.) - unbound mixtures (unbound surface layers and wearing courses etc.) - embankments and fill - sand blasting - ground stabilisation **For the manufacture of:** - cement and other hydraulically binders - concrete (as GGBS) - fertilizer (ground) - stone wool - glass (blended with other components)

2.3.6 Environmental aspects of BFS

Numerous tests and investigations were conducted to assess the impact of slags on ecology and human health. That is, toxicity tests (e.g. skin and eye irritation, skin sensitization, gene mutation in bacteria, cytogenicity in mammalian cells) as well as eco-toxicity tests (e.g. short- and long-term toxicity on invertebrates, effects on soil micro-organisms, toxicity to terrestrial plants, growth inhibition of algae) were performed. It was proved that ferrous slags did not release any dangerous substances and that all emissions released are still within allowable limits. It is also interesting to mention that no negative environmental impact has been reported for ferrous slags. On the contrary, slags are reported to contribute positively to environmental sustainability and against climate change. That is because using of slags promotes [20]; [4]:

- avoidance of landscape disruption as a result of mining activities
- saving of energy costs associated with mining and processing of natural fillers, such as talc and chalk
- reduction of CO_2 emissions associated with fuel savings (for instance, sintering of limestone)

2.4 Minerals filled PP systems

Examples of common industrial mineral, inorganic fillers reported within PP systems include calcium carbonate, mica, silica, kaolin, titanium oxide, zeolite and fly ash. It was reported that such fillers could combine cost reduction with improvement of functional performance of the polymer, hence they are referred to as ‘functional mineral fillers’ in this context. The following sections provide a review of reported endeavors to enhance PP performance using BFS and the aforementioned functional mineral fillers. To match the scope of this work, only PP systems with micron-sized fillers are reviewed.

2.4.1 BFS or flyash filled PP

Almost no systematic research studies for preparing a tailored BFS-filled PP composite have been proposed so far. Utilization of BFS was found to be surprisingly limited in

polymer industry, while the modest number of the reported BFS-filled thermoplastic studies lacks the systematic research methodology the current study aims to provide. Nearly all reported patents discussed the utilization of BFS for cement production-related applications [27]; [28]; [65]. Studies or patents in which blast furnace slag is used as a filler for thermoplastics are very limited. One example is the study reported by Padhi et al. [73], where the team prepared a hybrid short glass fiber/BFS reinforced PP composite by means of injection molding route. It was reported that the combination of glass fiber and BFS was effective for enhancing the wear resistance of the composite. Another example is a patent invented by Kamigaito et al. [38] with the aim of producing a thermoplastic polymer composite material filled with an industrial mineral waste fillers such as oil shale fly ash, clinker dust of cement industry or limestone mud or a mixture of them. The composite was produced via extrusion or injection molding techniques and was shown effective in applications involving films and pipes. In fact, the team did not mention whether similar findings could be attained if BFS is used instead of one of the aforementioned fillers, or even in combination with them.

Fly ash is an industrial waste mineral with complex oxide constituents that are quite similar to those of BFS in terms of type and composition [64]. Some patents and published studies were reported regarding the utilization of fly ash as a promising filler for PP and other thermoplastics such as low- and high density polyethylene (LDPE, HDPE) [77]; [35]; [33]; [31]; [3]; [29]. Compounding fly ash with both virgin and waste/recycled PP was reported by Huang et al. [32], Gummadi et al. [26], Yildirim et al. [89] and Das et al. [19]. Huang team reported that the vinyl silane-coated spherical fly ash particles were capable of bonding well with the PP matrix, improving the strength and flexural modulus of the composite. They also emphasized that composites filled with fly ash could be utilized for producing commercial automotive parts like trim clips by means of injection molding, where similar performance to composites with conventional fillers, such as calcium carbonate, could be achieved. That is, fly ash filled PP composites can offer comparable dimensional accuracies, injection moldability and surface quality to that of PP composites filled with conventional mineral fillers. The research teams of Yildirim and Das effectively utilized both PP and fly ash waste to build construction composites that are ecologically attractive and remarked by good flexural and insulation properties and less absorption

behavior. Silane was emphasized to be an attractive coupling agent choice for PP-fly ash systems. In another study, Chow et al. [15] utilized fly ash from municipal solid waste incineration (MSWI) as a filler in PP. The obtained composites were subjected to outdoor weathering, where the tensile fracture strength were decreased upon addition of 0 – 20 wt.-% fly ash. The tensile fracture strength improved, however, after subjecting the composite samples to high temperature, humidity and UV weatherability conditions. The authors reported that the annealing effect associated with such weatherability conditions was likely to complete the structure of PP and improve its tensile properties.

2.4.2 Other mineral-filled PP systems

Wang et al. [100] reported that a modified micro-sized calcium carbonate functional filler improved the impact strength of i-PP homopolymer up to a critical filler loading, where high loadings of rigid filler resulted in a significant decrease in impact strength. Wang et al. [101] reported that in the highly filled compound and the treatment of calcium carbonate filler had a noticeable impact on the compound behavior. That is, the treatment of the filler reduced the complex shear viscosity, which are typically high for non-treated fillers at high loadings. Meng et al. [60] used of a novel 2.5-µm calcium carbonate filler modified with pimelic acid in i-PP. The research team observed that the compounds filled with modified calcium carbonate showed better filler-matrix compatibility and improved dispersion uniformity compared to those with unmodified filler. The authors suggested that the filler modification slightly decreased the ultimate tensile strength but notably increased both the tensile- and flexural moduli. Another study was reported by Gendron et al. [22], where TSC parameters such as feed rate, filler treatment, screw speed and barrel temperature profile were investigated for PP compounds filled with a micron-sized calcium carbonate filler. The authors showed that the processing feed rate, filler type and screw speed parameters recorded the most significant impact upon the degree of dispersion. The authors also implied that the optimal conditions for filler dispersion might not necessarily be optimal for the matrix structure. To evaluate the influence of aspect ratio and filler-matrix compatibility on the mechanical properties, Nurdina et al. [69] melt-compounded i-PP with micro-sized calcium carbonate, silica and mica fillers to produce mono- and hybrid PP composites. The research team reported that mica-filled PP composites recorded better ultimate

tensile strength and stiffness due to the filler's high aspect ratio and good compatibility with the PP matrix. A system of ultrafine kaolin-PP was studied by Mareri et al. [55], where the team studied two types of surface treatments, stearic acid and a quaternary ammonium scattering agent, on the stiffness and the impact strength of the composite. The authors showed that the stearic acid treatment successfully increased the impact strength but reduced the stiffness of the composites. The other treatment, however, lead to a general improvement in the mechanical properties, including the compound stiffness.

2.4.3 Silane-modification of mineral fillers

Mineral fillers are usually incorporated into PP composites after being surface treated with a proper coupling agent. A coupling agent may be defined as "a substance that couples or bonds the filler to the polymer matrix" [39]. To be able to perform its bonding function, the coupling agent must be capable of interacting with the polar mineral filler and the non-polar polymer molecular chains.

A successful filler-matrix coupling is usually reflected by an improved yield or fracture strength, as the load can be easily transferred from the matrix to the filler, thanks to the coupling mechanism. The effect of the coupling agent on modulus is rather unclear [39]. Organofunctional silanes have been commonly reported to be effective coupling agents for mineral-filled PP systems. Silane molecules have a unique structure, where on one end exists a hydrolyzable group which is considered an intermediate in the formation of silanol groups. The silanol groups can chemically attach to the mineral filler's polar surface. On the other end, silanes have organofunctional groups that can physically entangle with the polymer chains. The silane product is defined according to its organofunctional group, which can be epoxy, methacrylate, vinyl, amine, etc. In fact, the functional group on the backbone of the polymer usually determines the type of the silane organofunctional group to react with; hence, the appropriate silane product for the polymer can be chosen. For instance, silanes that have amino groups are commonly used with polyolefins and polyamides, where reaction sites for the silane amine groups are provided via the abundant carboxylic acid end groups existing along the molecular chain [85].

Silane modification mechanisms

There are two widely-accepted theories describing the mechanisms behind the functionality of silane as a coupling agent: The 'chemical reaction' and the 'diffusion' theories. 'Chemical reaction' theory suggests that the covalent bond forming between the filler and the polymer is the main drive for the interfacial adhesion. As shown in Figure 10, the hydrolysis reaction of the silane results in intermediate silanol groups (Si-OH). These groups react with each other to form more stable, cross-linked siloxane bonds (-Si-O-Si-) which further react with silanol to form covalent –Si-O-M- bonds. These bonds, in addition to other H-bonds, are believed to trigger a strong interfacial adhesion between the silane and the filler particle [111]. On the other end, the organofunctional group reacts with the polymer and adheres to it, as shown in Figure 11. The 'diffusion' theory states that the silane molecules defuse into the polymer matrix, resulting into a formation of an interpenetrating network of the polymer and the silane [39]; [85].

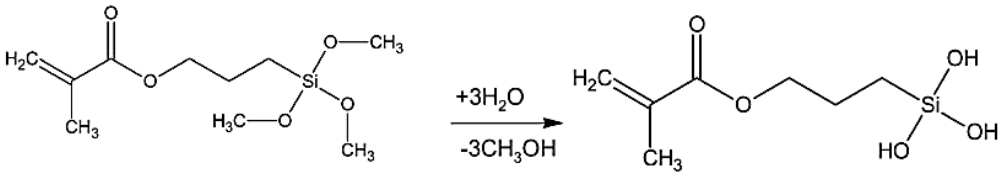

Figure 10: Silane hydrolysis, where hydrophobic 3-methacryloxypropyltrimethoxy silane reacts with water to form hydrophilic silanol [63].

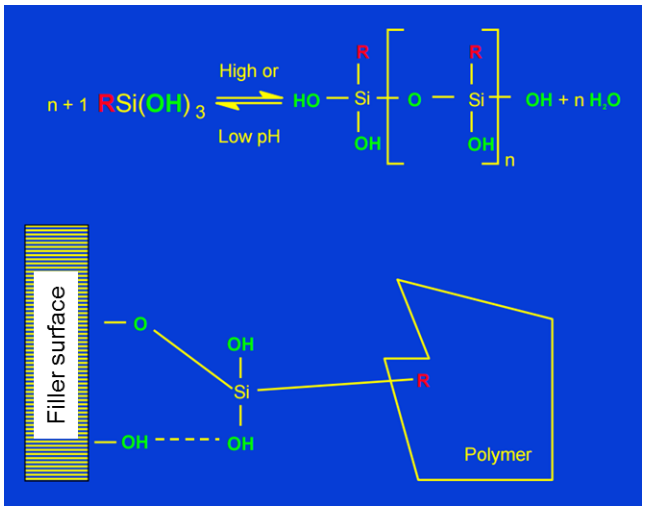

Figure 11: Interaction of the silane with the polymer matrix [53].

Unfortunately, no reporting of possible interaction mechanisms between modified-BFS and PP was found in literature so far. Interaction mechanisms with PP were reported, however, for other minerals such as fly ash and silica. Those reported mechanisms might explain the possible interaction mechanism(s) of modified-BFS with PP. Sengupta et al. [87] modified fly ash with furfuryl palmitate coupling agent, a renewable chemical with flame retardant properties.

As illustrated in Figure 12, the hydroxyl group (OH) on the surface of the fly ash particle was covalently bonded to the coupling agent, while the organofunctional groups reacted with PP. Zheng et al. [109] reported that nano-silica was modified by 3-methacryloxypropyltrimethoxysilane (MPS) and grafted with polymethyl methacrylate. The authors reported that the inorganic mineral silica particle was covalently bonded to the silane coupling agent by means of hydroxyl functional groups, as illustrated in Figure 13. The research team suggested that the hydroxyl groups on the surface of the nano-silica particle reacted with the silanol groups. These groups were formed by the hydrolysis of alkyloxyl group of MPS through condensation and dehydration. Si-O-Si- bonds were hence formed, where the vinyl groups attached to the silica surface by means of covalent bonds. Such interactions enhanced the interfacial bonding to a large extent. It is hence concluded that coating BFS with MPS could have triggered similar mechanism, where the interaction between the silane and BFS is caused by the covalent-bond interaction between the hydroxyl groups on BFS surface and the silane.

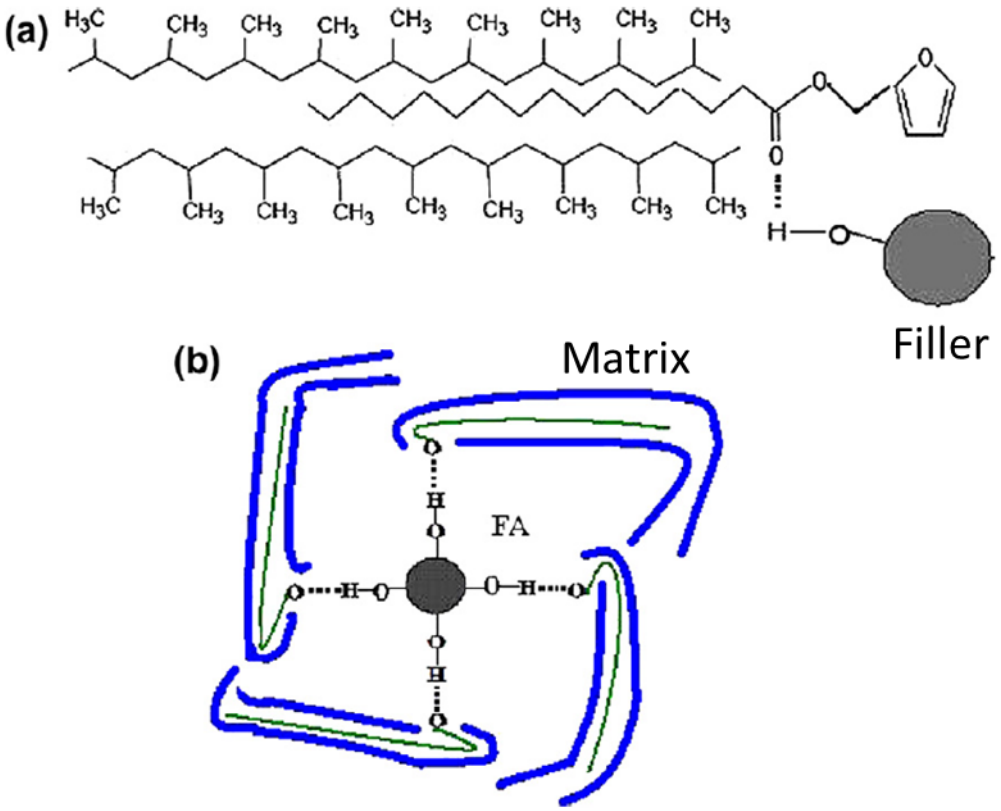

Figure 12: (a) A possible chemical interaction between furfuryl palmitate coated FA and recycled PP, and (b) a schematic representation of filler-matrix interactions [87].

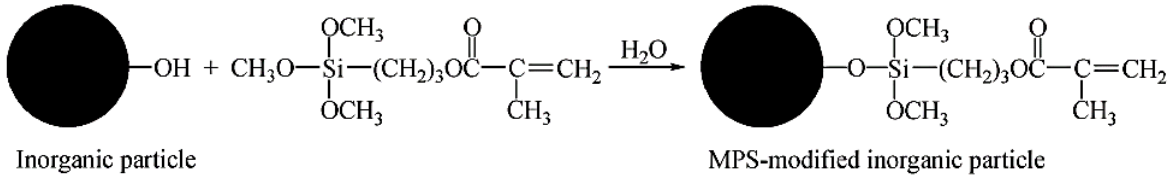

Figure 13: The coupling mechanism between PP and fly ash particles via MPS silane [109].

2.5 Compounding

2.5.1 Definition and tasks

Compounding may be defined as the process by which fillers and additives are added to the polymer. In principle, bio- and synthetic polymers are rarely used in their neat forms. That is, different additives are added to the virgin polymer in the form of plasticizers, fillers, stabilizers, colorants, etc. [61]. The compounding process may also be defined as a melt mixing process where different components are mixed together in a single screw extruder (SSE) or twin screw extruder (TSE) to form a new material with different properties. The compounding process is defined by Giles et al. [23] to be "as simple as mixing a colorant in the form of a liquid, powder, or concentrate into the polymer melt to change the resin color, or as complicated as blending or alloying two or more different resin systems while adding a filler, reinforcement, colorant, flame retardant and/or stabilizers to produce a radically different formulation with its own unique properties and end-use performance".

As discussed later in this context, compounding is predominantly achieved via co-rotating compounding TSEs, denoted in this work as TSCs, with continuous endeavors to increase drive powers, torques and screw speeds. Increasing screw speeds directly increases extruder throughput, resulting in higher thermal and mechanical stresses upon the compound as well but lower processing (residence) times. Such increase usually comes with the risk of decreasing the product quality due to the reduction of molar mass and existence of thermal inhomogeneities and melting inconveniences. Therefore, the design of both the extruder and the screw needs to be constantly optimized to avoid these problems. Compounding applications include [45]:

- Polymer reinforcement (i.e. incorporation of fiber or particles)
- Modification of thermoplastics for improved impact resistance (i.e. blending with rubber elastic components)
- Enhancement of the dimensional stability, compression strength and flame retardant behavior of polymers
- Production of polymer blends (i.e. mixing in-/compatible polymers)
- Coloring polymers (i.e. incorporation of pigments and masterbatches)

- Enhancement of the chemical/physical stability of polymers (i.e. incorporation of low-viscosity stabilizers and antistatic agents)

2.5.2 Principles of mixing

Mixing of polymers and other materials is considered a widely applied industrial process. Depending on the application, it can be regarded as a process by itself, or part of a more versatile sequence of processes. Mixing in general occurs through a combination of three mechanisms: Convective transport, eddy diffusion and molecular diffusion. 'Convection transport' is a hydrodynamic mechanism that can be found in both laminar and turbulent conditions. 'Eddy diffusion' is also a hydrodynamic mechanism that is produced by local turbulent mixing. Such mechanism prevails in the simple example of stirring cream into a cup of coffee. It is normally found in gases and low-viscosity liquids. The third mechanism, 'molecular diffusion', is a very slow operation but is considered the true mixing that is attained on the molecular-level. Such mechanism is activated by chemical potential difference as a result of concentration variation among gases and miscible liquid systems [61]; [23].

The two basic types of polymer/non-polymer mixing can be identified as: (1) Extensive, also referred to as distributive, convective, repetitive, blending mixing and (2) intensive, also referred to as dispersive and dispersing mixing, as illustrated in Figure 14. Extensive or distributive mixing is a process that functions under low stresses and aims to reduce the uniformity of the distribution of the minor component into the major one. Intensive or dispersive mixing, on the other hand, is a process that involves high stresses and aims at breaking down the minor phase, agglomerates, into finer components and then 'distributing' these finer components into the major component. Dispersive mixing changes the physical characteristics of one or more components. Dispersive mixing process can hence be divided into two stages: Introduction or incorporation of the additive into the polymer matrix; and deagglomeration or breaking down of the additive and dispersing in throughout the matrix [23].

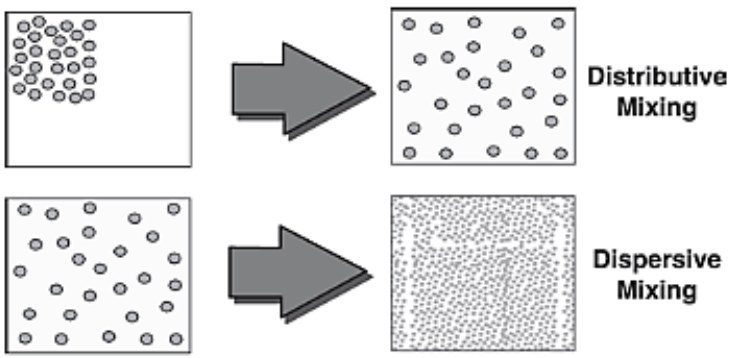

Figure 14: Distributive and dispersive mixing [99].

2.5.3 Extrusion process and extruder types

Extrusion is a process that aims to provide sufficient pressure, homogeneity and temperature to force the material through a die. The amount of pressure needed depends upon factors like the flow rate, geometry of the die and flow characteristics of the extruded material. The process can be applied for nearly all conventional polymers as well as biopolymers. Extrusion itself is a very versatile operation; that is, extruders are not solely used for extrusion purposes, but can integrate with other processing techniques such as injection- and blow molding. There are different types of extruders such as single-, twin screw-, planetary- and pin extruders. In this context, only the first two types are discussed for their relevance [61].

2.5.4 Single screw extruders

As shown by the schematic representation of a typical SSE is illustrated in Figure 15, the SSE zones start with (1) the feed zone, where the aggregate polymer enters the extruder via the hopper and gravity-fed to the feed throat, then it becomes in direct contact with the screw. Along the extruder length, the polymer travels through different zones known as the (2) solid-conveying, where the polymer aggregates are transformed from the solid into a melt- or softened state. Afterwards, the polymer enters the (3) and (4) metering, pumping and mixing zones, where the distributive mixing takes place and the melt is pumped to the die. The barrel is surrounded by a heating band that provides part of the heat necessary for melting the polymer, while most of the heating comes from the friction among the polymer particles. Pellets are

compressed in the channel and are dragged forward by means of friction drag mechanism [23]; [61] .

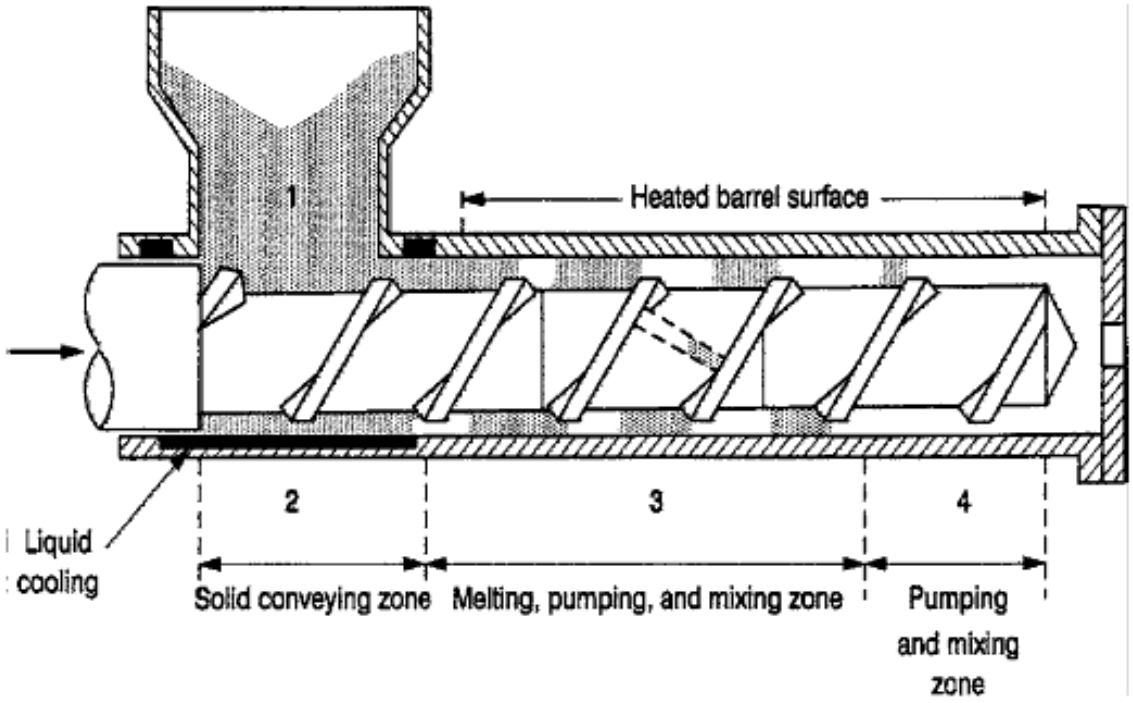

Figure 15: Single Screw extruder showing the four primary zones [61].

2.5.5 Twin-screw extruders

Instead of one rotating screw shaft, twin screw based extruders employ two parallel, or conical, screw shafts rotating together. They execute the same elementary polymer processing steps as in SSEs. What makes TSEs, specifically co-rotating types, superior in dealing with polymer melts is the additional physical mechanisms emerging from the screw-to-screw interactions. These mechanisms have profound influence on both melting and mixing steps, allowing rapid melting of the polymer over a short axial length and hence narrow residence time distribution (RTD). In addition, screw-to-screw interactions generate three-dimensional, time-varying, extensional melt chaotic flows that promote pressure gradients and rapid combination of distributive and dispersive mixing, as illustrated in Figure 16 [91].

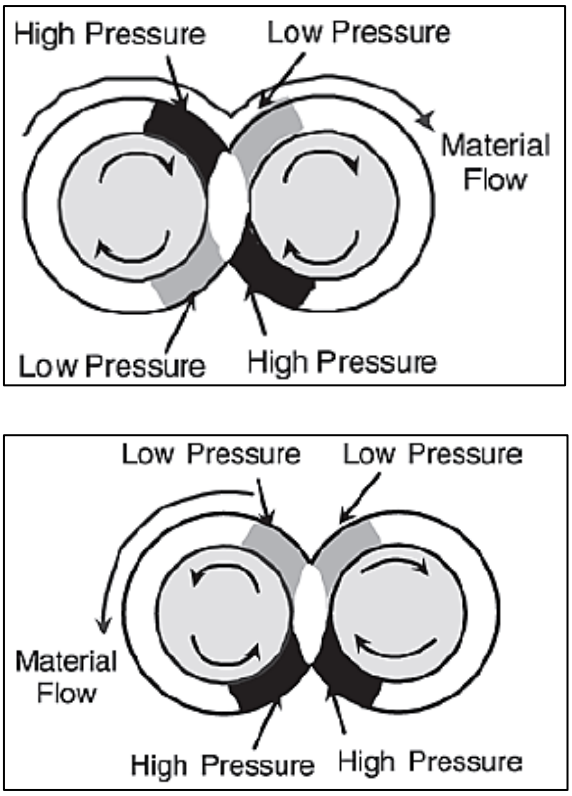

Figure 16: Material flow in co- (above) and counter-rotating screws (bottom) [23].

There is a variety of twin screw equipment models commercially available, where each design is optimized toward its end-use application.

Twin screw extruders can be categorized, Figure 17, into:

- Co-rotating extruders
- Counter-rotating extruders
    - Parallel counter-rotating extruders
    - Conical counter-rotating extruders

As illustrated in Figure 18, based on the rotation direction of each screw, parallel twin screw equipment could be basically classified into ‘co-rotating’ and ‘counter-rotating’ types. In addition, the extruder is referred to as ‘intermeshing’ when the centerline distance between the screw shafts is less than the screw diameter. Alternatively, the extruder is a ‘non-intermeshing’ type when the distance between the screw shafts equals the screw diameter. The applications vary depending on the TSE type, which will be discussed in more detail in the following sections [23]; [99]; [84].

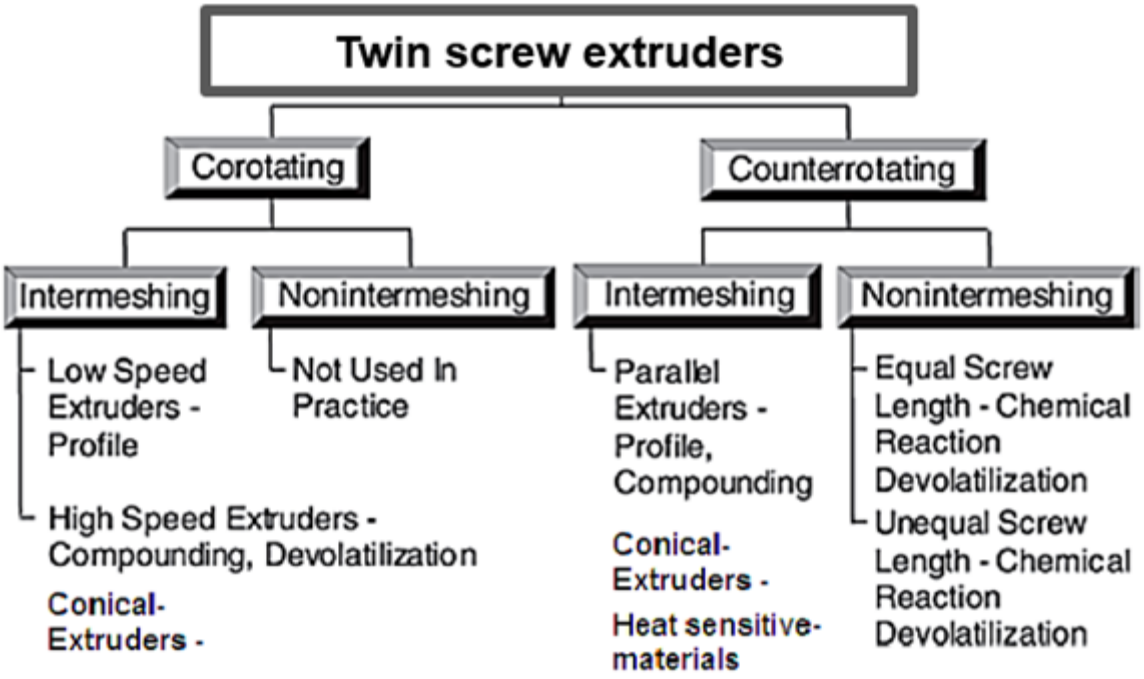

Figure 17: Types and application areas of TSEs (the main heading of the original figure was modified from previously 'parallel twin screw extruders' and the conical extruder section was added to the original figure for consistency) [23].

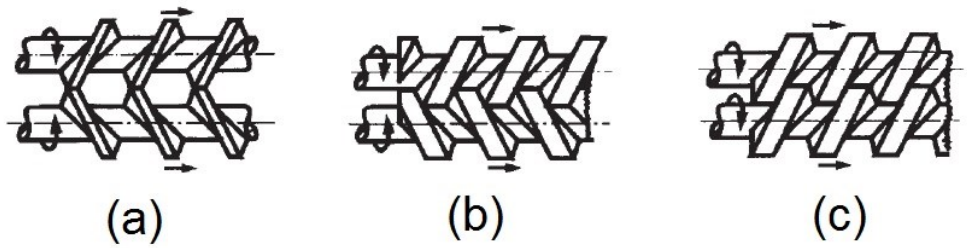

Figure 18: TSE configurations: (a) non-intermeshing, counter-rotating, (b) intermeshing, counter-rotating and (c) intermeshing, co-rotating screws [23].

2.5.5.1 Counter-rotating extruders

Parallel counter-rotating extruders

Parallel counter-rotating extruders are usually utilized in medium to high performance ranges. Typical applications of this type of extruders are devolatilization, chemical reactions like grafting, addition and condensation, functionalization and controlled

cross-linking. In addition, they are suitable for processing heat-sensitive materials like PVC, where pipes, profiles and sheets can be easily produced.

Conical counter-rotating extruders

There is commercially utilized variation of counter-rotating extruders in which the screws are tapered: The conical intermeshing, counter-rotating extruder, Figure 19. Conical extruders exert lower shear rates as compared to parallel ones; therefore, they are usually utilized in applications requiring low to medium performance. As a member of the counter-rotating screw extruder family, they are typically utilized in the processing of heat-sensitive materials such as PVC and food [23].

Figure 19: Conical, intermeshing screws variation [23].

2.5.5.2 Co-rotating extruders

Similar to the counter-rotating TSEs, low-speed, intermeshing co-rotating TSEs are used for producing profiles and pipes. On the other hand, high-speed, intermeshing co-rotating twin screw extruders are typically used for compounding polymers and resins with additives such as colorants, fillers, stabilizers, flame retardants and reinforcements. Hence, they are referred to in this study as TSCs. TSCs are used in devolatilization to remove solvents and in reactive extrusion, where in-situ chemical reactions exist within the extrusion process [23]. The TSC is considered the most widely used twin screw processing equipment. It was patented in the 1940s by Erdmenger at Bayer AG and was a subject of continuous development at Werner & Pfleiderer in the 1950s. The TSC has a variety of applications including [48]:

- Plastification, mixing, homogenization and granulation of polymers
- Dispersing of pigments and additives
- Homogenization of melts with wide differences in viscosity
- Blending different polymer resins

- Performing reactive processing such as, addition- and polycondensation polymerization
- Concentration of polymer solutions
- Mixing polymers with reinforcers and fillers such as glass and carbon fibers, talc, calcium carbonate
- Modification of polymers through incorporation of functional additives such as flame retardants and plasticizers

2.5.6 Estimating specific consumed energy and residence time

To estimate the specific energy consumed during the kneading and TSC processes, as well as the residence time of the TSC process, the following equations were utilized for the calculations:

Kneading process

Specific consumed energy of the kneading process (E_k), calculated in kJ/kg and converted to kW·h/kg can be directly calculated for kneading process according to the following equation [58]:

$$E_k = \frac{M_d \cdot \omega \cdot t_k}{m} \quad (1)$$

Where M_d refers to the average torque in N·m, ω refers to the angular velocity of the rotor blades in rad/s, t_k refers to the kneading time in seconds and m refers to the mass of weighted sample in kg.

TSC process

The following equations are utilized for estimating the specific energy consumed during the TSC process (E_{TSC}) and the mean residence time (t_{mean}) of TSC.

- Specific consumed energy (E_{TSC}) [84]:

$$E_{TSC} = \frac{P_A}{\dot{m}} \quad (2)$$

$$P_A = P_M \cdot \tau_r \cdot \frac{n_A}{n_M} \cdot 0.97 \quad (3)$$

where P_A is the applied power in W, $\dot{m}$ is the mass flow rate in kg/h, P_M is the maximum motor power capacity in W, τ_r is the percent of torque used as compared to full machine torque, n_A and n_M are the applied and maximum compound speeds in rpm and 0.97 is an assumed approximate percentage for gear box efficiency.

- Estimated free volume in the compounder (V_o) [23]:

$$V_o = A_o . L \quad (4)$$

$$A_o = A_b - A_s \quad (5)$$

Where A_o, A_b and A_s are the screw element open area, barrel area and screw area in m^2. L is the screw length in m.

- Mean residence time (t_{mean}) [23]:

$$t_{mean} = \frac{V_o}{\dot{V}} \quad (6)$$

Where $\dot{V}$ is the volume flow rate in m^3/s.

2.6 Automotive interior trims: A promising application

When it comes to automotive industry, continuous research is devoted to develop competitive materials that can provide optimum integration of lightweight and excellent functional properties; automotive interior component applications, Figure 20, are no exception. In today's vehicles, developing low cost, lightweight, aesthetic materials with highest performance standards in terms of scratch and corrosion resistance, stiffness and thermal stability is crucial. Equally important is the pursue of decreased material and energy inputs as sustainable solutions [34]. The company Borealis, a leading provider of chemicals and innovative plastic solutions, is one of the major suppliers of PP and thermoplastic polyolefin (TPO) compounds, designed specifically

to meet the specifications of automotive interior applications, as shown in Figure 21. Borealis produces tailored mineral-filled PP copolymer compounds as a commercial compound for interior trim applications. The properties of an example, 'ME268AI' compound, are listed in Table 11.

Figure 20: Automotive interior applications of PP and TPO based compounds [34].

Figure 21: Automotive interior door trim [34].

Table 11: Commercial mineral-filled PP copolymer for interior trim application, Borealis [34].

Grade code	ME268AI
Filler content (wt.-%)	20
Density (kg/m^3)	1050
MFR (230 °C/ 2.1 kg) (g/10 min)	12
Flexural modulus (MPa)	2400
Tensile stress at yield (MPa)	26
Impact Charpy notched at 23°C (kJ/m^2)	6
Impact Charpy notched at -20 °C (kJ/m^2)	2.5
HDT B (0.45 MPa) (°C)	100
Shrinkage indication (%)	1.1
Typical applications	Interior trims

2.7 Life cycle assessment (LCA)

2.7.1 Principle of LCA

LCA is a systematic set of procedures that aim at assessing the environmental effects assignable to a certain product or service. This is done through the quantification of all inputs and outputs of material flows and how they can impact the environment. This information is invaluable for improving processes and lay a strong background for decision making.

The term ‘Life cycle’ refers to the holistic assessment of the product existence stages (‘Cradle-to-grave’ concept): Raw material, distribution, use and disposal. This includes all the intervening transportation steps relevant to the product existence as well. LCA procedures are part of the ISO 14000, the environmental management standards and its framework is defined according to the ISO 14040 (2006) [50]; [105]

2.7.2 LCA Framework

As shown in Figure 22, the LCA process is divided into four main phases according to ISO 14040-14043: Scope and goal, life cycle inventory, life cycle impact assessment and data interpretation [105].

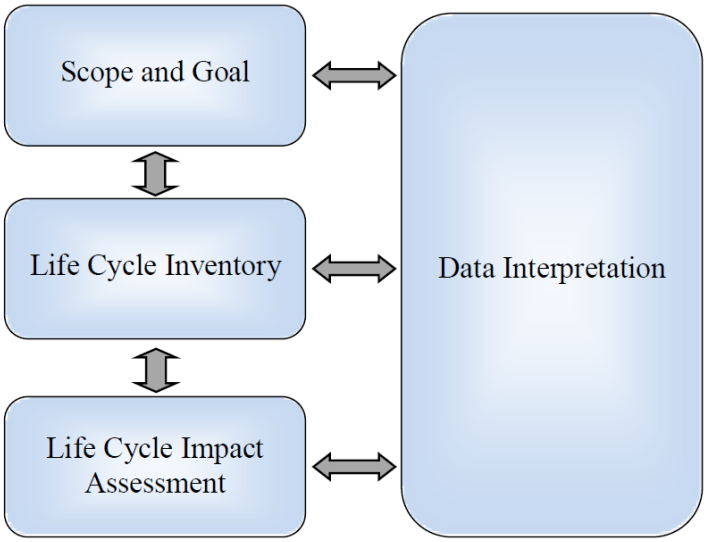

Figure 22: LCA framework (ISO 14040, 2006) [105].

2.7.2.1 Scope and goal definition

The first phase of LCA deals with defining the scope, the constraints and the goal of the study, taking into consideration the limitations of the study and the included/excluded parameters. In addition, the audience and boundary conditions are defined within this phase. An important term, the 'functional unit', defines accurately what is being studied and quantifies the services delivered by the product. The 'functional unit' is considered an important basis upon which alternative goods or services can be analyzed and compared [50]; [105].

2.7.2.2 Life cycle inventory analyses

Life cycle inventory involves the construction of a descriptive model or diagram, where the input/out inventory flows from/to the nature are formulated. Inventory flows include inputs of the water, energy and raw material and output releases to the air, land and water [50]; [105].

2.7.2.3 Life cycle impact assessment

Life cycle impact assessment phase deals with the evaluation of the significance of the potential environmental impacts in the study. This is done through the selection of impact categories, category indicators and characterization models. This is followed by sorting and classification of the inventory parameters into the respective impact

categories. Finally, an impact measurement is performed, where the categorized life cycle inventory flows are characterized into common equivalence units which can be summed to provide an overall impact measurement [50]; [105].

2.7.2.4 Data interpretation

In the data interpretation phase, the results of the inventory analyses and impact assessment are evaluated, which allows the investigator to derive conclusions and recommendations for the study. According to ISO 1040:2006, the interpretation should include (a) identification of significant results, (b) consideration of completeness, consistency and sensitivity of results and (c) providing conclusions, limitations and recommendations [50]; [105].

2.7.3 Carbon footprint screening

The carbon footprint screeing (CFS) may be defined as “a measure of the exclusive total amount of carbon dioxide emissions that is directly and indirectly caused by an activity or is accumulated over the life stages of a product.” [76]. Another definition might be “the total set of greenhouse gas emissions caused by an individual, event, organization, product and expressed as CO_2e” [104].

In fact, the worldwide attention and focus on the emission of the environmental impact of the emission of CO_2 and other greenhouse gas (GHG) emissions have drawn more interest towards CF. A combination of CF and LCA is utilized for a systematic analyses regarding the influence on the environment throughout the entire life cycle of a product or service. An end-to-end analyses consider all raw materials, transportation, production procedures, utilization and final disposal of the product. Accordingly, the carbon footprint at the product level can be thought of as a specialized application of the LCA criteria with a focus on GHG emissions. In other words, CF methodology may be considered as a simplified LCA restricted to a single category: Global Warming and GHG emissions [50]; [82]. According to Pattara et al. [75], more than 2500 scientific papers have been published on CF since 2000.

2.7.4 Modelling with SimaPro©

The software SimaPro© is one of the most widely recognized tools for establishing the LCA and product analyses. It was developed by PRé Consultants in Holland. The first version of this software was developed in 1990 as a tool for collecting, analyzing and monitoring the environmental impact of products and services brought by the market. To adequately analyze and compare a product, information about its origin, production, utilization and disposal are provided. At the end, the environmental impact of the product cycle is simulated and analyzed by SimaPro [47].

The software calculations and analyses are based upon the measures of the ISO 14040. It facilitates the development of the LCA via the following functions [47]:

- Graphic modelling of the investigated systems as a process chain, tree or net
- Utilizing an exclusive database of standard processes from different areas (energy generation, transportation and disposal). There is also a possibility to adopt custom processes and integrate them with the database
- Approved moles for the different analyses and modules are pre-installed. The visualization of the results can be rendered as a diagram or a table form
- Calculation of sensitivity analyses, i.e. Monte Carlo simulation (MCS).

2.7.5 Data uncertainty and sensitivity analyses

All input and output data in the LCA do not come in absolute values, but rather with some uncertainty. Such uncertainty emerges from the fact that there are always differences between the pre-installed or model data and real data in terms of representativeness, allocation basis, future scenarios and functional unit. For instance, the resources used for undertaking an LCA study, like energy data and manufacturing costs, might differ from the actual values. Therefore, sensitivity analyses, performed via statistical simulation analyses, such as MCS, are utilized to make sure that such uncertainties are taken into consideration within LCA findings [40]; [47].

2.7.6 Monte Carlo Simulation analyses

The Monte Carlo method was originally developed in the 1940s by physicists working on the nuclear projects in the Los Alamos National Laboratory. It may be defined as “a

broad class of computational algorithms that rely on random sampling to obtain numerical results" [46]. The name 'Monte Carlo' is adopted from the games of chance, a popular attraction in Monte Carlo in Monaco [2].

In science- and engineering related fields, MCS is used for conducting uncertainty analyses, optimization and reliability studies, allowing simulation of physical and mathematical systems. The simulation is typically necessary for handling data uncertainties, where MSC converts uncertainties in the input variables of the LCA model into probability distributions. These distributions are combined and random values resulting from a large number of iterations are selected from them. Therefore, the simulated model is recalculated many times and a useful output probability distribution is rendered [2].

Characteristics

- Defining the domain of several combined inputs for calculating the probability distribution of one or more outputs
- Inputs are generated randomly from the domain, allowing creation of different probability distributions
- As a stochastic method, independent, non-correlated random numbers are to be used for performing a deterministic computation using the inputs.
- Rendering the output as a range instead of a single value, aggregating the findings of individual computations

Statistical distributions of MCS

For applying MCS in LCA, the uncertainty data must be translated into a standard distribution. In SimaPro, the following four distributions are utilized [2]; [47]:

Range distribution: This distribution is used when an equal probability in a range defined by a minimum and maximum value. For instance, throwing a dice follows a range distribution between 1 and 6.

Normal (Gaussian) distribution (bell-shape): This distribution is defined by the mean (best guess value) and the standard deviation (SD). In SimaPro, the value 2xSD is required instead. The specification of SD is important as the 95 % confidence interval

lies between -2xSD and +2xSD, meaning that only 2.5 % of the total points lays above or below the specified range.

Triangular distribution: This is an alternative for the normal distribution but with the difference that very high or low points cannot occur. It is specified by a best guess value, a maximum and a minimum.

Lognormal distribution: This distribution is the one used for LCA analyses. They occur upon multiplication of the 'normal distribution' fitted values, which occurs in LCA. In SimaPro, the variance or the square of the standard deviation (σ^2) and the best guess value are specified for this purpose.

3 Experimental Work

3.1 Utilized materials

3.1.1 Polypropylene copolymer as a base polymer

Borealis PP BB412E block copolymer grade, provided by the company Borealis, Austria, was utilized throughout this study as a base polymer. The properties of BB412E grade and its recommended extrusion zone temperatures are provided in Table 12 and Table 13 [5]. The recommended processing temperatures provided in the data-sheet as well as peer-experience with this grade were the base for selection the proper processing temperatures for kneading and TSC runs. It was experimentally assured that the selected temperature rendered a quality mixture that is free of voids, moisture and thermal defects.

Table 12: Properties of BB412E PP grade [5].

Property	Typical Value Data should not be used for specification work	Test Method
Density (23 °C)	900 kg/m3	ISO 1183
Melt Flow Rate (230 °C/2,16 kg)	1,3 g/10min	ISO 1133
Melt Flow Rate (190 °C/5 kg)	2,5 g/10min	ISO 1133
Tensile Modulus	1.300 MPa	ISO 527
Tensile Strain at Yield (50 mm/min)	8 %	ISO 527
Tensile Stress at Yield (50 mm/min)	28 MPa	ISO 527
Charpy Impact Strength, notched (23 °C)	25 kJ/m²	ISO 179/1eA
Charpy Impact Strength, notched (-20 °C)	5 kJ/m²	ISO 179/1eA

Table 13: Recommended extrusion zone temperatures and the melt temperature of the BB412E PP grade [5].

Extrusion	
Cylinder	190 - 230 °C
Head	200 - 230 °C
Die	200 - 230 °C
Melt temperature	200 - 230 °C

3.1.2 Blast furnace slag as a functional filler

BFS was provided by company voestalpine Stahl GmbH, Austria. Figure 23 shows that the as-received ACBS is in the form of <4 mm gravel-like aggregates while the as-received GBS is in the form of fine sand [103]. The chemical composition analyses of both BFS types were discussed in detail at Chapter 4.

Figure 23: As-received ACBS (left) and GBS (right) [94].

3.1.3 BFS modification

Upon collaboration with the Chair of Chemistry of Polymeric Materials, Montanuniversitaet Leoben (LCK-MUL), two coupling agents were chosen for BFS:

- 3-Methacryloxypropyltrimethoxysilane (MPS)
- Vinyl-based vinylethoxysiloxanehomopolymer silicon (VES)

The MPS coupling agent is considered one of the most common used coupling agents for improving the adhesion between polymers and minerals [14]. In glass and mineral-filled PP systems, the utilization of this silane type as coupling agents has been frequently reported [43]; [51]; [110]; [109]; [111]. The structure and properties of MPS are shown in Figure 24 and Table 14, respectively. According to the company Gelest Inc., vinyl-based vinylethoxysiloxanehomopolymer silicon (VES) is one of the recommended coupling agents to use in polypropylene systems. It was chosen in this study for comparison with MPS. Figure 25 shows the structure of VES [97].

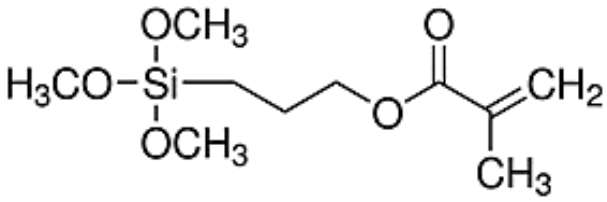

Figure 24: Structure of 3-methacryloxypropyltrimethoxysilane [1].

Table 14: 3-methacryloxypropyltrimethoxysilane properties [88].

Molecular weight g/mol	Specific gravity 25 °C	Refractive index 25 °C	Boiling point (°C)	Minimum covering area (m^2/g)
248.4	1.04	1.429	255	314

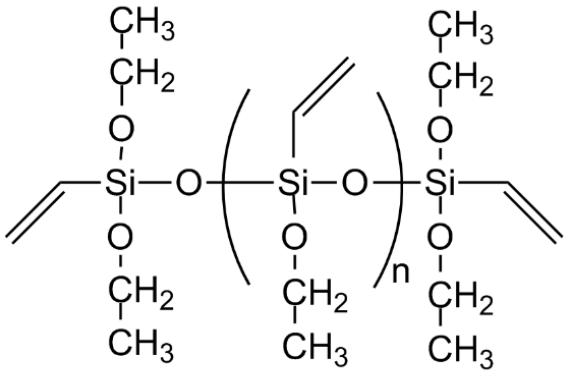

Figure 25: Structure of vinylethoxysiloxanehomopolymer silicon [97].

3.2 Preparation of BFS filler for compounding

3.2.1 Milling of the as-received BFS

The purpose of the milling process was to refine the as-received slags into three mesh sizes of each type of BFS: <71, <40 and <20 µm. The process was carried out using a ball mill available at the technical center of the Chair of Mineral Processing - Montanuniversitaet Leoben (LAV-MUL). The weight of the milling balls was 8.97 kg. The free volume provided by the milling media was calculated as 473 cm^3. Milling was

achieved at the speed of 1.08 1/s, corresponding to 68 % of the maximum speed capacity of the machine. Table 15 shows the milling duration for each mesh size [103].

Table 15: The milling duration required for producing each mesh size [103].

BFS size range (µm)	<71	<40	<20
Milling time (min)	30	30 to 60	60

3.2.2 Sieving of the milled BFS

After the ball milling, BFS with <71, <40 and <20 µm particle sizes were produced via different mesh-sized sieves from the company Haver & Boecker. The analyses were performed at LAV-MUL. The fine slag aggregates, which are the final products, as well as the coarse ones were preserved in air-tight sealed containers for further investigation. The product <20 µm was produced via an Alpine-air jet sieve. The amounts of compounding-ready BFS products illustrated in Table 16 were produced and transferred to PCCL for compounding [103].

Table 16: The amounts of compounding-ready BFS [103].

ACBS		GBS	
Fraction (µm)	Weight (g)	Fraction (µm)	Weight (g)
<71	489	< 71	613
<40	545	< 40	499
<20	534	< 20	368

3.2.3 Modification procedure

BFS modification was performed at the LCK-MUL for <71µm-GBS and <71µm-ACBS slag. The modification procedure is as follows: For 100 g of slag, the coupling agent amount of 2 wt.-% on the basis of filler was dissolved in 98 g of the ethanol mixture (93.1 g methanol, 4.9 g distilled water and three vinegar drops with ph~4.5-5). The mixture was left for five minutes and then mixed with the slag. Methanol was expelled by heating in an oil bath (100° C) with back-cooling, followed by 30 minute air-cooling and filtering. Finally, the mixture was further purged with ethanol and air-dried for 20 hours at room temperature

3.3 Utilized equipment and testing parameters

3.3.1 Laboratory scale rotor-blade, internal mixing kneader

As shown in Figure 26, kneading was performed via Haake Polylab System 3000P laboratory kneader with co-rotating steel rotor blades (Thermo Fischer Scientific Inc., Waltham, USA). PP granulates were added while the blades were rotating. BFS filler was always added five minutes after the addition of the polymer granulates. Except for the kneading parameter experiment (section 3.6.2.2), the kneading duration and speed of 10 minutes and 60 rpm, respectively, were fixed throughout this study.

Figure 26: Haake Polylab system 3000P laboratory kneader.

3.3.2 Co-rotating, twin screw extruding compounder

The twin screw compounding stages were performed via a ZSK 25 gravimetric-fed, co-rotating TSC with a screw diameter of 25 mm and screw length of 40D (Werner & Pfleiderer, Germany), as shown in Figure 27. The compounding parameters are listed in Table 17. The ZSK 25 intermeshing twin screws consist of three kneading blocks that are located at the following distances from the hopper: 300, 500 and 860 mm, with the third block having three medium pitch, right-handed kneading disks [108]. PP granulates and BFS were starve-fed into the TSC. TSC compounding was successfully performed with cooperation of Mr. Alexander Eder (LKV-MUL)

Figure 27: ZSK 25 twin screw extruder.

Table 17: Twin-screw compounding parameters

Process parameters	Value
Zone 1 Temperature (°C)	160
Zone 2 Temperature (°C)	180
Zone 3 Temperature (°C)	190
Zone 4 Temperature (°C)	200
Zone 5 Temperature (°C)	200
Die Temperature (°C)	210
Screw speed (rpm)	200
Melt flow rate (kg/h)	10

Figure 28 shows the compounder's control panel, where parameters like filler loading and mass flow rate are adjusted. The ventilation section of the compounder is attached to a suction pump to get rid of the unwanted process volatiles. As the molten polymer strand leaves the 3-mm rod die, it was directly guided into a water bath, as shown in Figure 29. The cooled compound strand was then pelletized via an air-knife equipped strand pelletizer (Accrapak Systems Ltd., Series 750), the pelletization was performed at a rate of 10 m/min, as shown in Figure 30. The compound was subsequently subjected to compression- or injection molding.

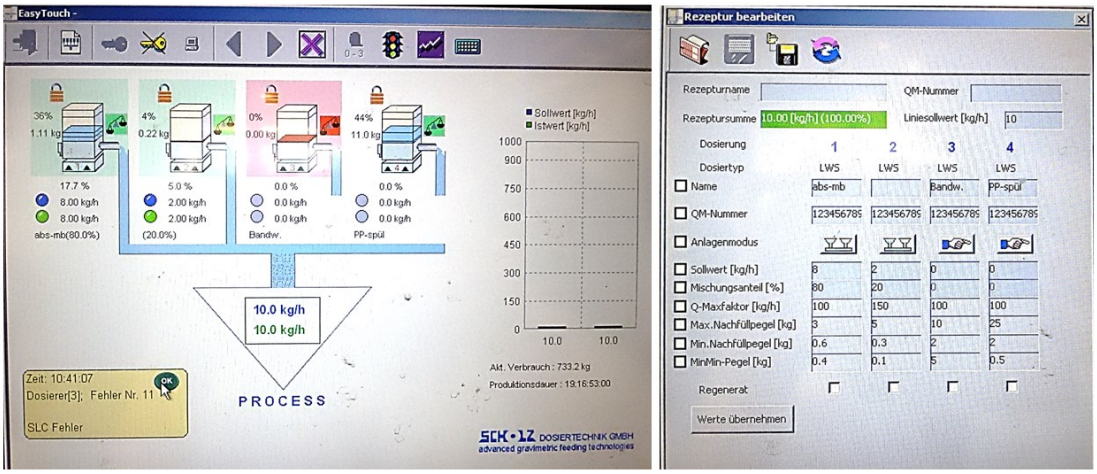

Figure 28: Compounding parameters, shown in the TSC control panel.

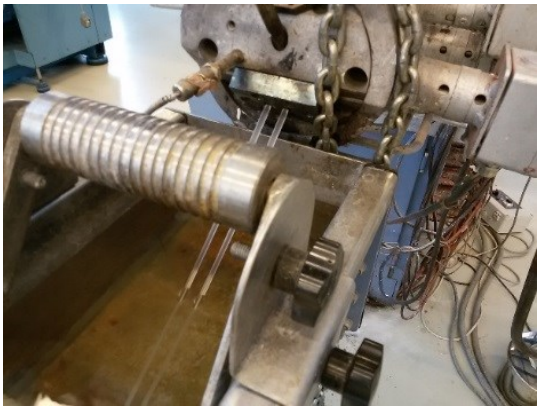

Figure 29: The molten PP strand shown during water bath cooling.

Figure 30: Pelletization of the PP strand into granulates.

3.3.3 Compression molding equipment

Compression molding was performed via a Collin hydraulic vacuum press (Collin 200 PV, Dr. Collin, Germany) shown in Figure 31. The viscous compound was removed from the kneader and pressed under vacuum into 0.15 x 0.15 x 0.004 (and 0.002) m^3 plates for testing. The compression molding run was programmed into four phases, where the temperature, pressure and time parameters for each phase are:

- Phase 1 (195, 1, 6)
- Phase 2 (195, 65, 2)
- Phase 3 (195, 100, 1)
- Phase 4 (30, 100, 10)

Figure 31: Dr. Collin hydraulic vacuum press.

3.3.4 Injection molding

Universal dog-bone shaped samples were produced via the injection molding machine ALLROUNDER 470A 1000-400 alldrive (Arburg, Germany) shown in Figure 32. Injection molding parameters for the neat PP, the slag filled compounds and the reference 'ME268AI' are listed in Table 18. No difficulties were experienced during the injection molding runs. The 'ME268AI' reference required a decreased injection pressure due to its relative brittleness compared to the neat PP and the slag filled compounds. The temperatures of each zone, however, remained unchanged for all the

compounds. The injection molding processing was kindly performed by Eng. Rudolf Schatzer (LKV-MUL).

Figure 32: ALLROUNDER 470A Injection molding machine.

Table 18: Injection molding parameters

Process parameters	Neat PP & BFS-PP compounds	Reference (ME268AI)
Hopper Temperature (°C)	40	40
Zone 2 Temperature (°C)	190	190
Zone 3 Temperature (°C)	200	200
Zone 4 Temperature (°C)	205	205
Zone 5 Temperature (°C)	210	210
Nozzle Temperature (°C)	220	220
Injection pressure (bar)	500	370
Rest cooling time (s)	25	25

3.4 Testing of BFS and PP-BFS compounds

3.4.1 Shear-rheology investigation

For the investigation of the shear rheological paramters, a Physica MCR 501 rheometer (Anton Paar GmbH, Austria) was utilized, as shown in Figure 33. For all compounds, a plate-plate configuration with a plate diameter of 25 mm and gap of 1 mm, was utilized. The used samples' dimensions were 2 mm in thickness and 20 mm in diameter and the test was performed under nitrogen atmosphere to prevent degradation. Except for experiment 2, the test temperature for neat PP and the

compounds was maintained at 200° C, while the temperature setting for experiment 3 was 180° C. Two testing modes were employed for the shear rheology analyses: (1) Dynamic strain sweep to identify the viscoelastic region and (2) dynamic frequency sweep to investigate the complex shear viscosity, storage and loss moduli. A frequency range of 0.1 - 500 1/s was maintained for all compounds and all measurements were confirmed to be within the viscoelastic region of PP. The measurements were done, thanks to the invaluable assistance of Dipl.-Ing. Dr.mont. Ivica Duretek, Ms. Julia Gössmann and Ms. Sabrina Winkler.

Figure 33: Physica MCR 501 rheometer.

3.4.2 Thermal investigation

3.4.2.1 Differential scanning calorimetry (DSC)

The thermal behavior was investigated via a DSC-4000 differential scanning calorimeter (Perkin Elmer, USA), Figure 34. The experiments were conducted using 10 mg samples sealed in aluminum pans. Heating and cooling rates were fixed at 10 K/min. The samples were subjected to one cooling and two heating cycles. The degree of crystallinity, DOC, was calculated as the ratio between the melting enthalpy of the sample and the melting enthalpy of a 100 % crystalline PP, which was taken as 209 J/g according to Marenille et al. [56]. The DSC measurements were kindly performed by Ms. Astrid Rauschenbach (PCCL).

Figure 34: DSC-4000 Differential scanning calorimeter.

3.4.2.2 Thermal conductivity (ASTM E1530)

As illustrated in Figure 35, thermal conductivity testing was performed via a DTC-300 thermal conductivity analyzer (TA-instruments, Germany). The method used for testing was guarded heat flow meter. This equipment measures the thermal conductivity accordingly to the ASTM E1530 standard test, which is applied for a variety of materials including polymers, glass, composites and some metals. The sample used for this test had a cylindrical shape with a diameter of 50 mm and a thickness of 2 mm. Thermal conductivity measurements were performed by Ms. MSc. Andrea Wanner (PCCL)

Figure 35: DTC-300 equipment.

3.4.3 Mechanical investigation

3.4.3.1 Tensile testing (Standard ISO 527-1)

A Zwick/Roell station (Zwick and Co.KG, Germany) was utilized for the tensile testing experiments according to standard ISO 527-1, as shown in Figure 36. A strain rate of 50 mm/min was utilized for recording the strength- and strain at break values, while a strain rate of 1 mm/min was used for the tensile modulus values. Samples were machined out of the compression molded, 0.004 m-thick plates to standard dog-bone samples. The tensile test was performed at room temperature and the data were evaluated using testXpert II software. The tensile testing was kindly performed by Mr. Herbert Fladenhofer (PCCL).

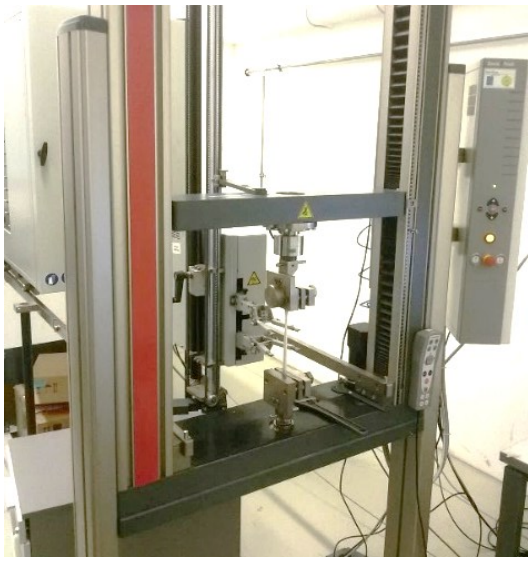

Figure 36: Zwick/Roell tensile testing station.

3.4.3.2 Charpy impact testing (ISO 179)

The Charpy impact test was conducted with a Ceast Resil 25 pendulum (Ceast S.p.A., Italy), Figure 37, according to the ISO 179 standard. The test was performed for un-/notched samples at 23 and -30°C.The test was kindly performed by Mr. Dipl.-Ing. Dr.mont. Florian Arbeiter (LWPK-MUL).

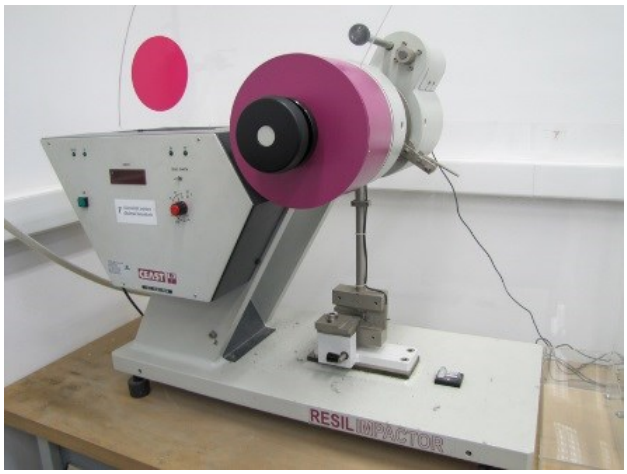

Figure 37: CEAST Resil Charpy impact apparatus [13].

3.5 Characterization of BFS and PP-BFS compounds

3.5.1 Optical microscopy

To visually investigate the particle distribution of BFS, rectangular samples were sliced out of the compression-molded plates and were mounted in acrylic molds and manually ground via grinding papers with different polish grades up to 1200. The ground samples were then characterized via the Alicona InfiniteFocus microscopy equipment (Alicona Imaging GmbH, Austria), shown in Figure 38. The optical characterization was performed with the kind assistance of Mr. Robert Hinterberger (PCCL).

Figure 38: Alicona InfinitFocus IFM G4 microscopy.

3.5.2 Scanning electron microscopy and energy dispersive X-ray analyses

SEM micrographs were captured and EDX analyses were performed via TESCAN VEGA scanning electron microscopy (SEM) (EO Elektronen-Optik-Service GmbH, Germany) with a tungsten electrode in scanning electron (SE) and backscatterd electron (BS) modes, as shown in Figure 39. Samples were gold-sputtered prior to characterization and mount on a single-sample holder into the SEM chamber. The chamber was vacuumed for nearly 10 min prior to characterization. All compounds were characterized at an electron gun voltage of 5 kV and a working distance (WD) of 7 mm. The characterization was performed by Ms. MSc. Dr. tech. Sandra Pötz.

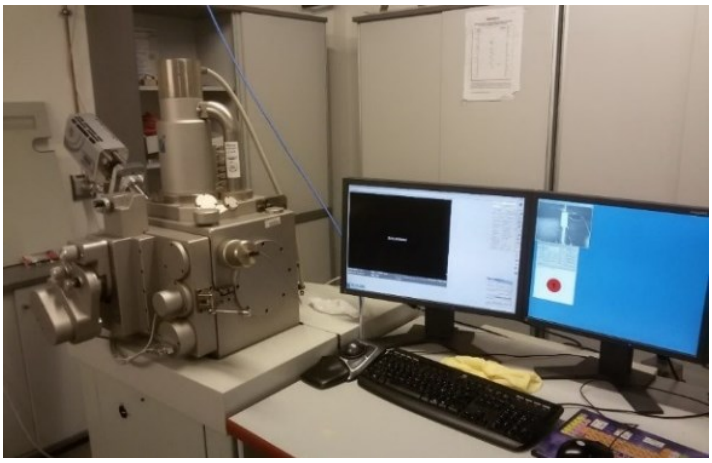

Figure 39: EOScan Tescan VEGA SEM microscopy.

3.5.3 Particle size distribution

The cumulative particle distribution analyses of BFS were kindly performed by Mr. Heigl (voestalpine Stahl GmbH, Austria) via CILAS 920 particle size analyzer, shown in Figure 40. A laser diffraction technique was used for analyzing the distributions. The test was done in wet mode using isopropyl alcohol as a dispersing agent. The test measuring range was 0.3 – 400 µm.

Figure 40: CILAS 920 particle size analyzer [16].

3.6 Experimental trial plans

3.6.1 Terminology and compound codes

An abridged terminology of 'X.(m)A(/G).Y A(/B)', is employed throughout this thesis for the compounds, where 'X' refers to BFS loading, 'A' or 'G' refers to slag type, 'Y' refers to BFS particle size range and A/B are the molding type, whether compression- or injection molding. For instance, the '20A71 K, CM' terminology means that 20 wt.-% of <71 μm-ACBS type is kneaded with PP then compression molded. The addition of the small letter 'm' before the slag type indicates that the slag is modified with the MPS coupling agent. Table 19 illustrates the compound codes utilized throughout this thesis.

Table 19: Compound codes utilized throughout this thesis

Code	Explanation
Neat PP (Neat PP K,CM)	Neat PP subjected to a laboratory kneading run then compression molded
Neat PP TSC (Neat PP TSC,CM)	Neat PP subjected to a TSC run then compression molded
Neat PP TSC,IM	Neat PP subjected to a TSC run then injection molded
20A71 (20A71 K,CM)	The terminology without any processing codes is the default setting (unmodified BFS, kneading followed by compression molding)
20A20 60, 10	The '20A20'compound is kneaded at a kneading speed of 60 rpm for and duration of 10 minutes then compression molded
20A71 TSC (20A71 TSC,CM)	The terminology without molding type is the default setting (unmodified BFS, TSC followed by compression molding)
20A71 VES/MPS	the '20A71' compounds is kneaded with MPS- or VES-modified slag then compression molded
20mA71 TSC,CM	The slag is modified with the chosen MPS coupling agent, twin-screw compounding is utilized followed by compression molding (this terminology is used in experiment 5)
20mA71 TSC,IM	Same as previous and the compound is injection molded (this terminology is used in experiment 5)

3.6.2 Basic study

3.6.2.1 Experiment 1: Influence of untreated BFS parameters

Purpose and criteria

The experiment purpose was to investigate the influence of the listed unmodified-BFS parameters on the rheological, thermal and mechanical properties of PP. Table 20 illustrates the chosen parameters and the tested compounds.

Table 20: Experimental plan for experiment 1.

Condition	Material	Compound Code	Filler parameters		
			Size/distribution (µm)	Type	Loading (wt.-%)
1	Neat PP	Neat PP	-	-	-
2	PP-BFS	10A71	<71	ACBS	10
3		10G71		GBS	
4		20A71		ACBS	20
5		20G71		GBS	
6		30A71		ACBS	30
7		30G71		GBS	
8		10A40	<40	ACBS	10
9		10G40		GBS	
10		20A40		ACBS	20
11		20G40		GBS	
12		30A40		ACBS	30
13		30G40		GBS	
14		10A20	<20	ACBS	10
15		10G20		GBS	
16		20A20		ACBS	20
17		20G20		GBS	
18		30A20		ACBS	30
19		30G20		GBS	

Experiment outcome

Analyzing the findings of this experiment was fundamental for obtaining a concrete overview of the behavior of BFS within the PP matrix. The findings of this experiment were fundamental to understand the significant filler factors affecting each of the three property category.

3.6.2.2 Experiment 2: Influence of kneading parameters

Purpose and criteria

The purpose of this experiment was to investigate the effect of two kneading processing parameters, kneading speed and duration, on the rheological, thermal and mechanical properties of a representative PP-BFS compound. The chosen compound for this experiment was PP filled with 20 wt.-% of unmodified <20 µm BFS (20A20). The reason for choosing this particular slag type and distribution was based on its availability at this stage. The choice of 20 wt.-% filler loading was chosen due to the comparison potential with the ME268AI commercial compound, having the same mineral filler loading.

Experiment outcome:

Analyzing the findings of this experiment was important to investigate the influence of the kneading process parameters, kneading speed and duration, on the rheological, thermal and mechanical properties of the '20A20' compound. In addition, the correlations between E_k, M_d, the thermal and mechanical properties, i.e. DOC and the Young's modulus, were also investigated. The kneading of neat PP and the compounds was performed at a fixed mass temperature of 195° C and alternating kneading speed/duration parameters, as shown in experimental trial plan of Table 21.

Table 21: Experimental plan for experiment 2 (Mass temperature = 195 °C).

Condition	Material	Compound code	Kneading speed (rpm)	Kneading duration (min)
1	Neat PP	Neat PP- 60, 10	60	10
2	PP-BFS	20A20 - 60, 10	60	10
3		20A20 - 60, 20	60	20
4		20A20 - 90, 10	90	10
5		20A20 - 90, 20	90	20
6		20A20 - 120, 10	120	10
7		20A20 - 120, 20	120	20

3.6.2.3 Experiment 3: Comparative study (kneading versus TSC)

Purpose and criteria

The purpose of this experiment was to compare the influence of the processing approach itself, kneading versus TSC, on the rheological, thermal and mechanical properties of chosen PP-BFS compounds. For this regard, three compounds were chosen: 20A71, 20G71 and 20A20. The compounds were chosen based on the following considerations:

- Ease of processability at LAV (<71 µm is much less time consuming in terms of milling and sieving compared to <20 µm), knowing that TSC consumes considerable amount of materials compared to the laboratory kneader
- Comparisons of the commercial ME268AI (20 wt.-% loading)
- Utilization of available <20 µm – ACBS from experiment 2

Experiment outcome

Besides investigating the influence of each compounding approach, kneading and TSC, this experiment allowed calculating key process factors such as E_k, E_{TSC} and $t_{mean,TSC.}$ Table 22 shows the accomplished trial plan. TSC parameters were previously illustrated in section 3.3.2.

Table 22: Experimental plan for experiment 3.

Condition	Compound code	BFS compounds		
		Weight fraction (wt.-%)	Type	Particle size range (µm)
1	20A71	20	ACBS	<71
2	20A20			<20
3	20G71		GBS	<71

3.6.3 Advanced study

3.6.3.1 Experiment 4: Testing two coupling agents, MPS and VES

Purpose and criteria

In the advanced study experiments, only 20A71 and 20G71 compounds were chosen for The purpose of this experiment was to investigate the influence of two coupling agents, MPS and VES, on the rheological, thermal and mechanical properties of two selected compounds: 20A71 and 20G71, based on the considerations described in experiment 3. Kneading parameters were previously illustrated in section 3.3.1.

BFS modification

For 100 g of slag, the silane coupling agent (2 g, corresponding to 2 wt.-% on the basis of filler) was dissolved in 98 g of ethanol mixture (93.1 g methanol, 4.9 g distilled water and three vinegar drops with ph~4.5 - 5). After addition of the silane, the mixture was left for five minutes and then mixed with the slag. Methanol was expelled by heating in an oil bath (100° C) with back-cooling, followed by 30 minute air-cooling and filtering. Finally, the mixture was further purged with ethanol and air-dried for 20 hr at room temperature.

Table 23: Experimental plan for experiment 4.

Code	BFS type	BFS particle size (µm)	BFS weight fraction (wt.-%)	Coupling agent	Kneading duration (min)	Kneading speed (RPM)
20A71VES	ACBS	<71	20	VES	10	60
20A71MPS				MPS		
20G71VES	GBS			VES		
20G71MPS				MPS		

Experiment outcome

Based on the findings of this experiment, only one coupling agent, MPS, was chosen for BFS modification in subsequent experiments because the ‘20G71-MPS’ compound showed 36 % higher strain compared with the VES-counterpart. This and other findings were described in detail at the ‘Findings of Experimental Work’ chapter.

3.6.3.2 Experiment 5: Final modified-BFS filled compounds

Purpose and criteria

The purpose of the experiment was to evaluate the influence of the post compounding processing (compression- or injection molding) on the rheological, thermal and mechanical properties of the following compounds. Table 24 shows the accomplished trial plan, where the compounds were subjected to TSC. After compounding, the compounds were either compression- (CM) or injection molded (IM). As previously noted in the terminology section 3.6.1, the compounds are noted as

- Neat PP
- 20mA71 TSC, CM (or IM)
- 20mG71 TSC, CM (or IM)
- ME268AI (Reference compound)

Table 24: Experimental plan for experiment 5.

Compound code	BFS compounds			
	Weight fraction (wt.-%)	Type	Particle size range (μm)	Coupling agent
Neat PP TSC, CM/IM	-	-	-	-
20mA71 TSC, CM/IM	20	ACBS	<71	MPS
20mG71 TSC CM/IM		GBS		
ME268AI CM/IM	-	-	-	-

Experiment outcome

Table 24 shows the accomplished trial plan. Two slag-filled PP compounds were compounded via TSC, where BFS was modified by MPS coupling agent. In addition, neat PP was also subjected to one TSC pass for comparison. Neat PP, slag-filled and pre-compounded 'ME268AI' compounds were subsequently injection molded, tested and compared. TSC and injection molding parameters are previously illustrated in sections 3.3.2 and 3.3.4.

4 Findings of Experimental Work

4.1 BFS analyses

The preparation and characterization of the <71, <40 and <20 μm GBS and ACBS groups were performed in the frame of a bachelor thesis, which was carried out by Weninger [103] at the LAV-MUL and cited in section 4.1.1.

4.1.1 As-received BFS

4.1.1.1 Determination of moisture-content of the as-received BFS

As reported by Weninger [103], representative samples from both GBS and ACBS types were collected and characterized. The moist slags were filled in containers and weighed. Afterwards, the slags were dried and refilled in the same containers then weighed. The measurement findings are shown in Table 25. The moisture content for each slag type was calculated via the following equation:

$$\text{Moisture content}(\%) = \frac{m_{\text{moist slag}} - m_{\text{dried slag}}}{m_{\text{dried slag}}} \times 100\% \quad (7)$$

Table 25: Moisture-content determination of the as-received BFS samples [103].

	ACBS	GBS
$m_{container}$ (g)	360.04	507.96
$m_{moist\ slag\ filled\ container}$ (g)	1229.63	1099.99
$m_{dried\ slag\ filled\ container}$ (g)	1201.70	1072.56
M_{water} (g)	27.93	27.43
$m_{moist\ slag}$ (g) ($m_{moist\ slag\ filled\ container} - m_{container}$)	869.59	592.03
$m_{dried\ slag}$ (g) ($m_{dried\ slag\ filled\ container} - m_{container}$)	841.66	564.60
Moisture content (%)	3.32	4.86

4.1.1.2 Particle-size distribution of the as-received BFS

GBS and ACBS were dried at 160° C and sealed and then investigated via a particle-size analyzer. Figure 41 shows the cumulative percent distribution of the as-received GBS and ACBS particles, reported by Weninger [103]. The curves indicate that the

D50 of both types was almost 1 mm. The shift of ACBS curve towards lower particle size indicated that ACBS contained higher amount of <100 μm particles compared to GBS.

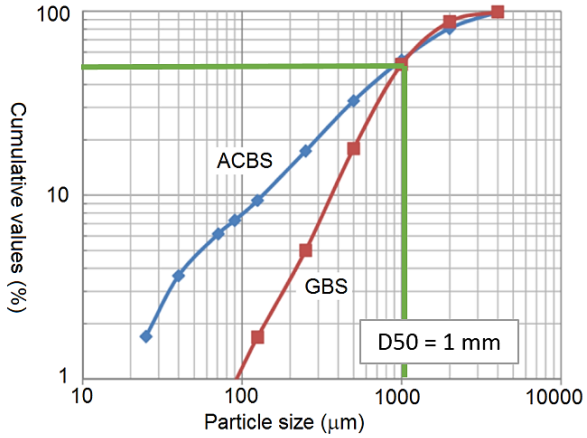

Figure 41: Particle size distribution of the as-received GBS and ACBS [103].

4.1.2 Milled BFS

4.1.2.1 Chemical composition

The elemental composition of BFS types was conducted by means of EDX analyses, where the elemental peaks for both types are shown in Figure 42. The spectra of individual elements for ACBS and GBS are indicated in Figure 43 and Figure 44. The spectra reflect that both GBS and ACBS were composed of the same major elements such as calcium, aluminum, silicon and magnesium. This indicates that the variation of the cooling rates for GBS and ACBS types hardly affected their elemental composition.

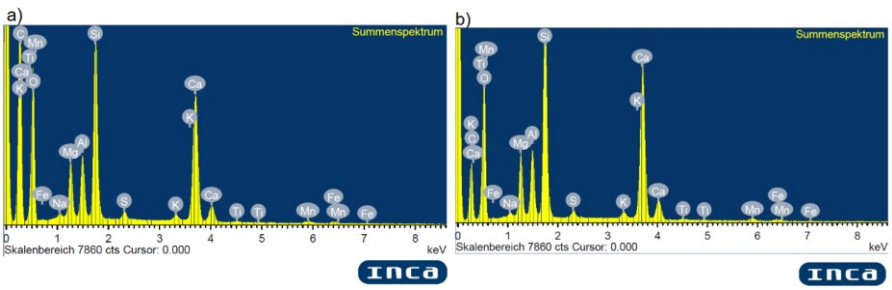

Figure 42: EDX peaks for (a) ACBS and (b) GBS.

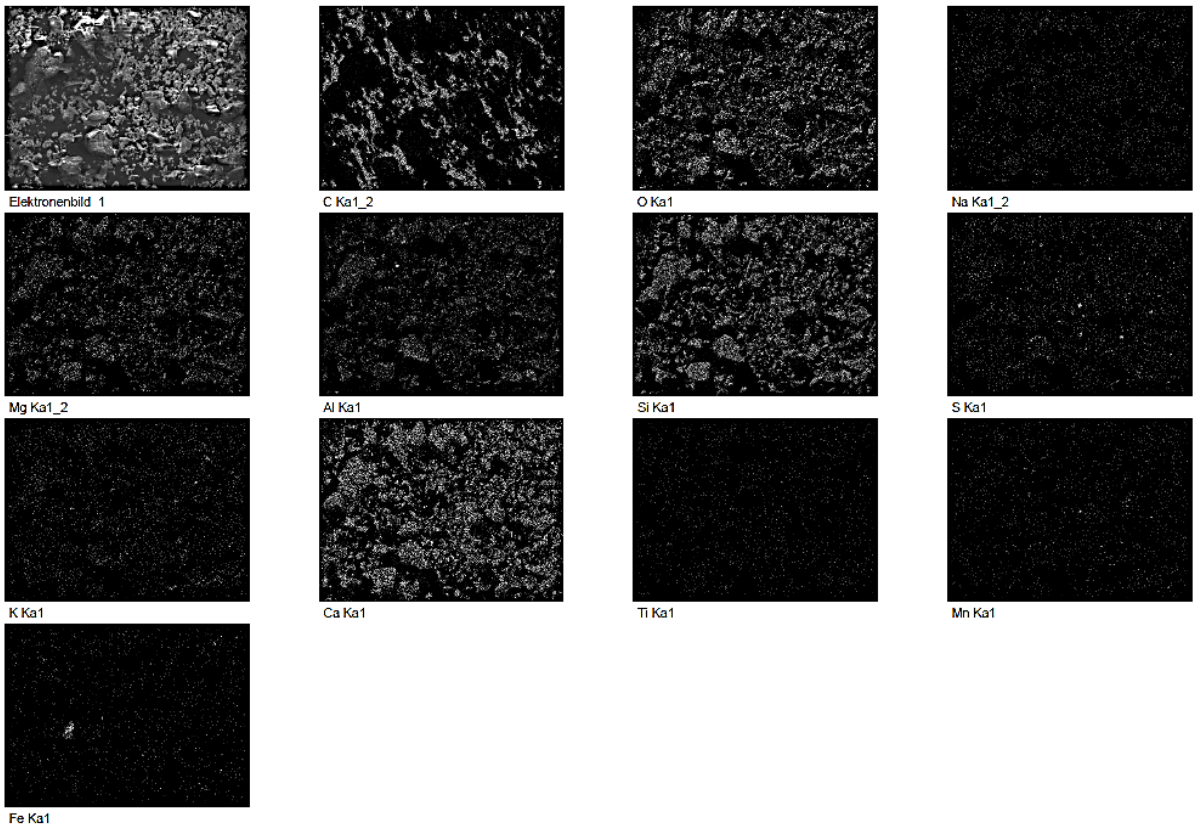

Figure 43: EDX spectra for elements composing ACBS.

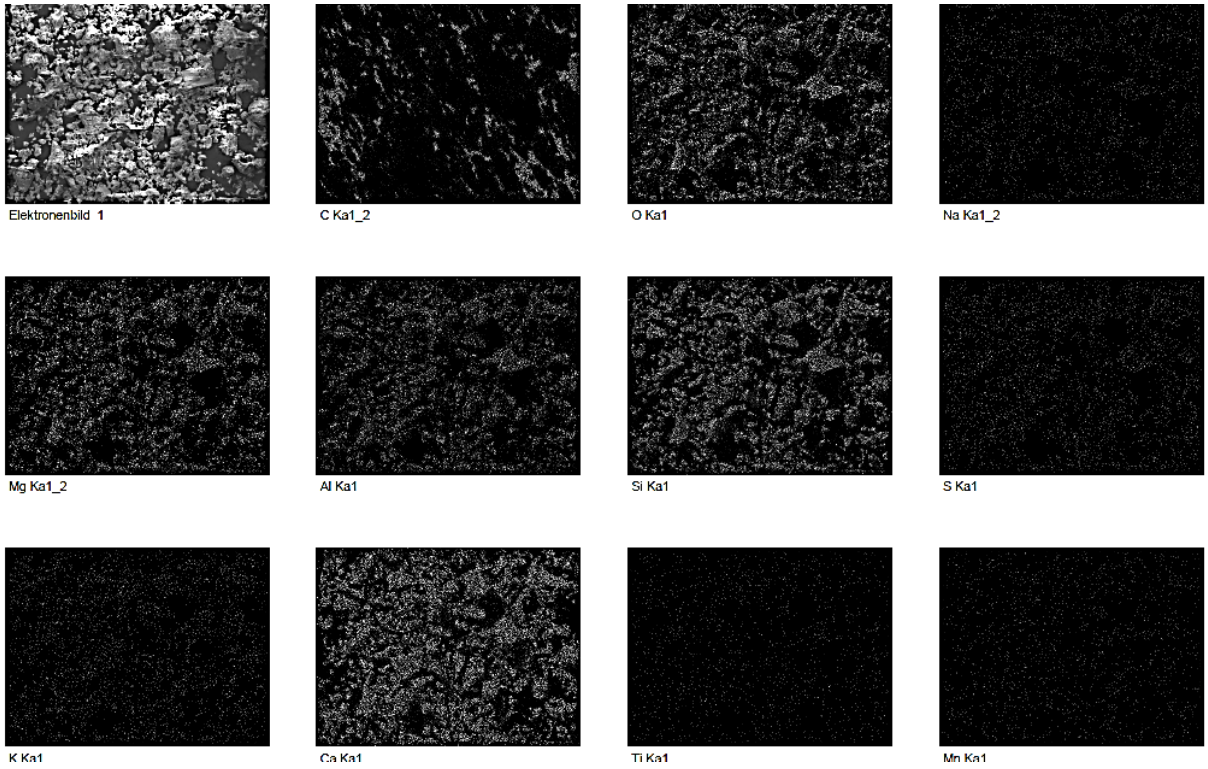

Figure 44: EDX spectra for elements composing GBS.

As previously discussed, ACBS has a crystalline structure while GBS is amorphous. This structural disparity resulted from the variation of cooling rates. It is also shown that the most intensive elemental spectra are the ones corresponding to the following elements: Magnesium, silicon, calcium and aluminum, oxygen. These spectra correspond to the major oxides of BFS: Calcium oxide (CaO), magnesium oxide (MgO), silicon oxide (SiO_2) and aluminum oxide (Al_2O_3).

4.1.2.2 BFS size, distribution and morphology

As shown in Figure 45, the median D50 particle sizes were identified from the graphs, which correspond to the cumulative value of 50 %. In Table 26, the corresponding D50 values for the different particle size distributions are listed. In order to investigate the BFS particle morphology, low- and high-magnification SEM micrographs were captured, as shown in Figure 46, where the slag particles showed irregular, non-equiaxed and sharp-edged morphology.

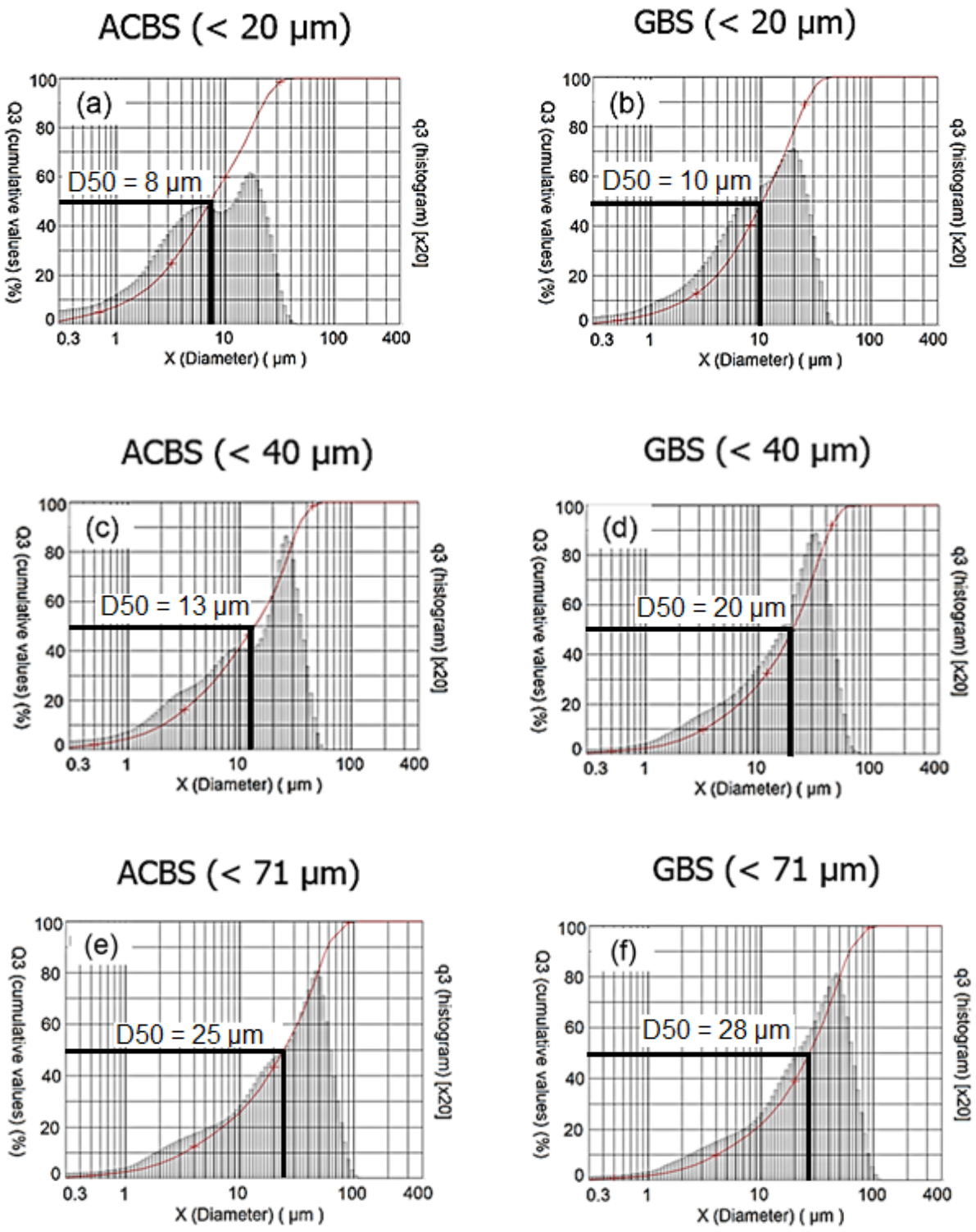

Figure 45: Cumulative particle size distribution with identified D50.

Table 26: D50 value for each particle size distribution.

Letter	Particle size distribution	D50 (µm)
a	ACBS (< 20 µm)	8
c	ACBS (< 40 µm)	15
e	ACBS (< 71 µm)	25
b	GBS (< 20 µm)	10
d	GBS (< 40 µm)	20
f	GBS (< 71 µm)	28

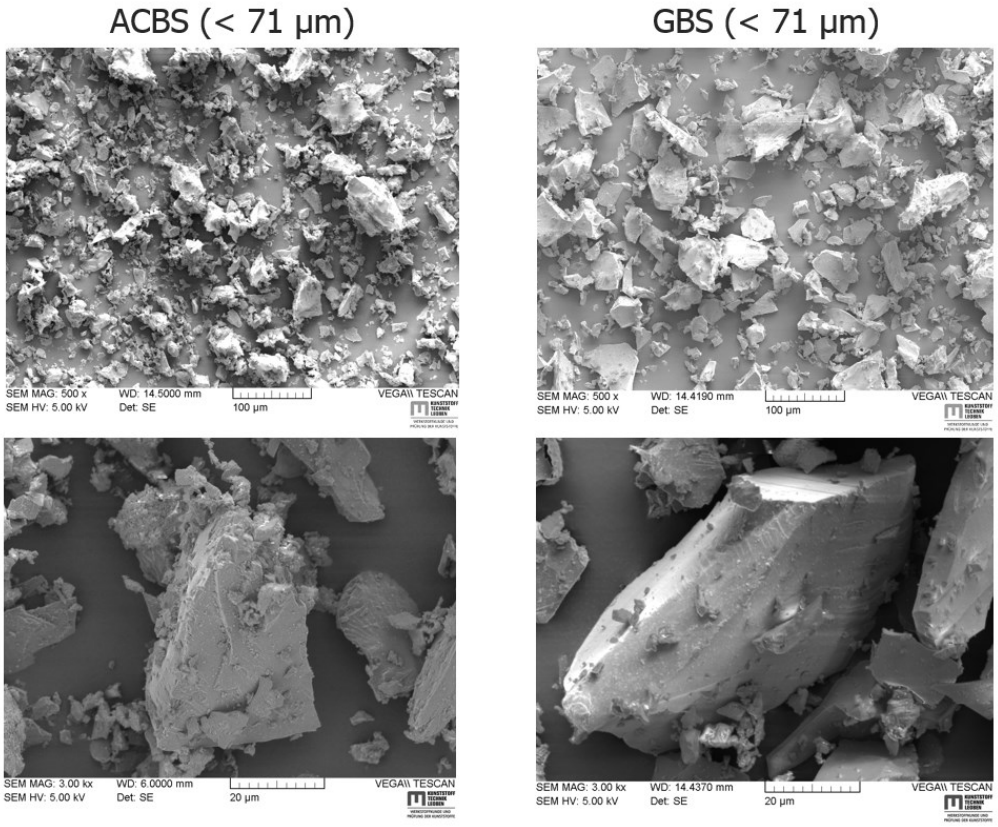

Figure 46: Low- and high magnification SEM micrographs of ACBS and GBS fillers.

4.2 Findings of the basic study

4.2.1 Experiment 1: Influence of unmodified-BFS parameters

The goal of this experiment was to study the influence of three BFS filler parameters, loading, distribution and type upon the rheological, thermal and mechanical properties of PP. The findings of this experiment also helped to identify which parameter(s) having significant influence upon the properties of PP. Upon analyzing the finding tables, the dimensional relationships between the significant parameters where plotted for better analyses.

In addition, a short statistical analyses were performed using JMP® software package to help identifying the significant factors influencing the tensile stiffness, ultimate strength and strain at break responses of the compounds. The optimum compound formulations with respect to the maximum three responses was suggested by the model 'prediction profiler' via the 'steepest ascent' optimization technique. The statistical analyses were compiled in a report [66] and can be found in the appendix section.

4.2.1.1 Rheological behavior

The values of the three rheological parameters, storage and loss moduli (G´ and G´´) as well as the complex shear viscosity (η^*), of the compounds as compared to the neat PP are listed in Table 27. The rheological data were classified intro three groups based on the distribution of the utilized BFS filler. The included data were all at the shear rate of 0.1 1/s. With some exceptions, the table shows that the η^*, G´ and G´´ values of the compounds were mostly 2 – 35, 5 – 40 and 4 – 35 % higher than the neat PP. The compound recording the highest G´ and G´´ values was '30G71', while the one recording the highest η^* was '30G40', with nearly 35 % increase over the neat PP value . In addition, the table shows that the highest η^*, G´ and G´´ levels corresponded to the <40 µm group. It was also noticed that for some compound, the rheological data were 5 – 10 % lower than the neat PP.

Figure 47 and Figure 48 show that all the compounds exhibited a shear-thinning behavior, where the rheological parameters decreased with increasing the shear rate. The influence of the BFS loading on the η^* is illustrated in the graphs of Figure 49 to Figure 51. The three graphs shared a common trend, where the increase in η^* was proportional to the BFS loading. The proportionality between the η^* and its rigid filler loading have been widely reported in literature [51, 92–98]. It might be also instructive to particularly refer to the reporting of Jahani [97], where the rheological properties increased proportionally with a comparable mineral filler, talc, in PP. Such increase is believed to be due to the restriction of chain mobility by the filler [99]. Compared to the neat PP, the figures display that the increase in η^* with BFS loading was almost linear. Furthermore, it was generally noticed that the η^* levels of GBS and ACBS were comparable to each other, regardless of the loading or distribution setting.

Table 27: Shear rheology findings of experiment 1 (at 200 °C and 0.1 1/s).

Code	Storage modulus (Pa)	±D	Loss modulus (Pa)	±D	Complex shear viscosity (Pa.s)	±D
Neat PP	459	18	1884	69	19390	351
10A71	604	17	2303	41	19730	170
10G71	490	10	2014	86	20725	643
20A71	512	12	2102	59	21630	424
20G71	528	10	2163	69	22265	502
30A71	576	20	2362	96	24310	806
30G71	571	16	2343	48	24110	198
10A40	530	18	2126	96	21910	332
10G40	534	10	2136	55	22010	417
20A40	563	16	2245	87	23140	805
20G40	592	14	2361	50	24340	80
30A40	635	18	2509	60	25890	219
30G40	639	15	2545	93	26240	537
10A20	450	10	1812	99	18670	216
10G20	458	16	1841	92	18970	235
20A20	494	18	1977	75	20380	339
20G20	477	12	1913	90	19720	424
30A20	518	17	2064	80	21280	358
30G20	517	14	2067	55	21300	244

The graphs showing the influence of the BFS size and distribution on the η^* are illustrated in Figure 52 to Figure 54. It was observed that the <20 µm distribution tended record lower η^* levels compared to the other distributions. The ACBS and GBS compound levels were comparable except for the 10 wt.-% loading group, where a clear difference between the <20 µm GBS and ACBS levels was noticed. That is, the GBS recorded a decrease of almost 10 % compared to its ACBS counterpart.

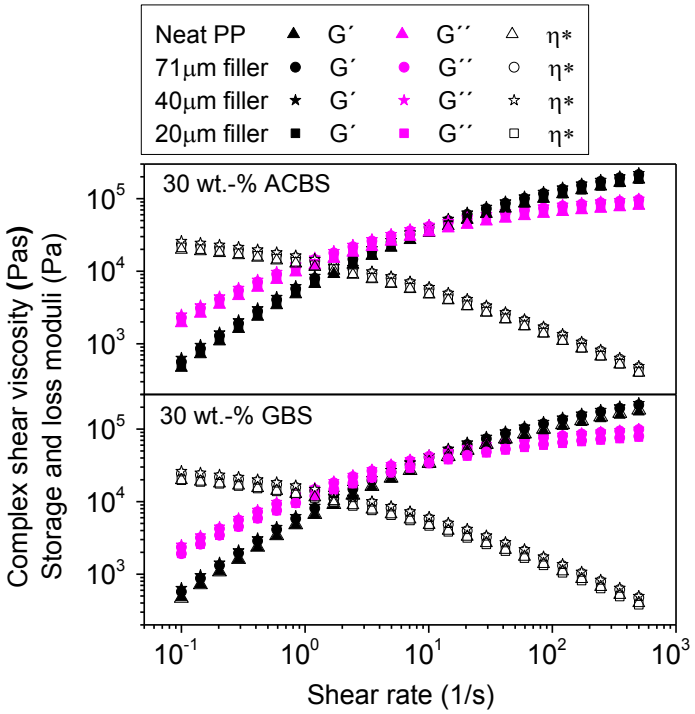

Figure 47: G´, G´´ and η as function of shear rate at 30 wt.-% loading*

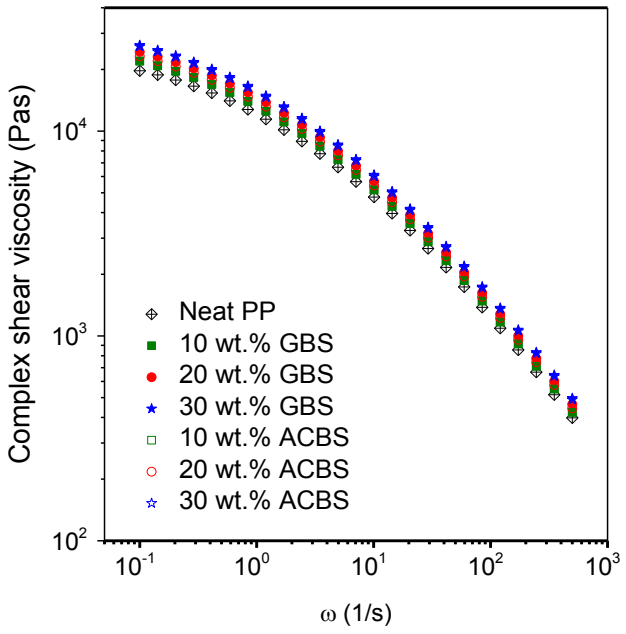

Figure 48: Complex shear viscosity at <40 µm.

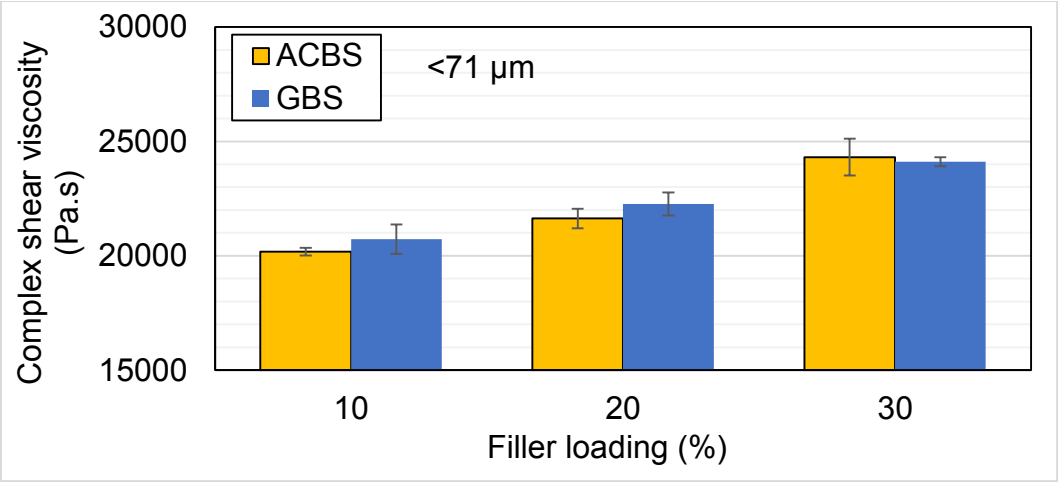

Figure 49: Complex shear viscosity at <71 µm distribution.

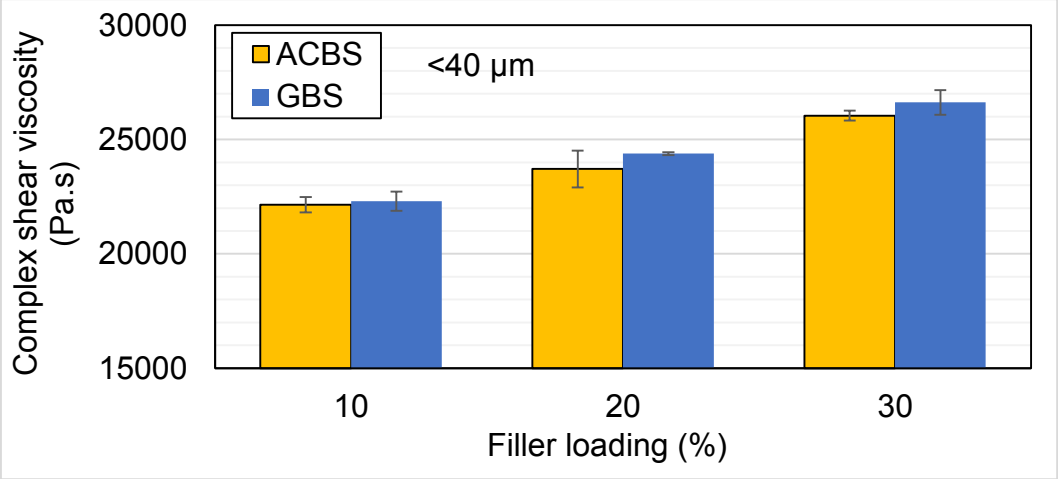

Figure 50: Complex shear viscosity at <40 µm distribution.

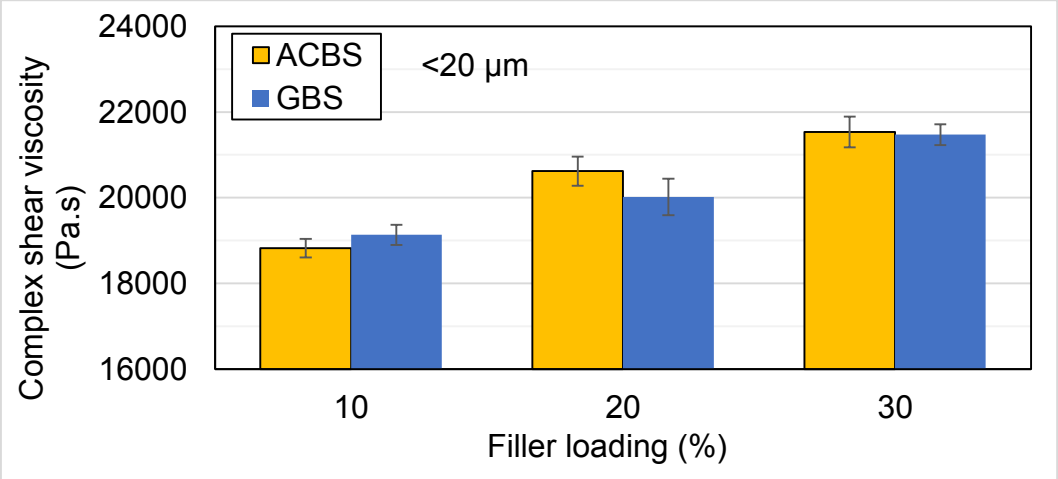

Figure 51: Complex shear viscosity at <20 µm distribution.

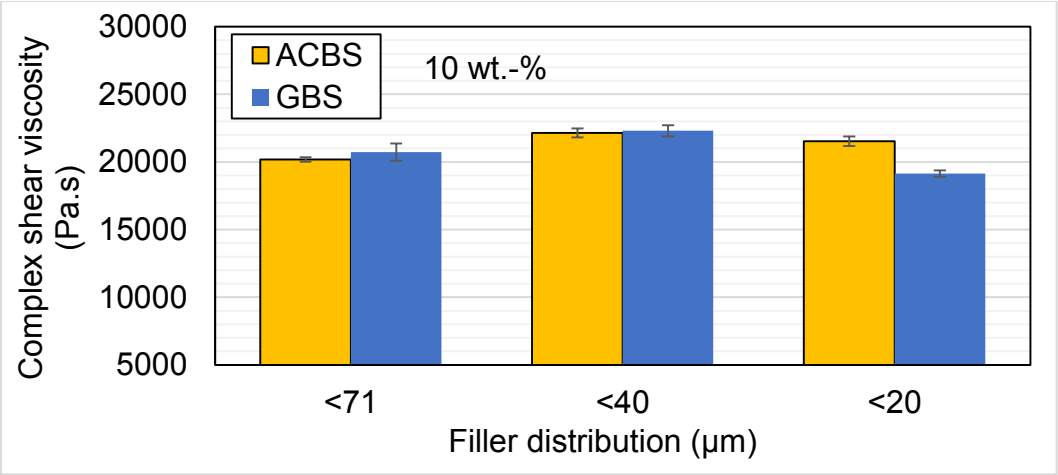

Figure 52: Complex shear viscosity at 10 wt.-% loading.

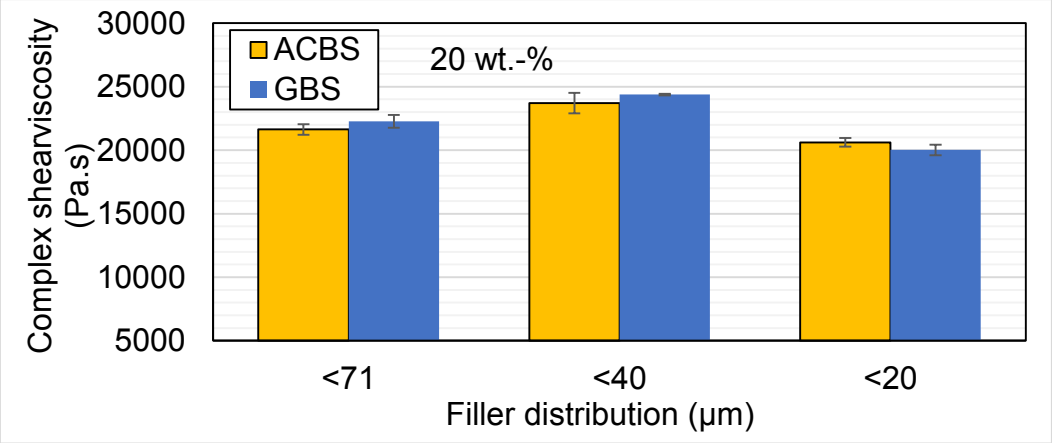

Figure 53: Complex shear viscosity at 20 wt.-% loading.

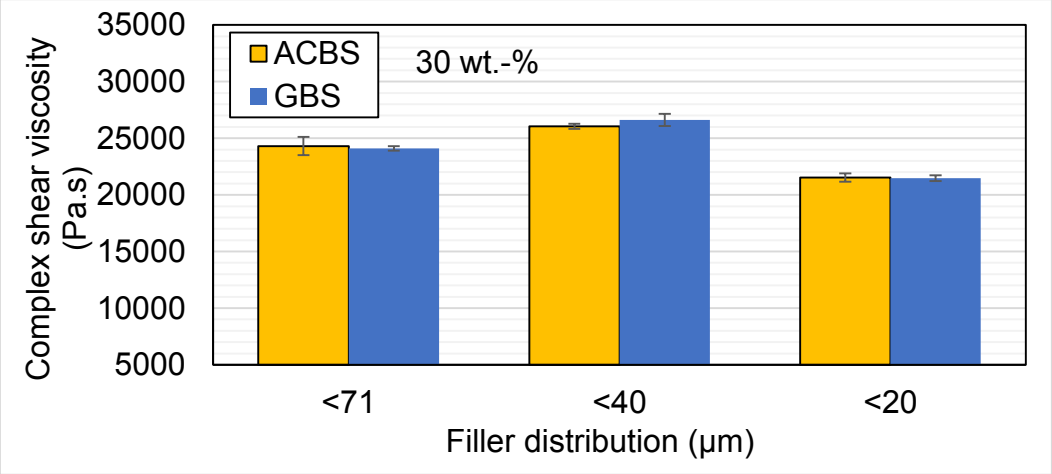

Figure 54: Complex shear viscosity at 30 wt.-% loading.

The investigation of cross over points is useful for understanding the influence of filler type and loading on the viscoelastic properties of the compounds, as the cross over point emphasizes the transition from viscous to elastic behavior. In Figure 55 and Figure 56, the cross over frequency and modulus components were plotted as a function of GBS and ACBS loading.

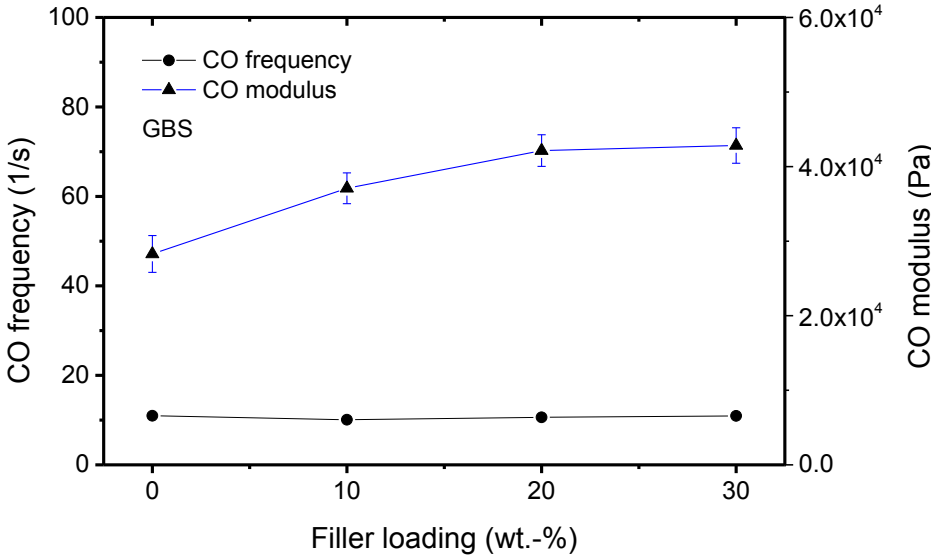

Figure 55: Cross over (CO) frequencies and moduli at for < 40 µm-GBS loading.

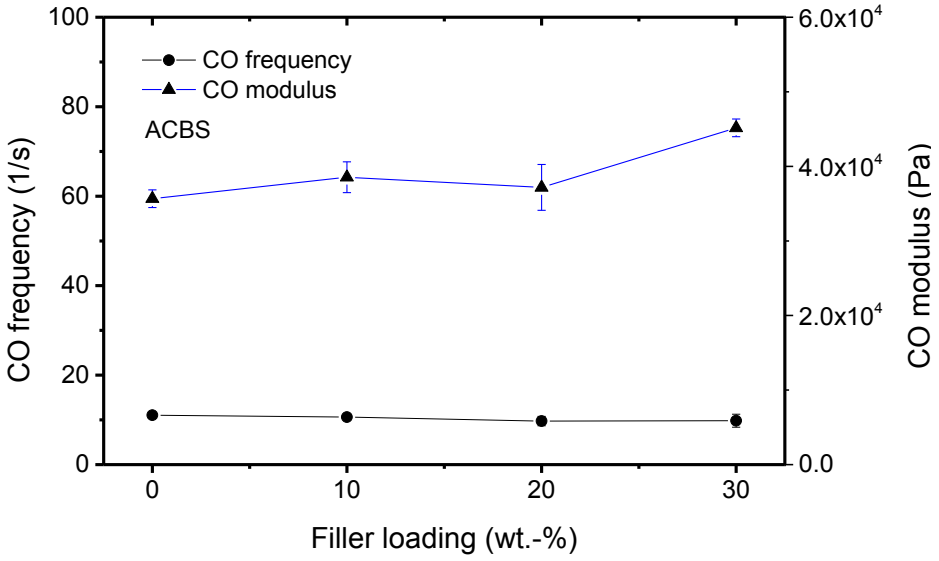

Figure 56: Cross over (CO) frequencies and moduli at for < 40 µm-ACBS loading.

The cross over frequencies were almost unchanged for filler loadings up to 30 wt.-%. The stability of cross over frequency reflects that the molecular mobility and relaxation time behavior of PP is almost unchanged at the indicated filler loading. Cross over moduli increased almost linearly with the BFS loading. A deviation was observed in the compound '20A40', possibly due to an experimental error. The linear increase of the cross over modulus with the filler loading is possibly due to a corresponding increase of the molecular weight distribution, elasticity and solid-like behavior of the melt [36].

4.2.1.2 Thermal behavior

The data presented in Table 28 show that BFS hardly influenced T_c or T_m of the compounds. The change in crystallization- (ΔHc) or melting (ΔHm) enthalpy, on the other hand, was influenced by the addition of BFS. That is, ΔHc and ΔHm decreased by at least 5 – 20 % when comparing the neat PP with the BFS filled compounds, meaning that less amount of energy was needed to induce crystallization or melting in the filled compounds as compared to the neat PP. It was noted that the error margin for the ΔH for neat PP and some compound values was quite large, possibly due to experimental error.

Figure 57 demonstrates the second-cycle heating curves of BFS-filled PP compounds at 10 – 30 % loading and <40 µm distribution. It was found that introducing the BFS filler narrowed down the melting peaks as compared to the neat PP, which corresponded to a decreased melting enthalpy of the compounds, while no shifting of the peaks was witnessed among the compounds.

Figure 58 - Figure 60 show that the compounds' DOC decreased up to 40 % as compared to the neat PP. It is likely that the BFS particles were able to disrupt the crystalline regions of the PP and hence decreasing its DOC. It was hence expected to see the DOC decrease almost linearly with increasing the BFS loading. A similar trend was reported by Pustak et al. [83], where the DOC of micron-sized silica filled PP compounds decreased almost linearly as the silica loading increased. Compared to the neat PP, a decrease of almost 30 % for the <71 µm group was noticed, while a decrease for almost 10 % was observed for the other two. It is suggested that the <71 µm BFS distribution affected the DOC more dramatically compared to the other

two. That was expected, since the coarse BFS particles of the <71 µm distribution were capable of inducing more deformation, and hence disturbance of the crystalline regions, into the molecular structure of PP as compared to the finer particles of <40 and <20 µm distributions. The DOC for the GBS and ACBS compounds were generally comparable except for the following compounds: '20A/G71' (20A71 was 5 % less than 20G71), '10A/G20' (10G20 was 10 % less than 10A20) and '30A/G20' (30G20 was 5 % higher than 30A20).

Figure 61 - Figure 63 show the influence of BFS distribution within each loading group. For the 30 wt.-% group, Figure 63, the DOC was observed to increase almost linearly with distribution for GBS compounds. For the other two loading groups, this pattern was not clear. In the 10 and 30 wt.-% groups, an almost 10 % difference in the DOC was recorded between the <20 µm GBS and -ACBS compounds. This came in an alternating manner, where the ACBS level was higher at the 10 wt.-% group and lower at the 30 wt.-% one. It was difficult to find an interpretation for this phenomenon, but it likely to be linked with the difference in distribution between each BFS type. Accordingly, a careful inspection of the BFS particle distribution in both Figure 45 and Figure 46 could be insightful. For Figure 45 (a, b) it was observed from the histograms' areas that GBS consisted of relatively more coarse particles, i.e. 5 – 20 µm, and consequently less finer particles, i.e. 0.3 - 5 µm, compared to ACBS. This classification was indicated graphically but for the <71 µm group in Figure 46. Depending on the loading, it might be possible that either one of the fine or coarse particle groups, 0.3 – 5 or 5 – 20 µm showed more impact upon the DOC over the other. For the 10 wt.-% loading, the higher amount of coarse particles in GBS compounds could be dominating, thus triggering more deformation within the PP structure. This might be a reason why the DOC of the GBS filled compound was lower than that of corresponding ACBS one. On the other hand, at 30 wt.-% loading higher amount of the relatively fine particles in ACBS compounds likely dominated and triggered the deforming action compared to GBS compounds, resulting in lower DOC for the ACBS filled compound.

Table 28: Thermal findings of experiment 1.

Code	T_c (°C)		ΔH_c (J/g)		T_m (°C) second heating		ΔH_m (J/g) second heating		DOC (%)	
Neat PP	118.9	±0.56	91.6	±13.40	167.6	±0.69	92.5	±11.18	44.7	±0.69
10A71	118.9	±0.23	74.4	±1.55	167.3	±0.23	75.5	±1.61	36.2	±0.23
10G71	119.2	±0.07	78.6	±2.16	167.2	±0.09	77.4	±2.82	37.0	±0.09
20A71	118.8	±0.16	67.4	±5.20	167.0	±0.13	67.9	±5.60	32.6	±0.13
20G71	119.1	±0.35	73.9	±8.08	167.5	±0.58	73.6	±7.40	35.2	±0.58
30A71	118.9	±0.12	63.4	±1.93	166.7	±0.11	63.3	±0.81	30.3	±0.11
30G71	120.3	±0.21	60.9	±1.32	167.0	±0.21	62.0	±1.07	29.3	±0.21
10A40	116.9	±0.74	82.2	±1.39	168.7	±1.07	82.3	±2.47	39.4	±1.07
10G40	118.4	±0.23	79.5	±0.42	168.1	±0.47	79.8	±1.13	37.9	±0.47
20A40	118.3	±0.39	68.5	±5.03	167.7	±0.37	70.4	±3.90	33.2	±0.37
20G40	118.0	±0.06	71.9	±8.75	168.5	±0.16	72.2	±8.37	34.2	±0.16
30A40	119.0	±0.50	70.4	±0.63	167.4	±0.59	67.8	±2.40	33.5	±0.59
30G40	118.1	±0.30	72.8	±7.62	168.2	±0.40	72.6	±7.15	34.8	±0.40
10A20	118.6	±0.42	85.9	±6.56	168.1	±0.67	86.4	±5.69	41.2	±0.67
10G20	118.4	±0.01	76.0	±5.44	168.4	±0.12	76.3	±5.11	36.1	±0.12
20A20	118.6	±0.62	76.5	±14.30	168.2	±0.77	79.9	±10.20	37.9	±0.77
20G20	118.2	±0.01	76.0	±5.10	168.5	±0.11	78.2	±7.67	36.7	±0.11
30A20	119.7	±0.23	71.5	±1.20	167.4	±0.35	71.1	±1.68	33.2	±0.35
30G20	118.8	±0.14	74.7	±0.13	167.9	±0.36	74.4	±0.47	35.3	±0.36

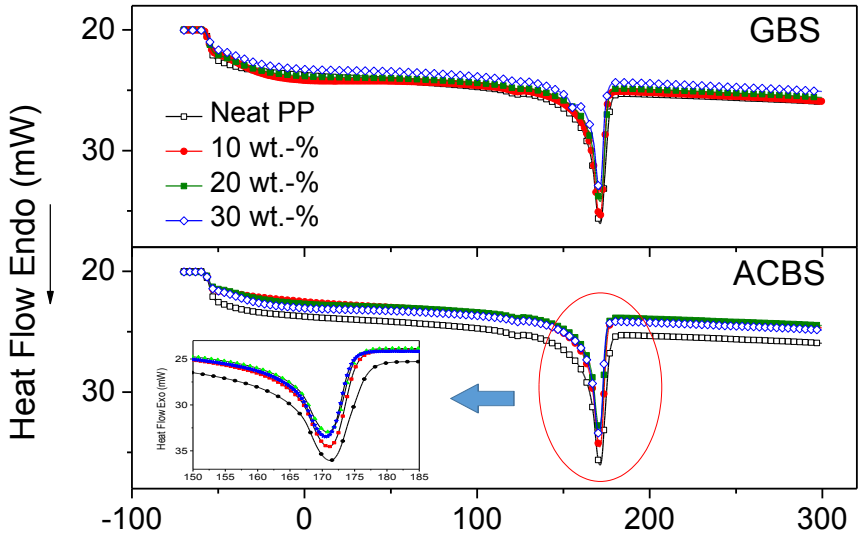

Figure 57: DSC heating curves for neat PP and <40 µm-BFS compounds.

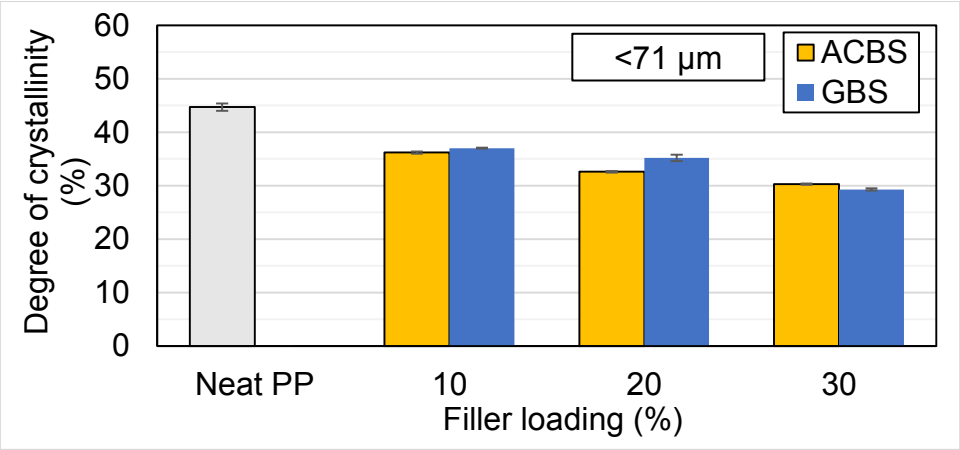

Figure 58: DOC at different <71 µm-BFS loadings.

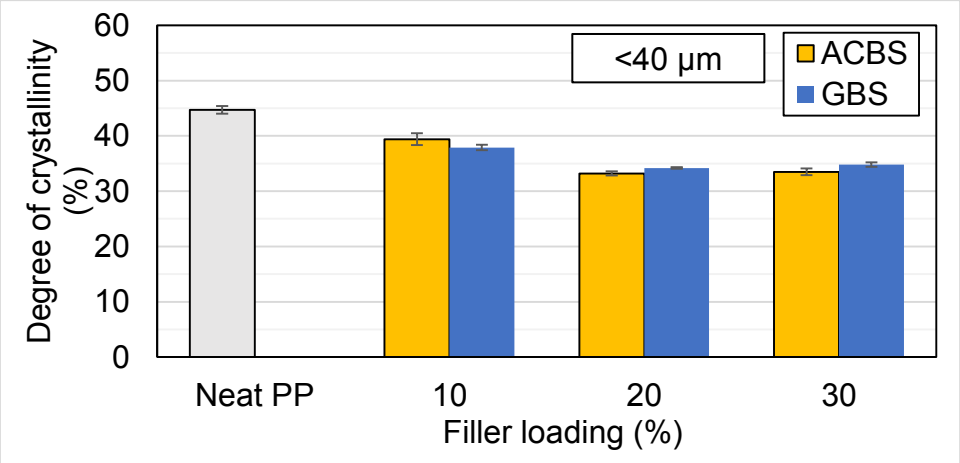

Figure 59: DOC at different <40 µm-BFS loadings.

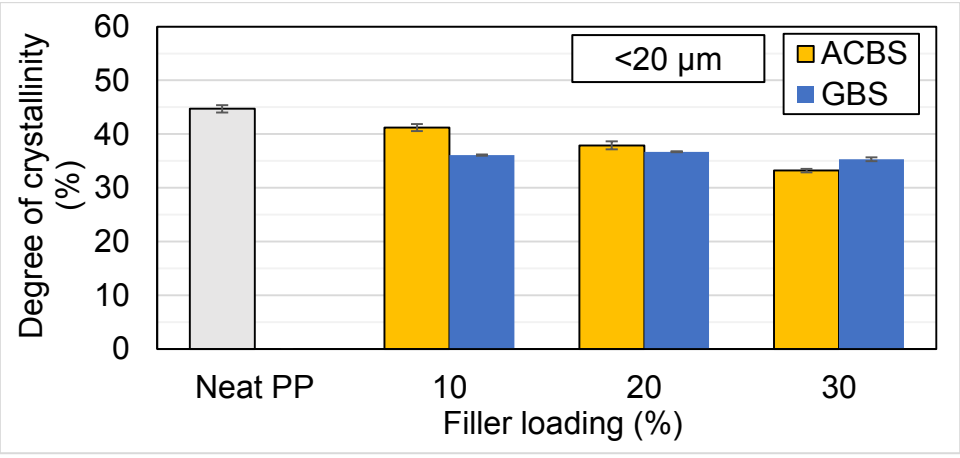

Figure 60: DOC at different <20 µm-BFS loadings.

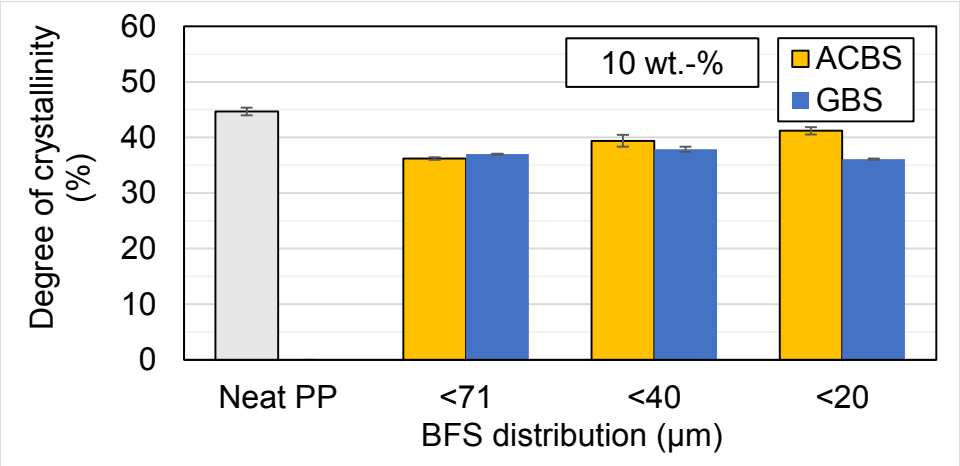

Figure 61: DOC at different 10 wt.-%-BFS distributions.

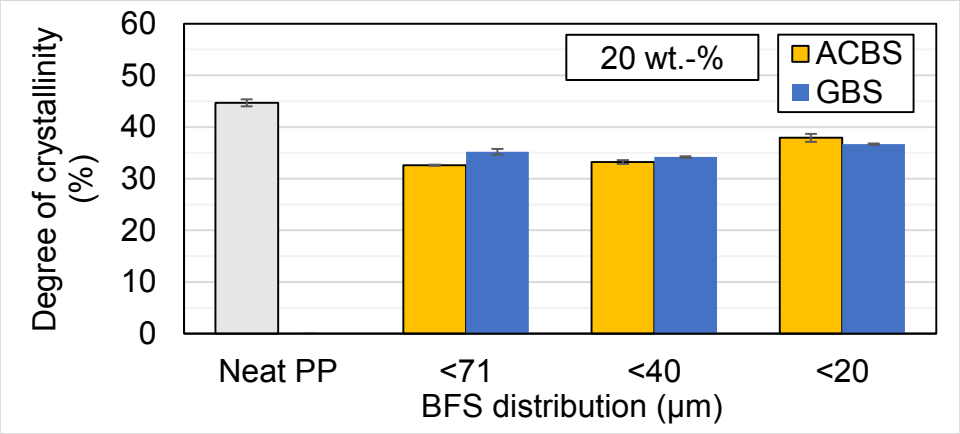

Figure 62: DOC at different 20 wt.-%-BFS distributions.

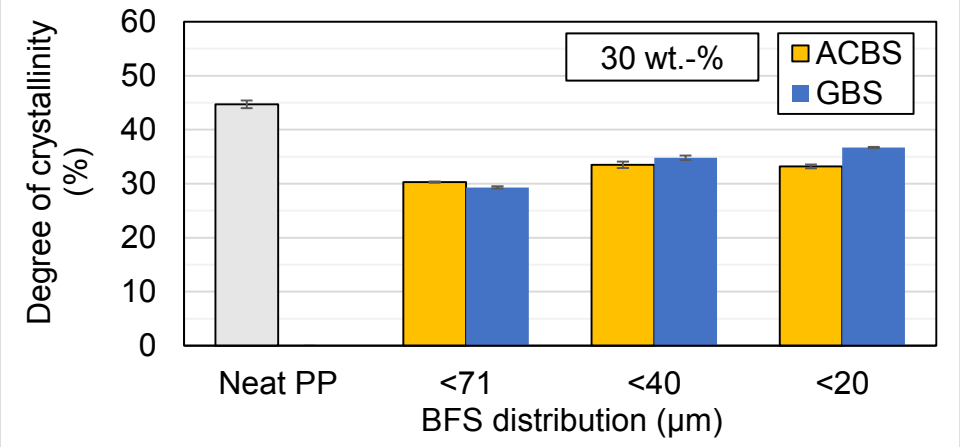

Figure 63: DOC at different 30 wt.-%-BFS distributions.

Figure 64 and Figure 65 demonstrate the thermal conductivity levels for the '20A/G20' and '20A/G71' compounds. The selection of the compounds for thermal conductivity testing was based upon the significance of the 20 wt.-% loading as well as consideration of the lower- and upper distribution levels of BFS. Compared to the neat PP, the BFS filler increased the thermal conductivity by almost 40 %. For the neat PP, the thermal conductivity levels increased linearly with the testing temperature, with an overall increase of nearly 10 % from 25 to 100 °C. In contrast, the thermal conductivity values of the filled compounds were almost stable at the three test temperatures.

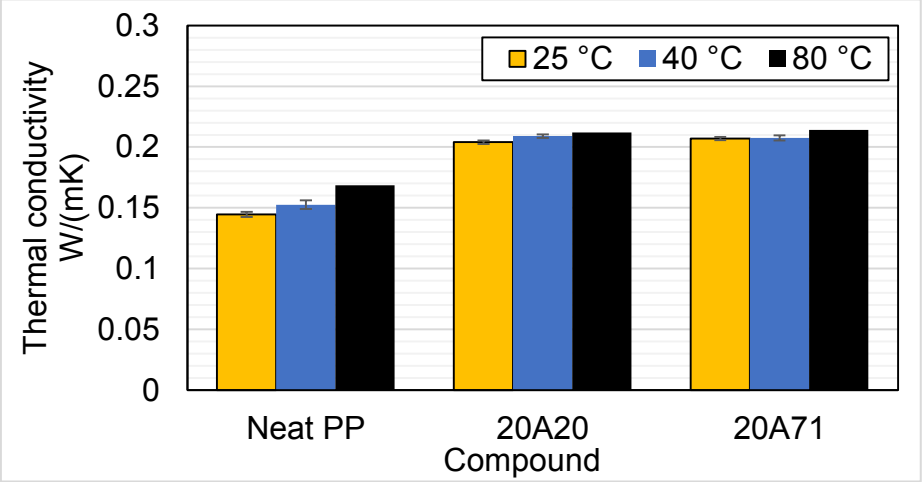

Figure 64: Thermal conductivity values of selected ACBS filled compounds.

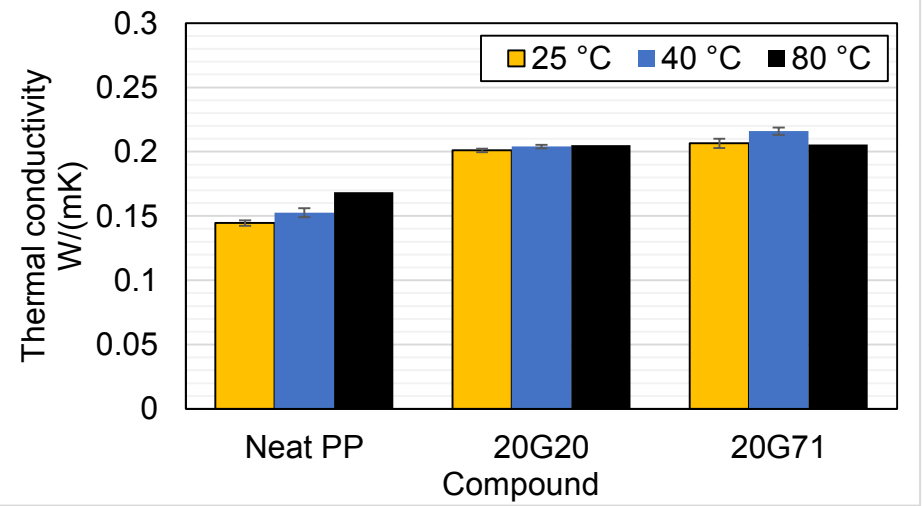

Figure 65: Thermal conductivity values of selected GBS filled compounds.

4.2.1.3 Mechanical behavior

Table 29 shows the mechanical properties of the filled compounds as compared to the neat PP. Selectively, the stress-strain diagram was plotted for <71μm-BFS-filled compounds in Figure 66. During testing, it was observed that all compounds fracture in a ductile manner. Figure 66 shows that increasing the BFS loading notably decreased the compound ductility. At 30 wt.-% loading, the compound strain was almost 70 % lower that the neat PP.

Table 29: Mechanical findings of experiment 1.

Code	Young's modulus (MPa)	±D	Ultimate strength (MPa)	±D	Ultimate strain (%)	±D	Strength at break (MPa)	±D	Strain at break (%)	±D
Neat PP	1504	6	24.2	0.4	4.6	0.1	17.3	0.2	116	24
10A71	1606	97	23.6	0.7	4.1	0.0	17.3	0.4	67	22
10G71	1601	51	24.4	0.7	4.5	0.0	17.5	0.1	100	5
20A71	1794	94	21.8	0.1	3.9	0.2	17.3	0.4	60	8
20G71	1742	26	20.3	0.0	3.9	0.0	16.7	0.4	69	1
30A71	1893	18	20.9	0.5	3.8	0.1	18.3	0.0	43	6
30G71	1779	9	19.4	0.1	3.9	0.1	16.9	0.1	37	3
10A40	1426	49	23.0	0.3	4.5	0.1	16.4	0.7	71	15
10G40	1479	41	22.4	0.6	4.3	0.1	17.1	1.3	72	24
20A40	1671	38	22.0	0.7	3.7	0.0	16.4	1.3	59	26
20G40	1684	48	20.6	0.1	3.9	0.1	16.1	0.4	60	9
30A40	1810	44	20.9	0.8	3.7	0.2	17.1	0.8	47	6
30G40	1818	2	19.9	0.5	3.9	0.1	16.3	0.7	50	10
10A20	1535	60	20.9	0.4	4.5	0.1	17.2	1.8	193	139
10G20	1390	137	20.2	0.5	4.6	0.1	16.8	0.2	122	85
20A20	1678	33	21.9	0.2	4.1	0.2	17.3	0.4	75	53
20G20	1666	54	34.4	0.6	4.0	0.2	17.0	1.0	124	67
30A20	1824	72	33.6	0.6	3.6	0.0	16.8	0.6	89	8
30G20	1801	19	32.1	0.9	3.8	0.1	16.0	1.4	127	71

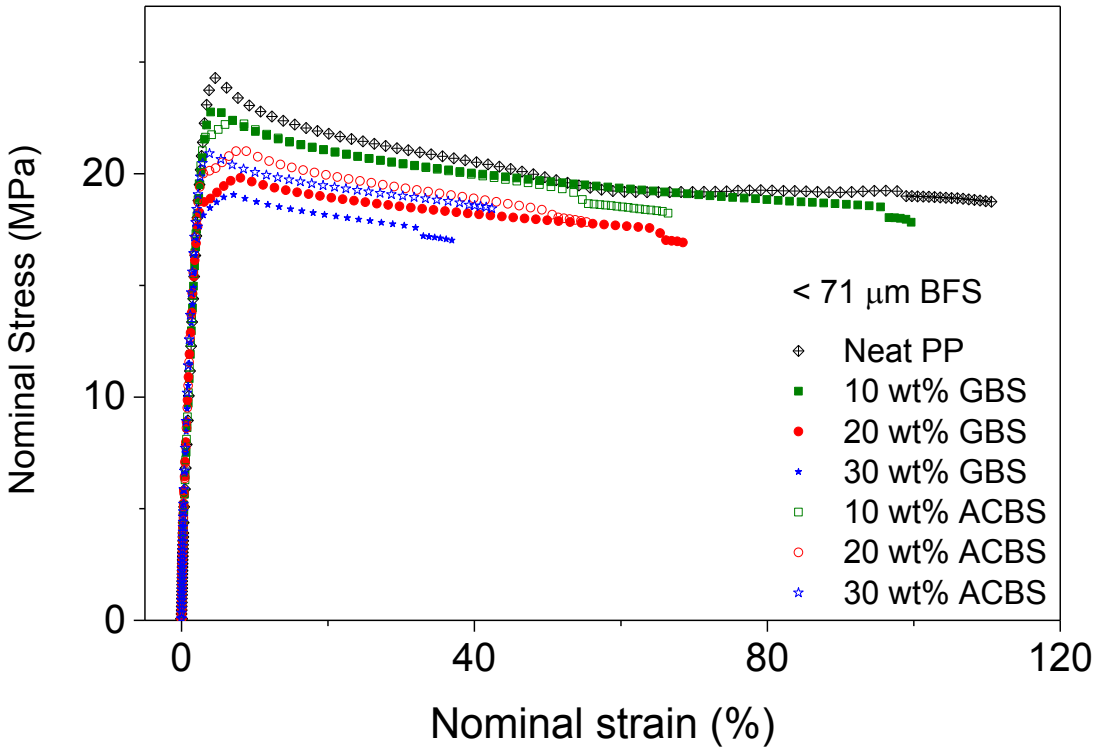

Figure 66: Nominal stress-strain curves of <71μm-BFS filled PP compounds.

Figure 67 - Figure 69 show the influence of the BFS loading upon the tensile stiffness of the compounds. Similar to the η* pattern, increasing the BFS loading was coupled with an increasing trend in the tensile stiffness up to 20 % compared to the neat PP. It was also observed that the variation of the slag type hardly influenced the tensile stiffness. The increase in the tensile stiffness with increasing the coarse rigid filler loading agrees with the reporting of Nurdina et al. [68], Lou et al. [52] and Selvin et al. [86] that relatively coarse rigid fillers, i.e. micron-sized mineral fillers, increase the stiffness of the base polymer; such increase is often coupled with a decrease in polymer ductility.

Figure 70 - Figure 72 demonstrate the influence of the BFS distribution upon the tensile stiffness of the compounds. Unlike the influence of varying the BFS loading, the variation of BFS distribution did not show any specific trend. At 30 wt.-% loading, the <71 µm ACBS showed nearly 10% higher stiffness compared to the GBS compound.

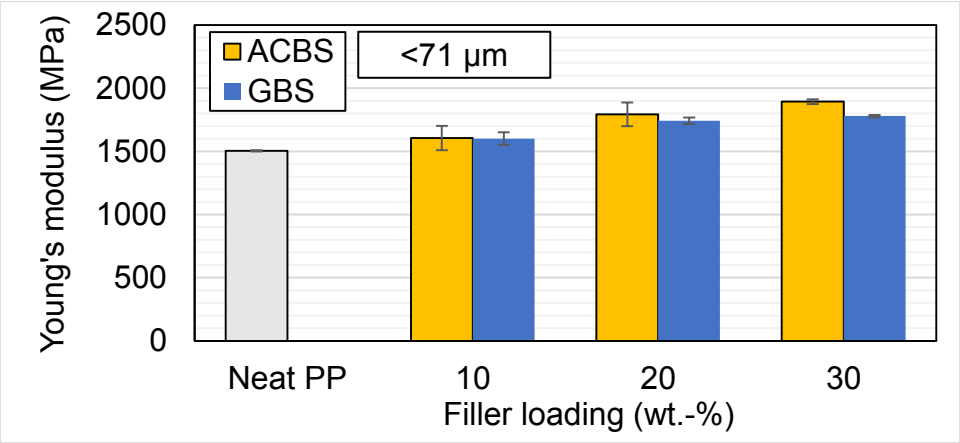

Figure 67: Young's modulus at different <71 µm-BFS loadings.

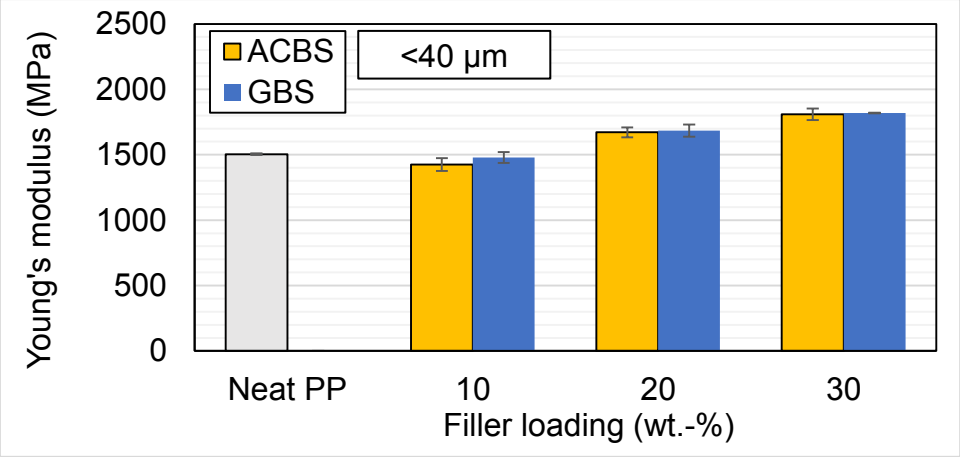

Figure 68: Young's modulus at different <40 µm-BFS loadings.

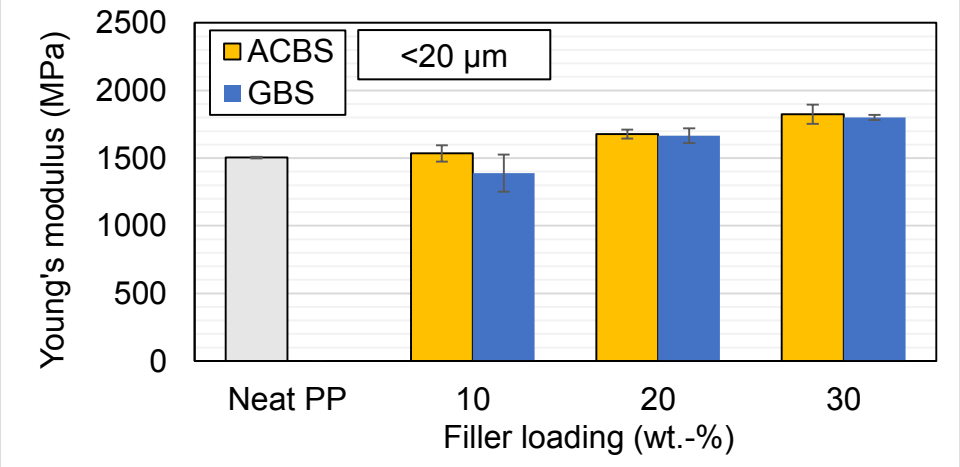

Figure 69: Young's modulus at different <20 µm-BFS loadings.

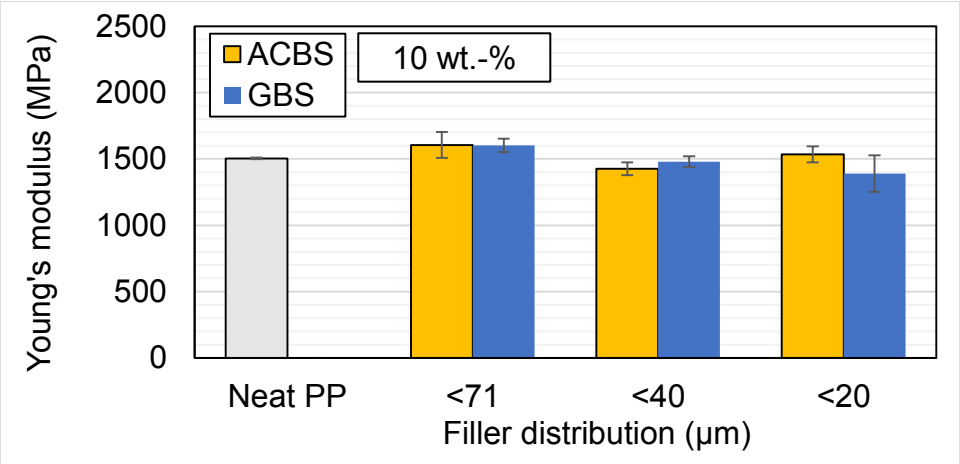

Figure 70: Young's modulus at different 10 wt.-%-BFS distributions.

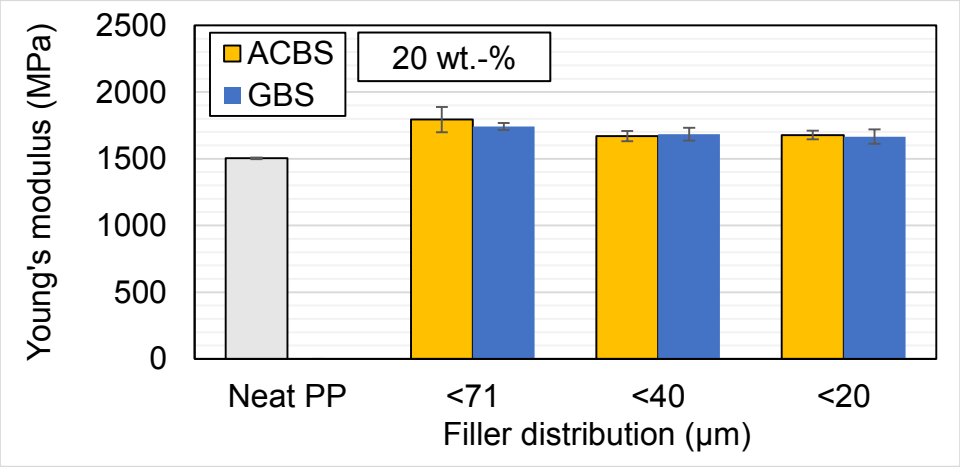

Figure 71: Young's modulus at different 20 wt.-%-BFS distributions.

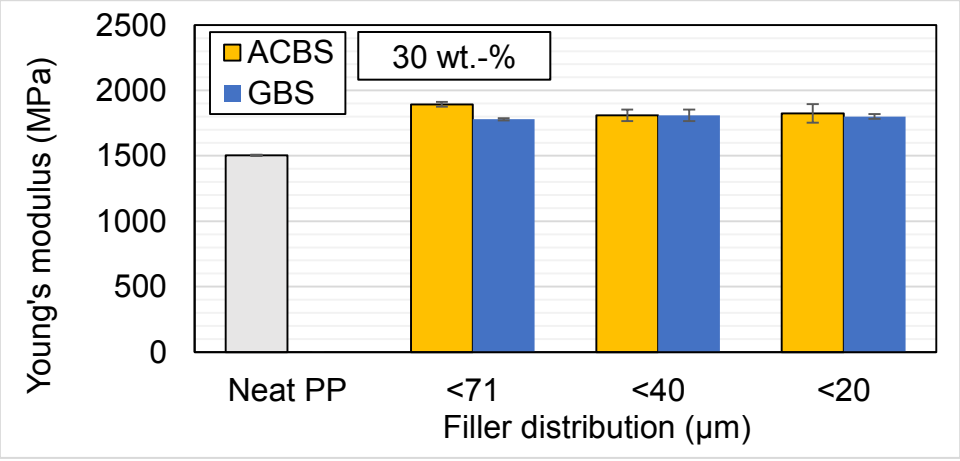

Figure 72: Young's modulus at different 30 wt.-%-BFS distributions.

Figure 73 - Figure 75 show the influence of BFS loading on the ultimate strength. For the <71 and <40 µm distributions, the ultimate strength of the compounds were observed to decrease linearly with increasing BFS loading. At the <20 µm distribution, this trend disappeared. In this particular distribution, the ultimate strength of both ACBS and GBS compounds was reduced by almost 50 % at the 10 wt.-% loading. At the 20 wt.-% loading, however, only the ultimate strength of the ACBS compound was reduced.

To investigate the influence of BFS distribution on the ultimate strength, the plots of Figure 76 - Figure 78 were constructed. At the 10 wt.-% loading, the ultimate strength generally experienced a decreasing pattern. However, this trend did not exist at the 20 and 30 wt.-% loadings. Rather, a stabilization of the ultimate strength was observed at the <71 µm and <40 µm followed by an almost 50 % increase for either GBS or both ACBS/GBS filled compounds at the <20 µm.

Figure 79 - Figure 81 demonstrate the influence of the filler loading on the strain at break levels at each distribution. Similar to the ultimate strength at 10 wt.-%, the ductility of the compounds seemed to undergo a decreasing pattern with increasing the filler loading only at the <71 and <40 µm distributions. The trend did not hold at the <20 µm distribution, where comparable ductility levels with a high margin of error dominated the scene. Inspecting the influence of the BFS distribution, Figure 82 - Figure 84, revealed that only at <20 µm the strain at break was comparable to the neat PP, but again with large margins of error resulting from premature failure.

The optical micrographs of Figure 85 show that the utilized kneading parameters were sufficient for obtaining a uniform distribution of the BFS filler within PP matrix. The distribution uniformity was always achievable regardless of the filler type or loading. The higher-magnification SEM micrograph of Figure 86 shows the weak filler-matrix interface, which reflects incompatibility between unmodified-BFS and PP; As shown in Figure 87, the voids and the sharp-edged morphology of the slags increased the stress concentration at the interfacial zones, resulting in prevention of stress transfer between the matrix and the filler as well as premature failure and loss of ductility.

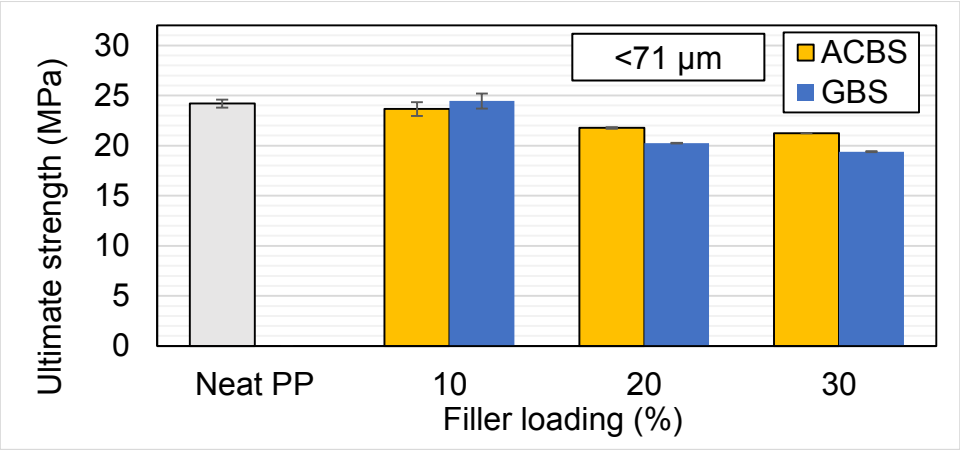

Figure 73: Ultimate strength at different <71 µm-BFS loadings.

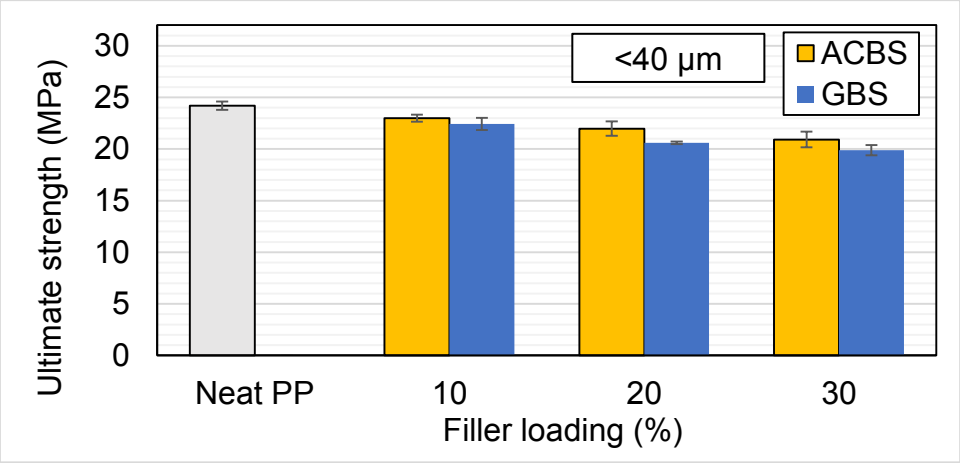

Figure 74: Ultimate strength at different <40 µm-BFS loadings.

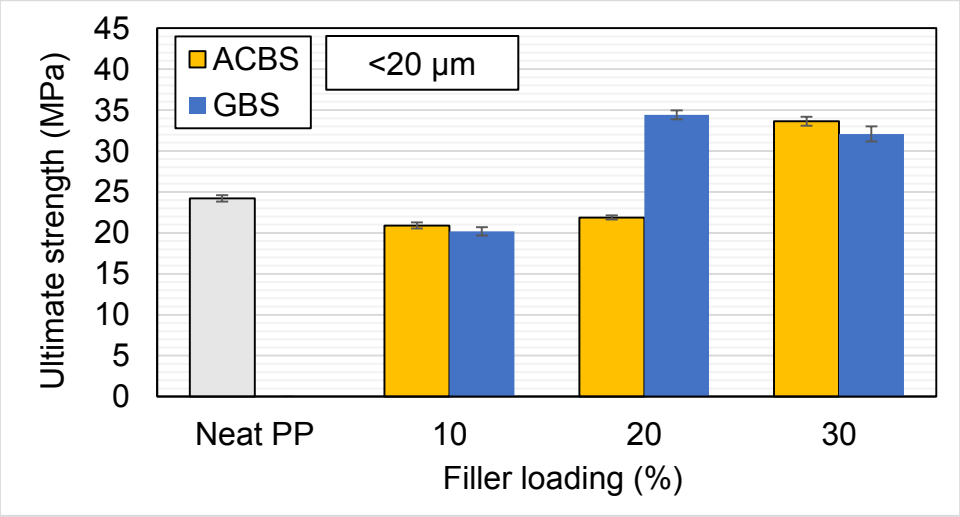

Figure 75: Ultimate strength at different <20 µm-BFS loadings.

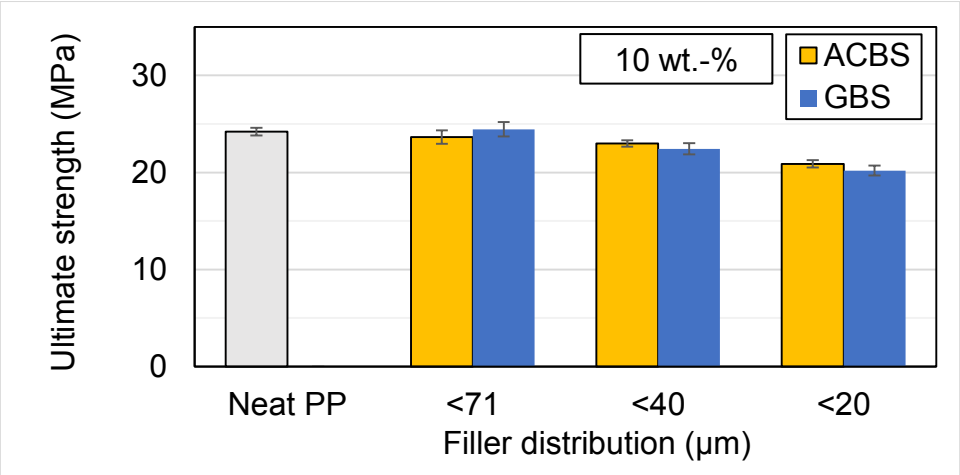

Figure 76: Ultimate Strength at different 10 wt.-%-BFS distributions.

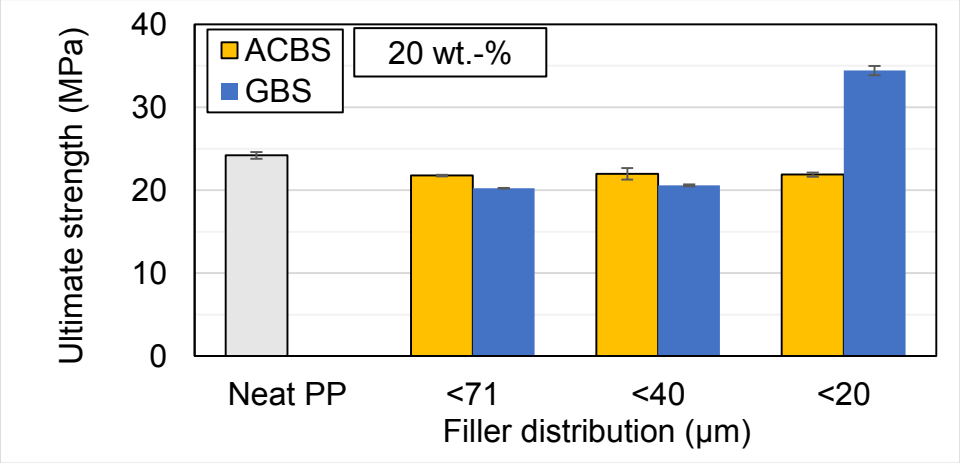

Figure 77: Ultimate Strength at different 20 wt.-%-BFS distributions.

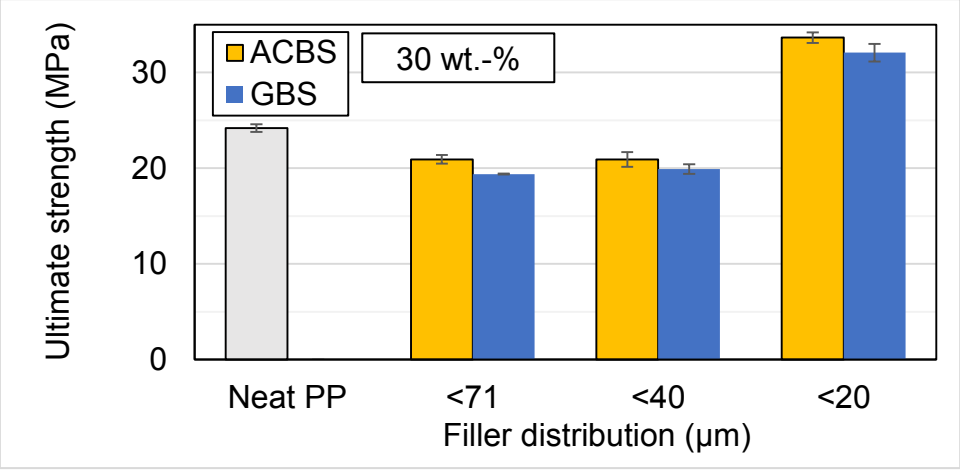

Figure 78: Ultimate Strength at different 30 wt.-%-BFS distributions.

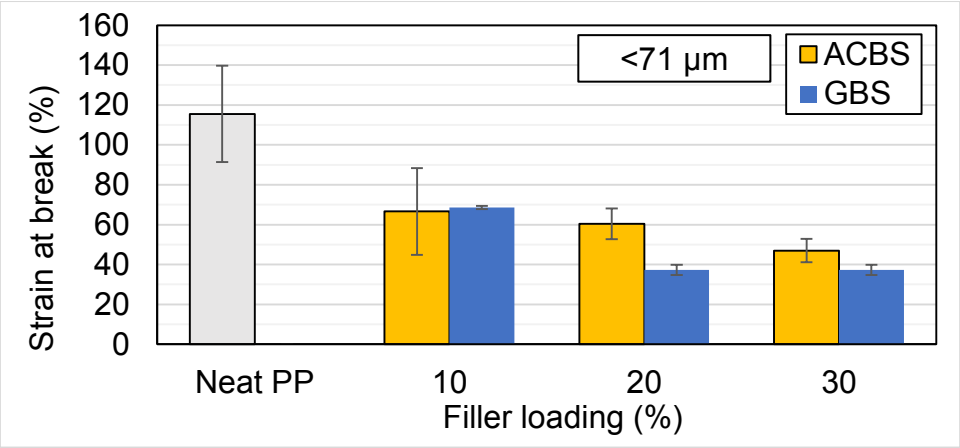

Figure 79: Strain at break at different <71 µm-BFS loadings.

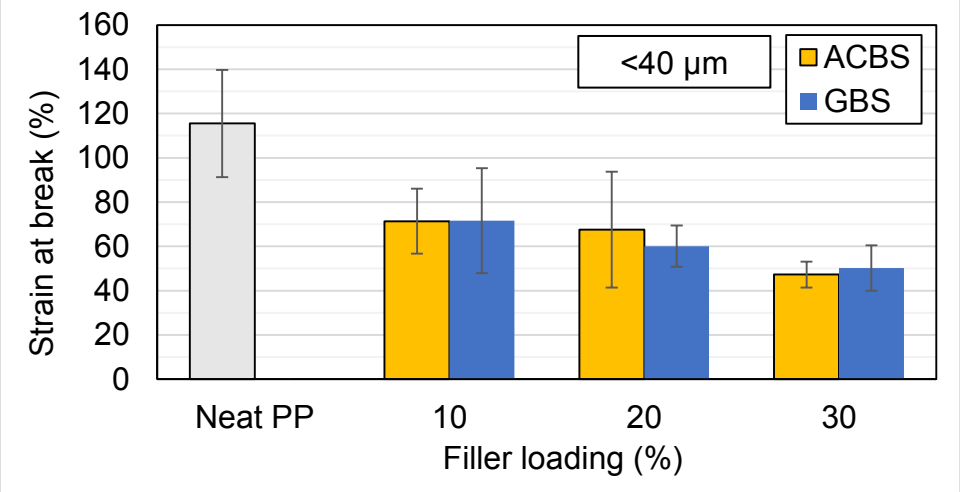

Figure 80: Strain at break at different <40 µm-BFS loadings.

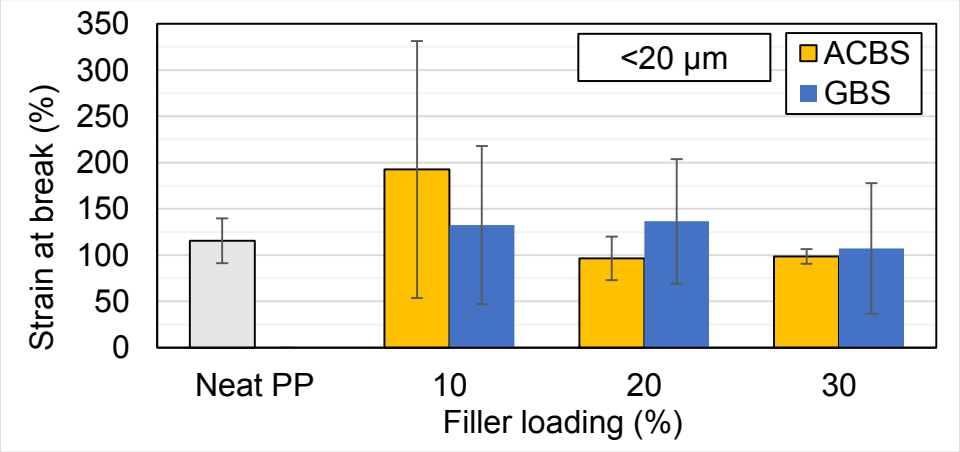

Figure 81: Strain at break at different <20 µm-BFS loadings.

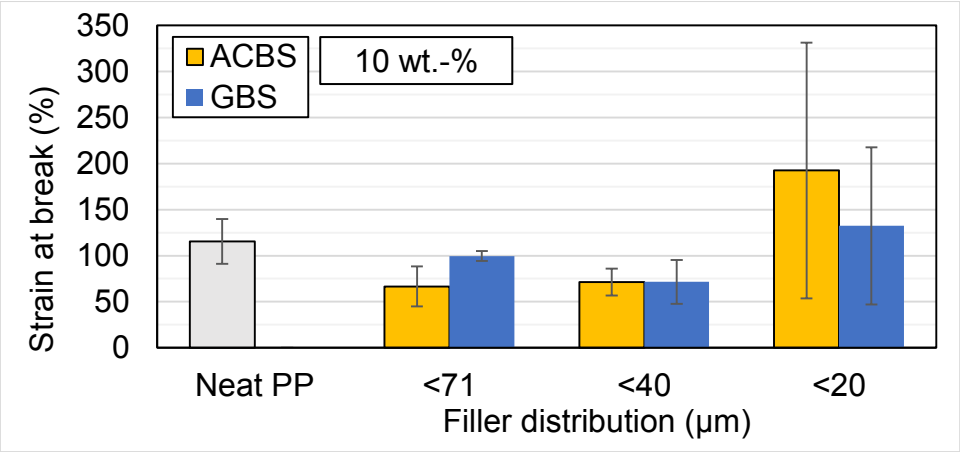

Figure 82: Strain at break at different 30 wt.-%-BFS distributions.

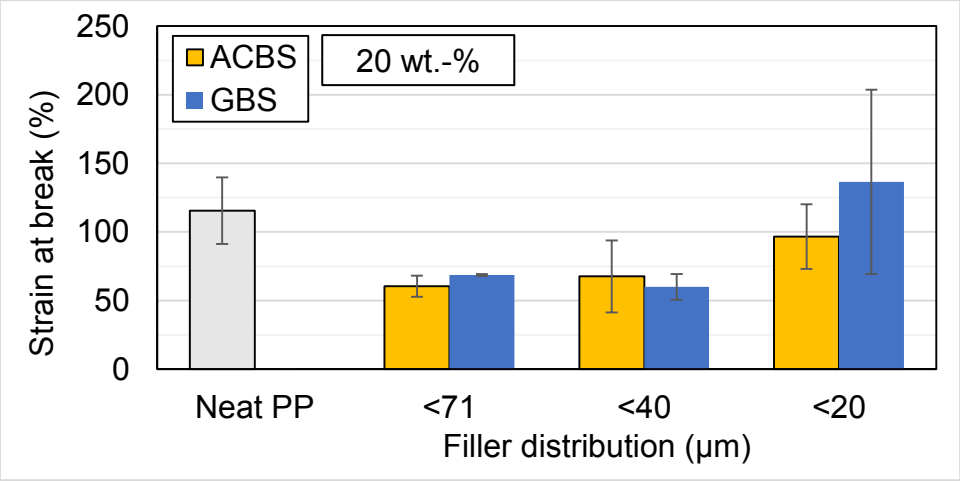

Figure 83: Strain at break at different 20 wt.-%-BFS distributions.

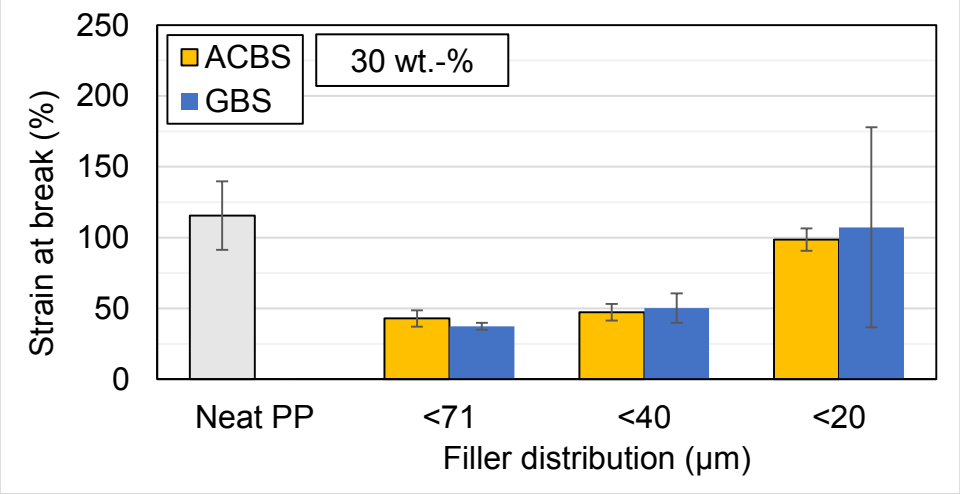

Figure 84: Strain at break at different 10 wt.-%-BFS distributions.

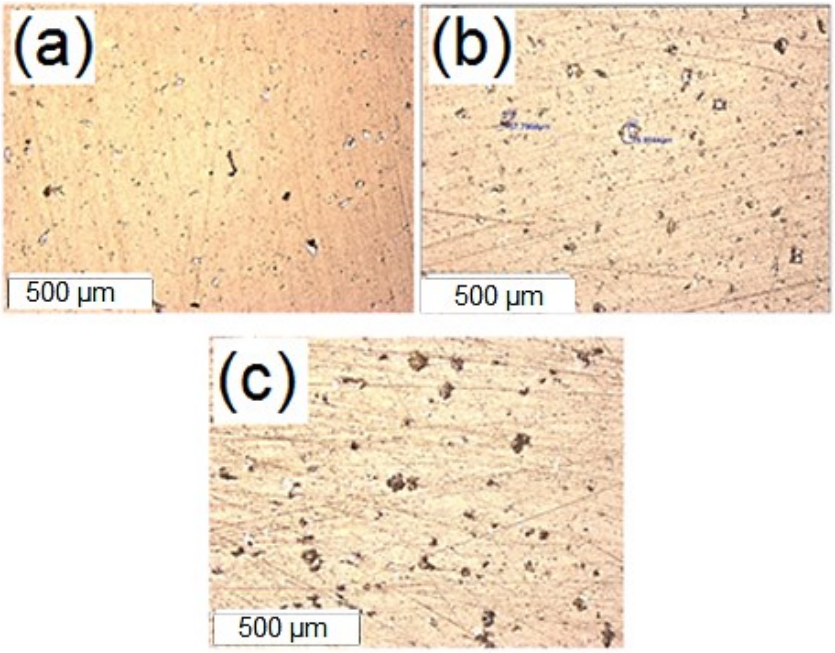

Figure 85: BFS distribution in (a) 10, (b) 20 and (c) 30 wt.-% <71µm-ACBS filled PP

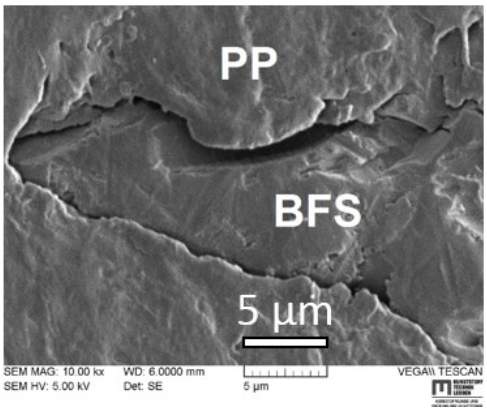

Figure 86: BFS-PP interface in the 20A71 compound.

4.2.1.4 Conclusions and outlook

The behaviour of the unmodified-BFS parameters was successfully investigated for PP. It was noticed that η^* proportionally increased with filler loading up to 35 % increase over the neat PP, regardless of the distribution or type of BFS. The <20 µm group recorded the lowest η^* among the three, which was expected due to the relatively low BFS particle size of this group compared to the other two. For the thermal properties, the DOC recorded a linear decrease with increasing BFS loading up to

40 % compared to the neat PP; however, the DOC was almost unaffected by the BFS distribution. It was also witnessed that incorporating 20 wt.-% of unmodified-BFS increased the thermal conductivity of PP by nearly 40 %. In agreement with the rheological behavior, the tensile stiffness increased linearly with BFS loading up to 20 % compared to the neat PP; however, no influence from BFS type or distribution was recorded. The ultimate strength decreased with increasing the filler loading except for the <20 µm. In addition, depending on the loading, BFS distribution affected the ultimate strength differently, where at <20 µm the ultimate strength increased by almost 70 % compared to the neat PP. Finally, the ductility was largely affected by the stress concentration induced by the unmodified and sharp-edged BFS particles, leading to immature failure and wide variations in the replicate ductility in most cases. However, at only < 20 µm distribution, the strain at break was almost comparable to the neat PP.

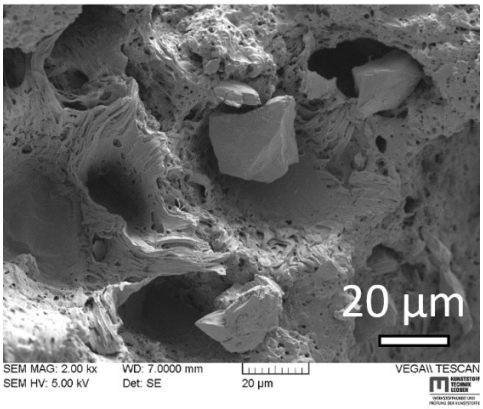

Figure 87: BFS debonding from the PP matrix in the 20A71 compound.

Outlook

From technical perspective, the previous findings as well as a short statistical investigation, shown in the Appendix, suggested that the '30A/G20' compounds could be the best candidate compounds for further investigation. However, the chosen compounds were the '20A/G71' compounds instead. The justification for this choice was based on the following considerations:

1. **The choice of 20 wt.-% loading:** to compare the modified-BFS filled compounds with ‘ME268AI’, a commercial PP copolymer filled mineral fillers at a loading of 20 wt.-%, which is utilized for automotive trim applications.
2. **The choice of <71 µm distribution:** to avoid processability difficulties and save time, since the grinding and sieving of enough amounts of <40 and <20 µm patches for TSC-compounding was time consuming and could have delayed the findings of this part beyond the constructed time plan.

4.2.2 Experiment 2: Influence of kneading parameters

The purpose of this experiment was to investigate the influence of two kneading process parameters, kneading speed and duration, upon the three property groups of PP as well as the kneading torque (M_d) the consumed specific energy of the kneading process (E_k). The compound chosen for this experiment was ‘20A20’, as it was readily available from the previous work. In fact, it was much more efficient and time saving to utilize a ready compound rather than waiting for the time-consuming preparation processes of another slag patch. In addition, the compound formulation was not of a great importance in this particular experiment because it was fixed throughout the experiment. The rheological test of this particular experiment was performed at 180 °C (instead of 200 °C utilized for all the rheological tests in this thesis). This was intended to compare the influence of the temperature upon the η^*, as discussed in the rheological findings section.

4.2.2.1 Process calculations

Figure 88 shows the kneader’s online process graph for the ’20A20 60,10’ compound. The red curve depicts the evolution of the mass temperature during the kneading process, while the blue curve corresponds to the evolution M_d. After addition of PP granulates, the kneading torque increased gradually, reflecting the increase of shear viscosity of the softening polymer. The increase of the kneading torque continued until an M_d peak was reached after nearly 180 seconds of kneading, beyond which the PP torque started to decrease and stabilize, reflecting a decrease followed by a stabilization of the compound shear viscosity. After five minutes of blade rotation, ACBS filler was added to the softened PP, where the dispersion of ACBS triggered a

slight increase in the kneading torque of the compound, followed by a stabilized torque plateau that reflected a complete dispersion of BFS in PP. A similar scenario was reported by Premalal et al. [81], where a rise husk (RHP) filler was kneaded with PP utilizing similar kneading parameters to those illustrated in the current work. The increase of kneading torque that accompanies the dispersion of RHP was reported to be caused by RHP particles restricting the mobility of PP macromolecular chains. The stabilized M_d values were averaged and plotted for each compound. E_k was calculated according to equation 1 in section 2.5.6 and superimposed on the same graph. Figure 89 and Figure 90 show the evolution of both M_d and E_k with the kneading speed at the kneading duration of 10 and 20 min, respectively. For the inspection of both figures, it was noticed that M_d and E_k increased almost linearly with the kneading speed. An increase of almost 40 % in M_d and 150 % in E_k was observed as the kneading speed increased from 60 to 120 rpm. In Figure 91, E_k was observed to be proportional to the kneading duration. This trend was shown to be consistent at the three kneading speed settings.

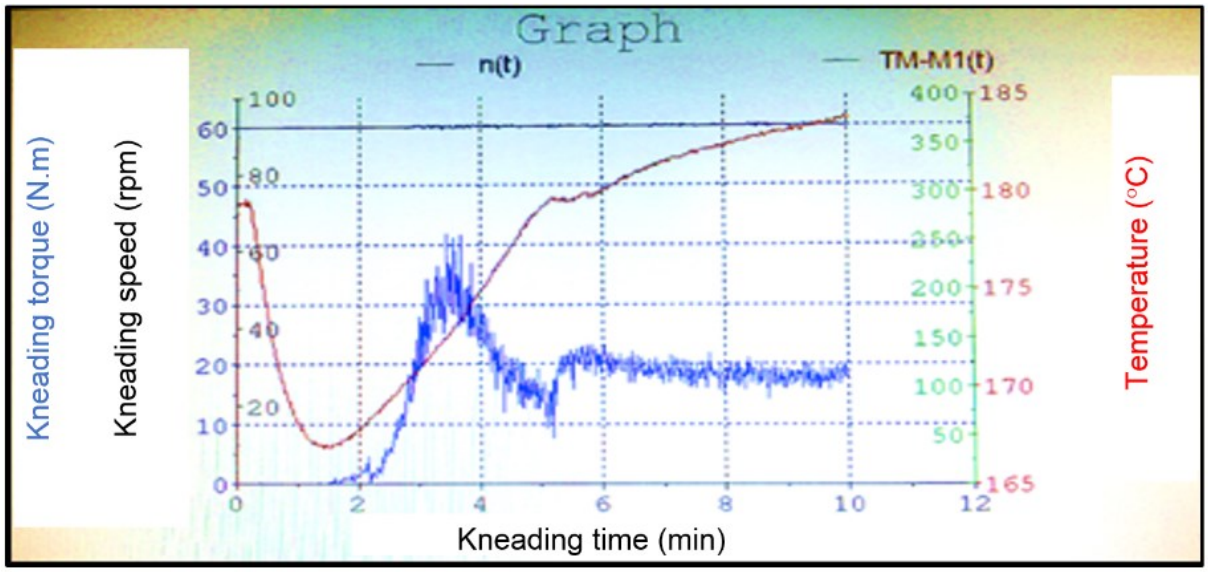

Figure 88: In situ kneading process graph for the '20A20 60,10' compound

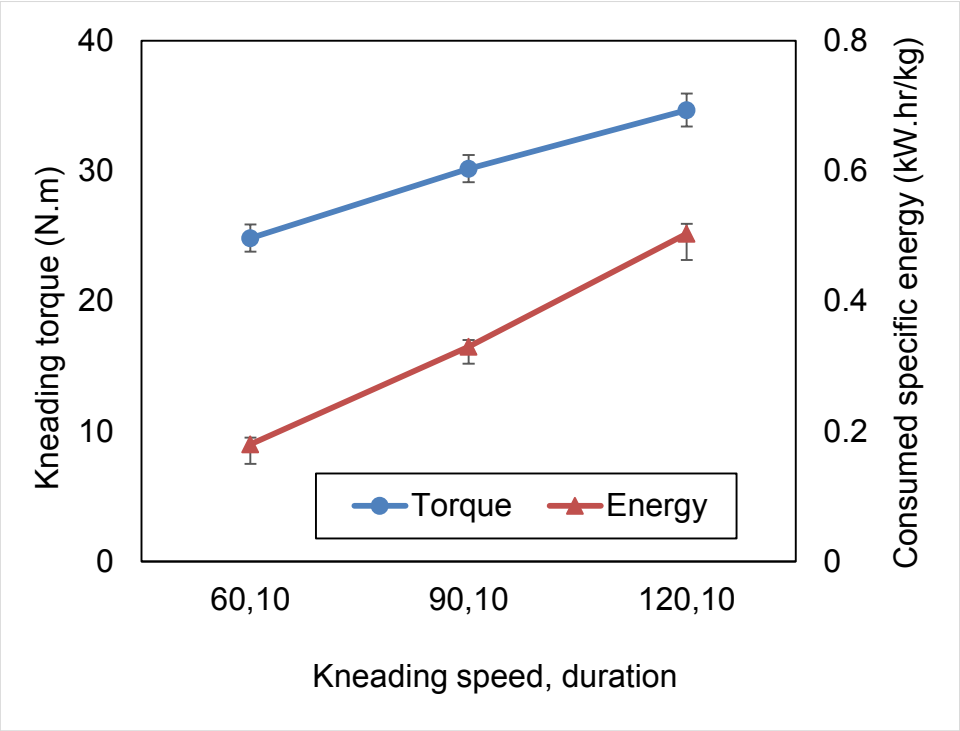

Figure 89: Kneading torque and consumed specific energy at 10-min kneading

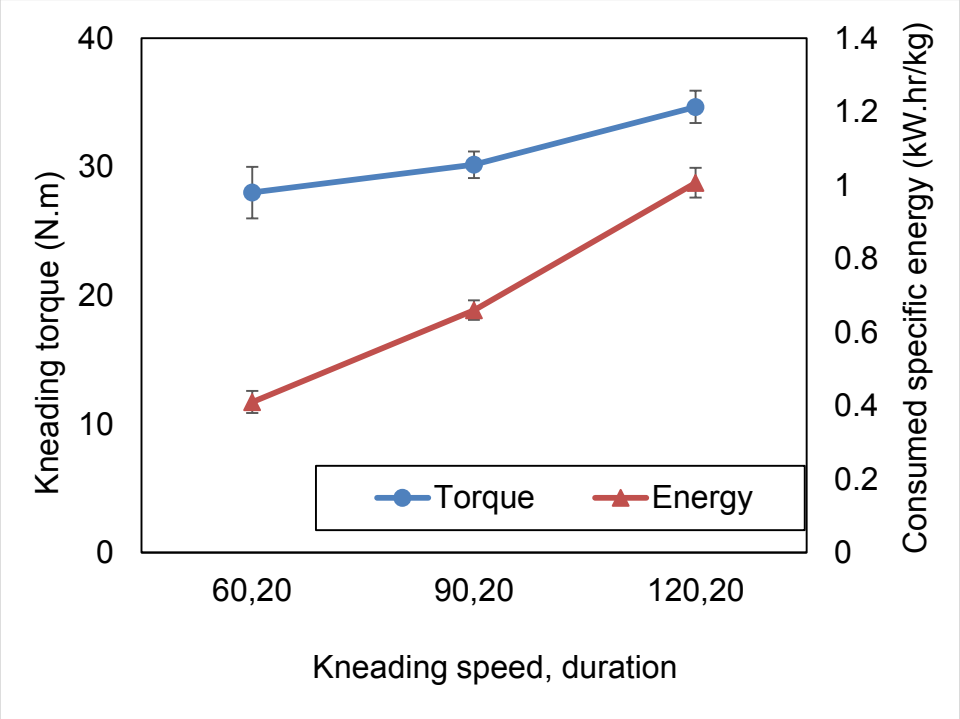

Figure 90: Kneading torque and consumed specific energy at 20-min kneading

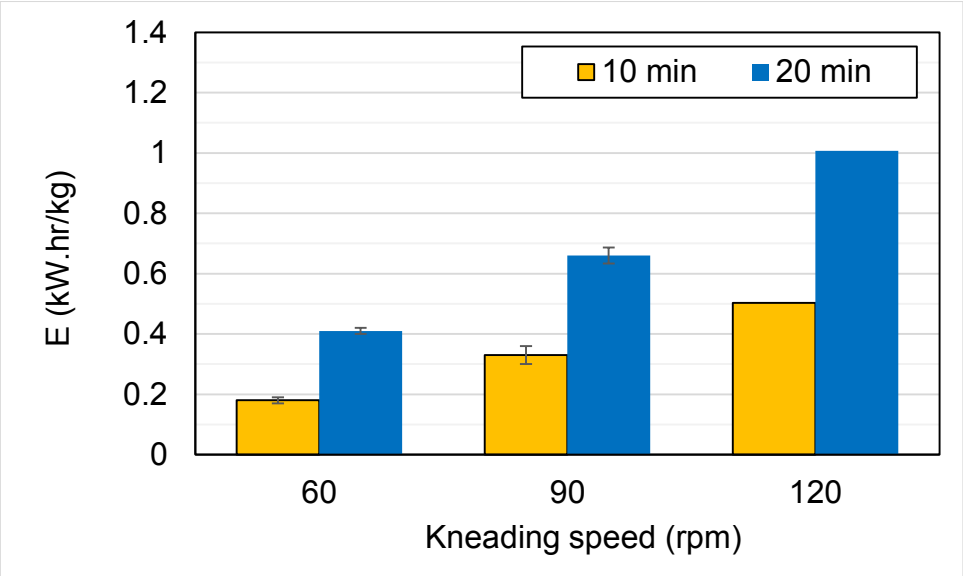

Figure 91: Consumed specific energy at for all parameter combinations.

4.2.2.2 Rheological behavior

The data for η*, G´ and G´´ of the compounds at 180 °C as compared to neat PP are listed in Table 30. As shown in Figure 92 and Figure 93, a typical shear thinning behavior was dominating for all the compounds along the shear rate range. The highest η* corresponded to the '20A20 120,10' compound with almost 21 % increase above the neat PP. The highest G´ and G´´, on the other hand, corresponded to the '20A20 60,20' compound, with nearly 30 and 26 % increase above the neat PP, respectively. Figure 94 demonstrates that within the indicated margin of error, the variation of the kneading speed and duration hardly influenced the η* of the '20A20' compound, which was expected as the compound loading was fixed in all trials. It was also noticed that both GBS and ACBS showed comparable η* levels. In Figure 95, η* levels for both neat PP and '20A20' compound at the rheological testing temperatures of 180 and 200 °C were compared. It was observed that compound temperature had a strong effect on the η*, where increasing the testing temperature corresponded to a 30 % decrease in η*. Such decrease was expected due to enhanced movement of the polymer molecular chains relative to each other as the temperature increases. The decrease in η* was seen to be independent of the compound type.

Table 30: Rheological findings for experiment 2 (at 180 °C and 0.1 1/s).

Code	Storage modulus (Pa)	±D	Loss modulus (Pa)	±D	Complex shear viscosity (Pa.s)	±D
Neat PP 60,10	769	20	2676	80	27840	409
20A20 60,10	870	17	2997	55	31210	138
20A20 60,20	994	17	3393	52	35355	195
20A20 90,10	924	14	3136	59	32690	408
20A20 90,20	920	11	3127	42	32600	271
20A20 120,10	947	20	3223	44	33585	466
20A20 120, 20	935	14	3185	65	33195	156

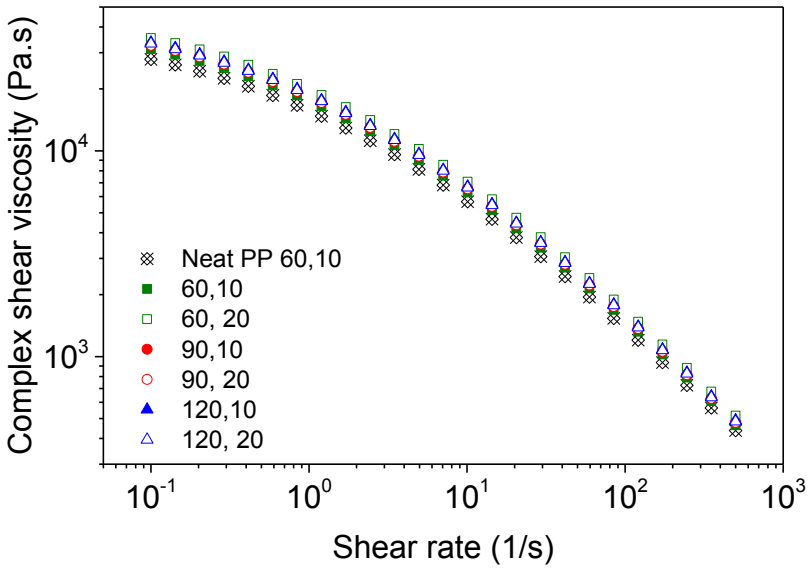

Figure 92: Complex shear viscosity for parameter combinations and neat PP.

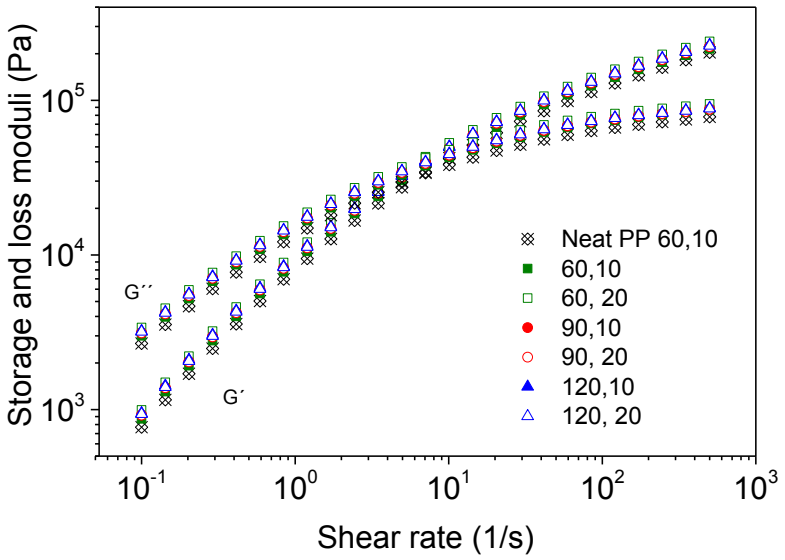

Figure 93: Storage- and loss moduli for parameter combinations and neat PP.

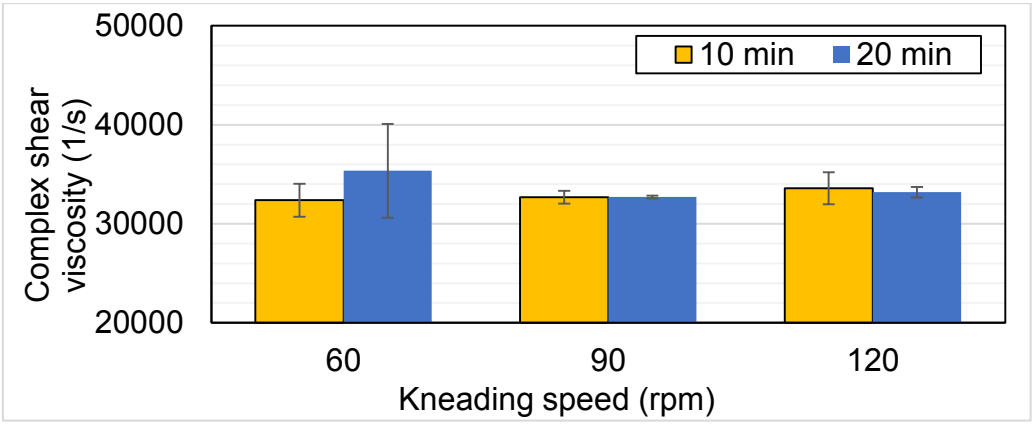

Figure 94: Complex shear viscosity at different parameter combinations.

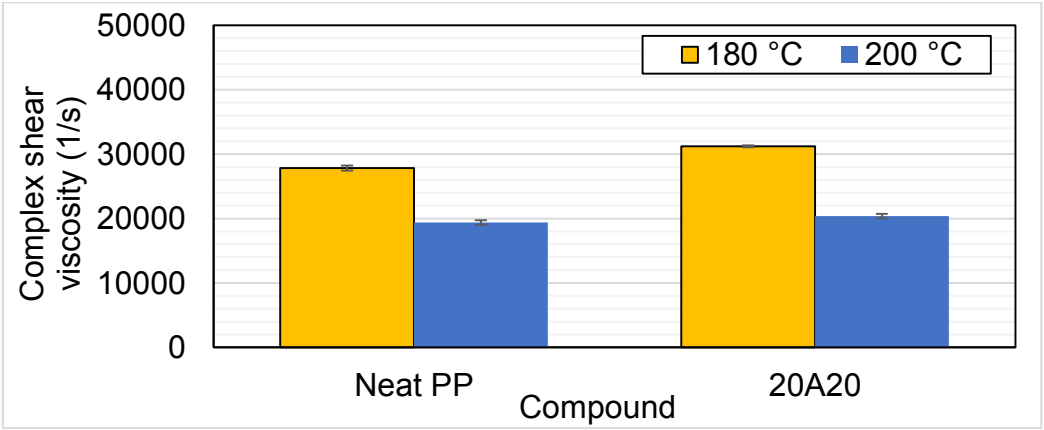

Figure 95: Complex shear viscosity at 180 and 200 °C

4.2.2.3 Thermal behavior

The DSC findings are shown in Table 31. Within the indicated margin of error, it was observed that the variation of the kneading parameters had minimal influence upon the T_c, T_m and DOC of the compounds. As compared to the neat PP, a decrease of at least 20, 15, 7 and 10 % was observed for the $\Delta H_{m,\ first\ heating}$, ΔH_c, $\Delta H_{m,\ second\ heating}$ and DOC of the filled compounds, respectively. This decrease was mainly associated with the addition of the BFS, as previously discussed.

Table 31: Thermal findings of experiment 2.

	First heating				Cooling				Second heating				DOC (%)	
Code	T_m (°C)		ΔH_m (J/g)		T_c (°C)		ΔH_c (J/g)		T_m (°C)		ΔH_m (J/g)			
Neat 60,10	168.2	±0.6	94.5	±6.9	118.9	±0.6	91.6	±13.4	167.6	±0.7	92.5	±11.2	44.7	±0.7
60,10	168.4	±0.9	79.7	±10.4	118.5	±0.6	76.5	±14.3	168.9	±0.2	86.1	±1.4	39.7	±2.2
60,20	168.1	±0.4	84.5	±2.6	118.5	±0.3	83.0	±4.6	167.5	±0.3	84.9	±4.0	40.5	±0.1
90,10	167.8	±0.4	84.8	±5.1	118.3	±0.1	79.2	±4.3	167.4	±0.5	79.9	±9.9	39.4	±1.6
90,20	167.7	±0.1	82.8	±5.8	118.7	±0.1	80.9	±9.9	167.3	±0.2	84.2	±7.3	40.0	±0.5
120,10	167.7	±0.2	82.0	±4.4	118.1	±0.8	76.9	±7.2	167.3	±0.2	82.4	±7.7	39.3	±0.2
120,20	167.8	±0.2	85.7	±4.7	118.4	±0.2	81.4	±4.2	167.3	±0.3	87.6	±4.3	41.5	±0.6

4.2.2.4 Mechanical behavior

The findings of the tensile testing are listed in Table 32. Comparing the neat PP and filled ’60,10’ compounds, it was observed that the tensile stiffness of the filled compounds was 5 – 10 % higher than that of neat PP due to the influence of BFS as a rigid filler [7]. The tensile stiffness levels of the filled compounds were rather comparable, which was expected due to the fixed loading of BFS. The tensile stiffness level of the filled compounds was stable despite the PP softening that took place upon increasing the kneading duration, as shown in Figure 97. This stability could be attributed to a balancing effect between softening and strain hardening, where the softening effect was possibly negated by a counteracting strain hardening effect associated with increasing the shear stresses at higher kneading speeds.

It was also shown that the ultimate strength and strain at break values of the filled compounds were comparable. The mean strain at break values tended to be proportional to the increase in kneading speed and duration, but the large statistical

error margin for the strain at break values did not allow for an accurate detection of any patterns. The influence of the kneading speed on the strength at break level is demonstrated in Figure 96. At the lowest speed setting, the strength at break increased by at least 20 % after doubling the kneading duration. This might be due to the increased shear and associated strain hardening. The trend was reversed upon switching to the 90 rpm setting, where generation of frictional heat might have overcome the hardening effect. At the maximum speed setting, the kneading duration hardly affected the strength at break level, which remained at almost 20 MPa. This might indicate that the softening effect was very dominant at this stage.

Table 32: Mechanical findings of experiment 2.

Compound code	Young's modulus (MPa)	±D	Ultimate strength (MPa)	±D	Strength at break (MPa)	±D	Strain at break (%)	±D
Neat 60,10	1487	32	23.6	1.1	18.2	0.8	94	31
60,10	1657	40	23.7	0.2	17.2	2.5	91	19
60,20	1555	61	25.1	0.8	23.7	0.2	70	44
90,10	1613	15	24.9	0.3	24.9	0.3	116	23
90,20	1733	107	25.5	0.1	19.8	0.3	96	56
120,10	1663	60	25.2	0.1	20.6	0.4	133	38
120,20	1720	44	25.9	0.8	20.7	1.5	129	34

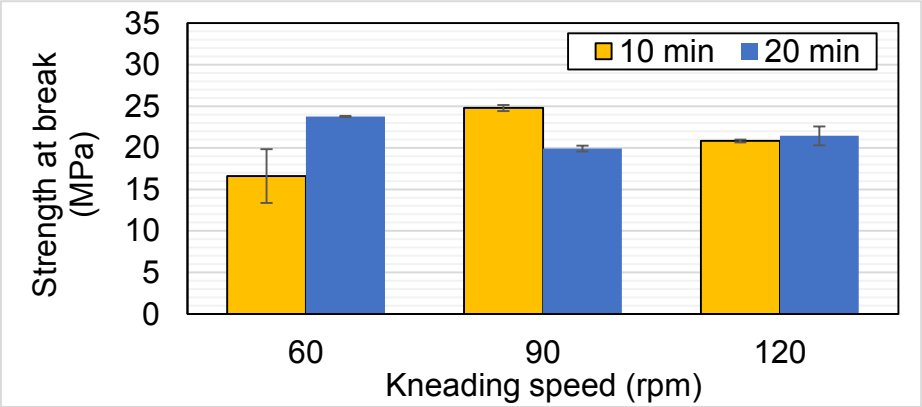

Figure 96: Strength at break at different parameter combinations.

4.2.2.5 Conclusions

The findings of this experiments showed how the variation of the kneaded process parameters influenced the consumed energy and properties of the '20A20' compound.

It was shown that both E_k and M_d were proportional to the kneading speed. The η^* was only affected by the kneading temperature. Furthermore, the parameters showed hardly influenced the thermal- and mechanical properties; an exception was the strength at break level, which was differently affected by the kneading duration depending on the utilized speed setting.

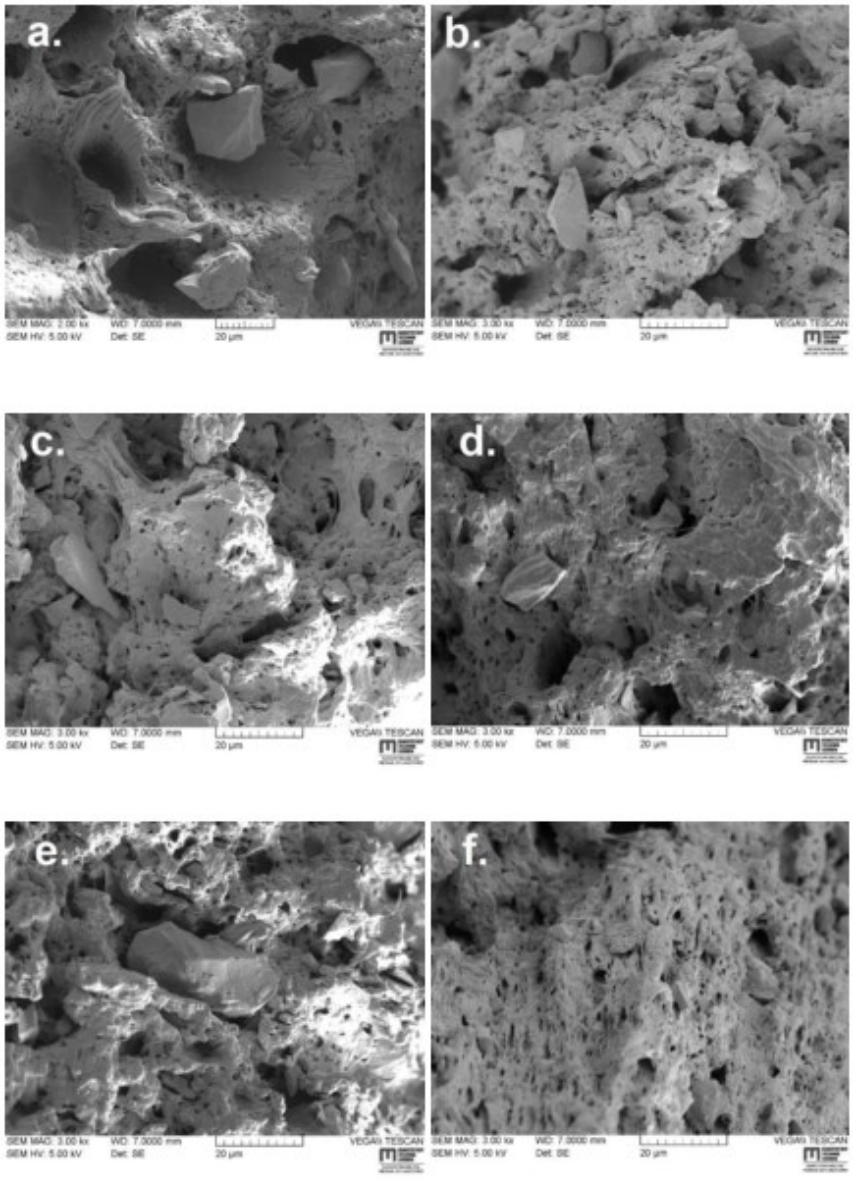

Figure 97: Fracture SEM micrograph for the kneaded BFS-filled PP compounds: (a) 60, 10, (b) 60, 20, (c) 90, 10, (d) 90, 20, (d) 120, 10 and (f) 120, 20.

4.2.3 Experiment 3: Comparative study (kneading versus TSC)

The purpose of this experiment was to compare the processing approach, laboratory kneading versus TSC, in terms of the consumed specific energy as well as the properties of selected BFS filled compounds, '20A/G71' and '20A20', which were chosen in the previous experiments. As comparable mass temperature profiles as possible were adjusted for both the kneading and TSC processes.

4.2.3.1 Process calculations

E_k, E_{TSC} and the mean residence time (t_{mean}) of the TSC process were calculated by the equations of section 2.5.6. Table 33 shows that the t_{mean} for TSC process was 55 s as compared with 600 s for the kneading process. The calculated M_d was doubled for in the TSC process. The calculated E_k *and* E_{TSC} values were 0.15 and 0.1 kW·h/kg for kneading and TSC processes, respectively. Comparable power consumption values of both the kneader and TSC were expected, since for the laboratory kneader, relatively low power is consumed, due to the low mixing speeds, for a high mixing duration. For TSC, the opposite is true. Low- and high shear mixers at comparable processing temperatures was reported by Park et al. [74], where the team showed comparable *E* values for low and high-shear mixers employed in processing wood fiber filled low density polyethylene, where TSC is considered as a high-shear mixer.

Table 33: Calculated E and t_{mean}.

Melt compounding process	**Kneading**	**TSC**
Torque (M_d) (N·m)	20	40
Consumed specific energy (*E*) (kW·h/kg)	0.15	0.1
Mean residence time (t_{mean}) (s)	600	55

4.2.3.2 Rheological behavior

The rheological parameters of the kneaded- and corresponding TSC compounds as compared to the neat PP are listed in Table 34, while the graphical representation is shown in Figure 98 and Figure 99. As discussed in the previous sections, a typical shear thinning behavior predominated for all compounds in the shear rate range of 0.1 to 500 1/s. Figure 100 shows the η^* of the kneaded- and TSCed compounds. For neat

PP, the margin of error for the TSC compound was quite large, making it difficult to conclude the effect of the mixing technique. However, the difference between the kneaded and TSC levels for the filled compounds was distinct. It was observed that the η^* levels of the kneaded compounds were 8 – 10 % higher than the correspondent TSC ones. This is likely attributed to the dispersive mixing capability of the TSC technique. In contrast to the distributive mixing during the kneading process, the high shear stresses taking place within the dispersive mixing of the TSC were capable of rupturing the slag particles into finer ones. The rupturing process could disintegrate many coarse particles into finer particulates with lower resistance to the melt flow, which can reduce the η^* levels. This situation is likely to occur in systems with micron-sized fillers, where the relatively coarse particles were unlikely to agglomerate and cause a counteracting increase in the η^* levels.

Table 34: Shear rheology findings of experiment 3 (at 200 °C and 0.1 1/s).

Code	Storage modulus (Pa)	±D	Loss modulus (Pa)	±D	Complex shear viscosity (Pa.s)	±D
Neat PP	459	18	1884	69	19390	351
Neat PP TSC	446	28	2129	102	21925	1054
20A20	494	18	1977	75	20380	339
20A20 TSC	413	16	1848	74	18930	379
20A71	512	12	2102	59	21630	424
20A71 TSC	421	17	1887	87	19330	578
20G71	528	10	2163	69	22265	502
20G71 TSC	422	11	1884	85	19300	416

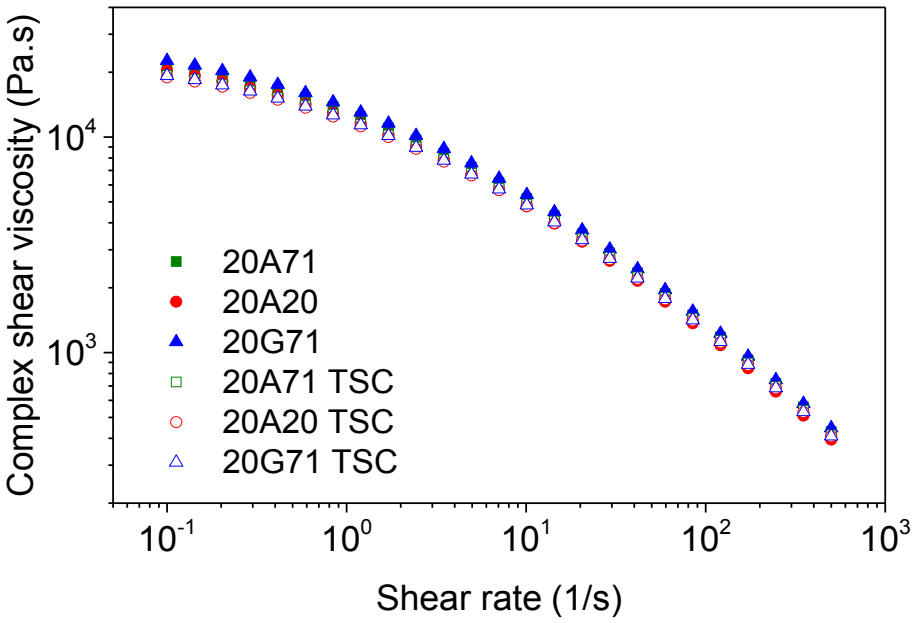

Figure 98: Complex shear viscosity of the kneaded/TSCed compounds.

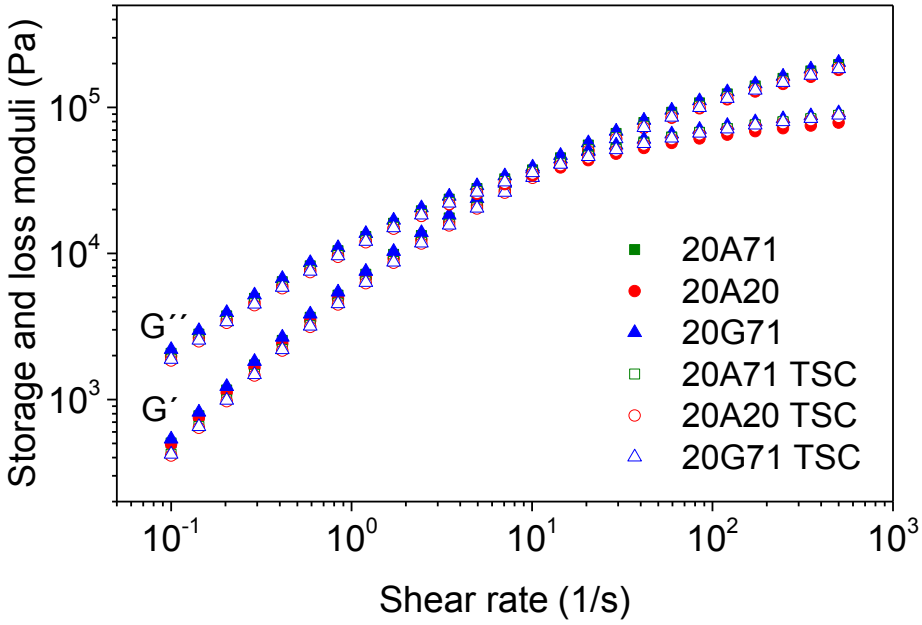

Figure 99: Shear- and loss moduli of the kneaded/TSCed compounds.

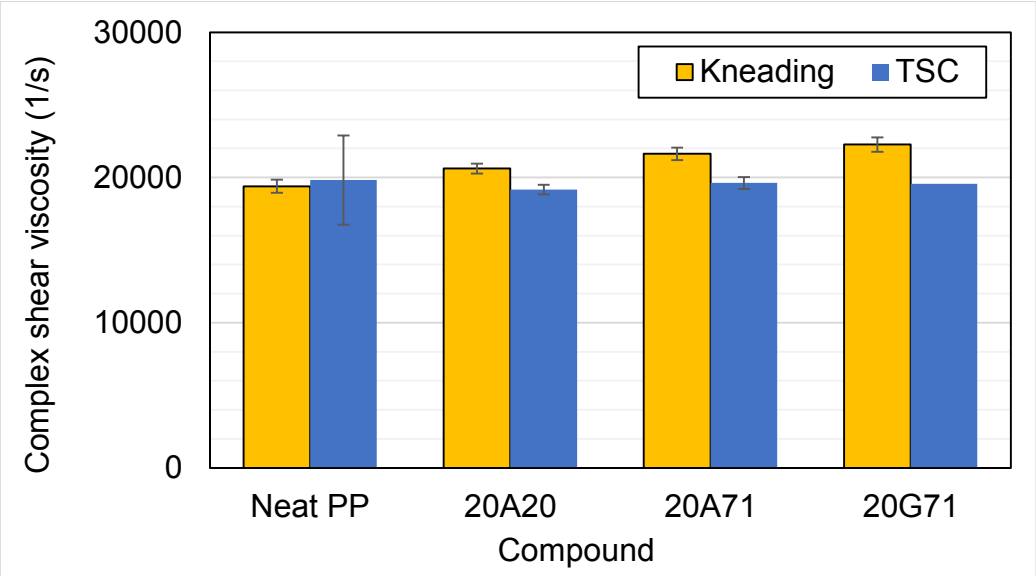

Figure 100: Complex shear viscosity for the kneaded/TSCed compounds

4.2.3.3 Thermal behavior

Table 35 shows that the neat PP and the kneaded-/TSC compounds exhibited comparable T_m values. A decrease of 10 – 50 % was found, however, for the compounds' $\Delta H_{c/m}$ and DOC levels as compared to the neat PP. As previously discussed, this decrease was driven by the interaction between BFS and the PP matrix.

Figure 101 shows that the T_c for TSC compounds increased by 1 - 2 % as compared to their kneaded counterparts. Figure 102 and Figure 103 demonstrate that the ΔH_c and ΔH_m of the TSCed '20A71' were almost 10 % higher than their kneaded correspondents. In Figure 103 and Figure 104, it was however noticed that the ΔH_m and DOC was 10 % lower for the TSCed '20A20' compared to the kneaded twin. Figure 104 reveal that the difference between the DOC values of the kneaded and TSC compounds could be a function of the BFS distribution. That is, the DOC level for the kneaded '20A20' compound was higher, or at least comparable, to the corresponding TSCed one. The trend disappeared upon switching to the '20A/G71' compounds. As previously discussed, it is likely that the dispersive mixing of TSC helped decreasing the number of coarse BFS particles, which were disintegrated into finer particulates with lower resistance to the melt flow. This trend was more pronounced for the <71 µm distribution with larger BFS particles compared to the <20 µm.

Table 35: Thermal findings of experiment 3.

Code	First heating				Cooling				Second heating				DOC (%)	
	T_m (°C)		ΔH_m (J/g)		T_c (°C)		ΔH_c (J/g)		T_m (°C)		ΔH_m (J/g)			
Neat PP	168.17	±0.57	94	±6.94	118.87	±0.56	92	±13.40	167.56	±0.69	93	±11.18	44.3	±5.35
20A20	168.4	±0.62	80	±7.39	118.5	±0.39	77	±10.12	168.9	±0.17	86	±0.97	39.7	±2.17
20A20 TSC	167.5	±0.63	73	±5.47	119.8	±0.13	79	±5.08	167.5	±0.14	75	±4.55	35.5	±0.82
20A71	167.8	±0.00	68	±3.83	118.8	±0.12	67	±3.68	167.1	±0.09	68	±3.96	32.6	±0.12
20A71 TSC	167.8	±0.31	78	±2.84	119.7	±0.14	79	±2.95	167.5	±0.14	79	±3.16	37.7	±0.31
20G71	167.9	±0.06	73	±5.85	119.1	±0.25	74	±5.71	167.5	±0.41	74	±5.24	35.2	±0.06
20G71 TSC	167.7	±0.07	78	±5.75	119.6	±0.03	81	±5.14	167.2	±0.06	79	±4.98	37.6	±0.28

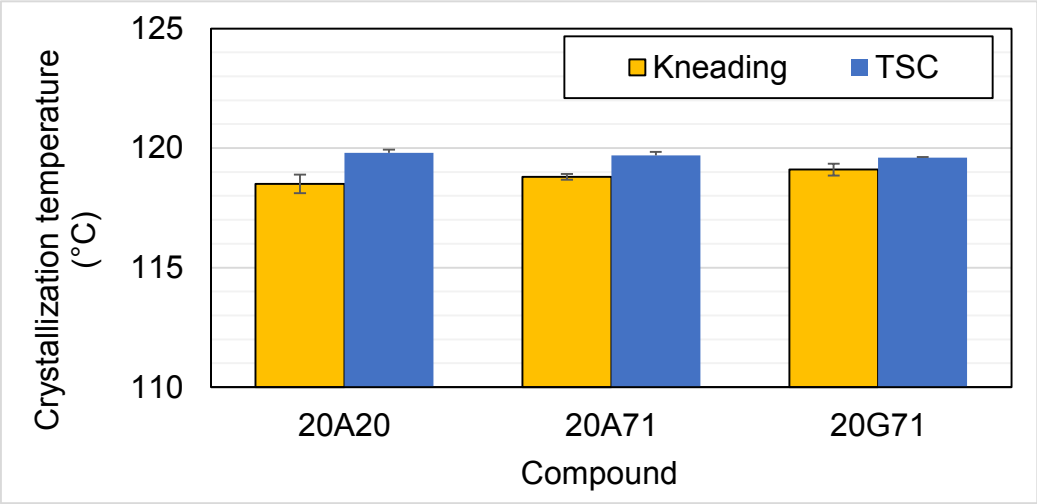

Figure 101: Crystallization temperature of the kneaded/TSCed compounds.

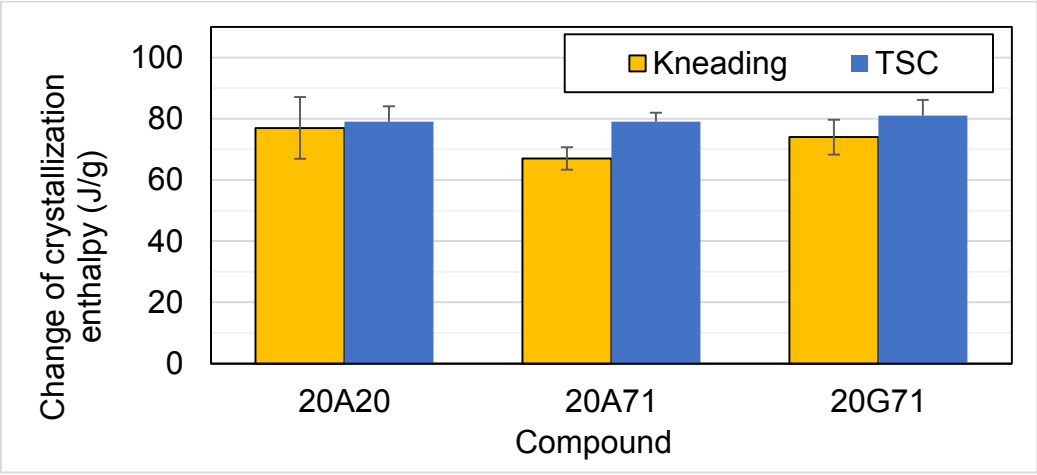

Figure 102: Change of crystallization enthalpy of the kneaded/TSCed compounds.

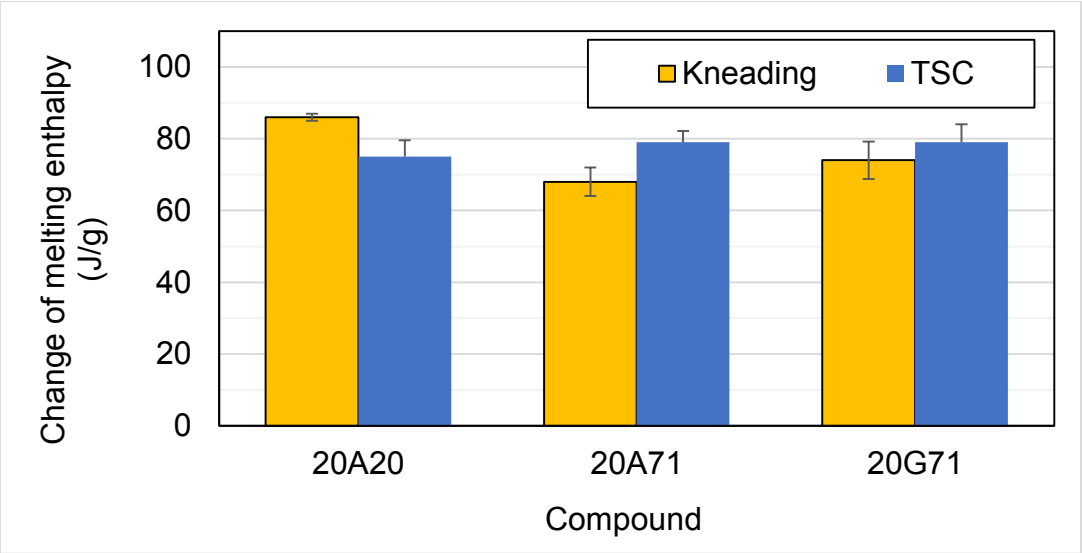

Figure 103: Change of melting enthalpy of the kneaded/TSCed compounds.

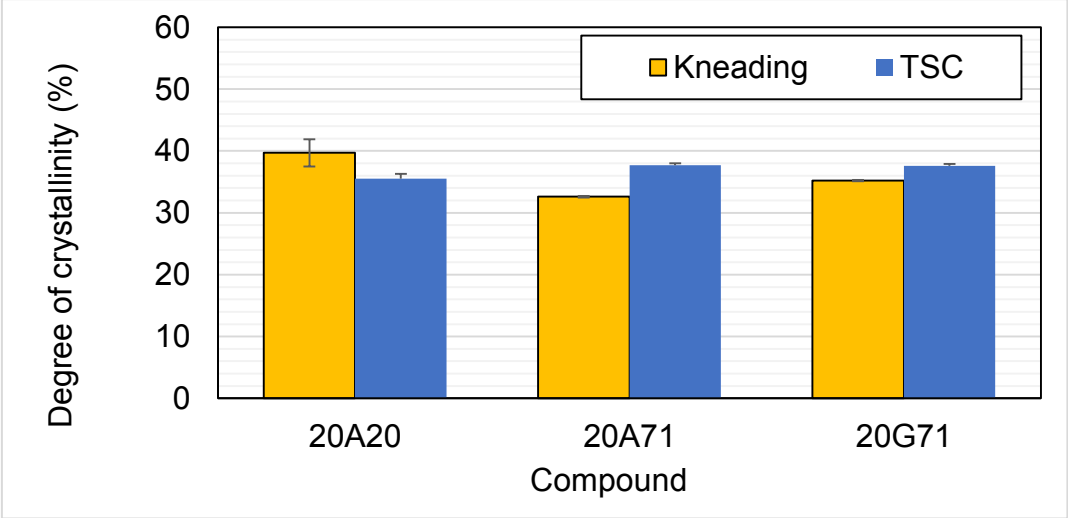

Figure 104: Degree of crystallinity of the kneaded/TSCed compounds.

Figure 105 - Figure 107 show the thermal conductivity levels for the neat PP and the '20A/G71' compounds. As previously discussed, the thermal conductivity levels of kneaded PP increased with increasing the testing temperature, with an overall increase of nearly 10 % from 25 to 100 °C. In contrast, the thermal conductivity level of the TSCed PP was stable over the test temperature range. The figures show that the thermal conductivity was insensitive to either the BFS type or the processing technique.

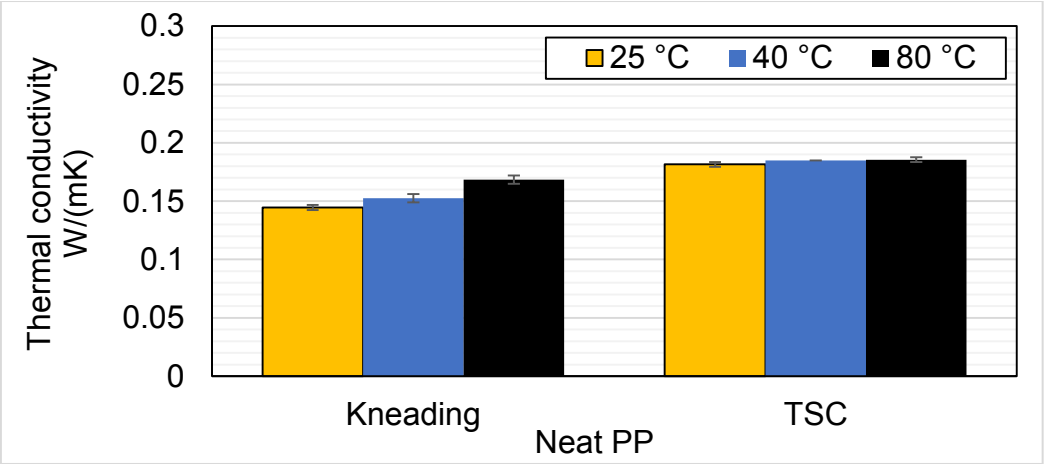

Figure 105: Thermal conductivity of the kneaded/TSCed neat PP.

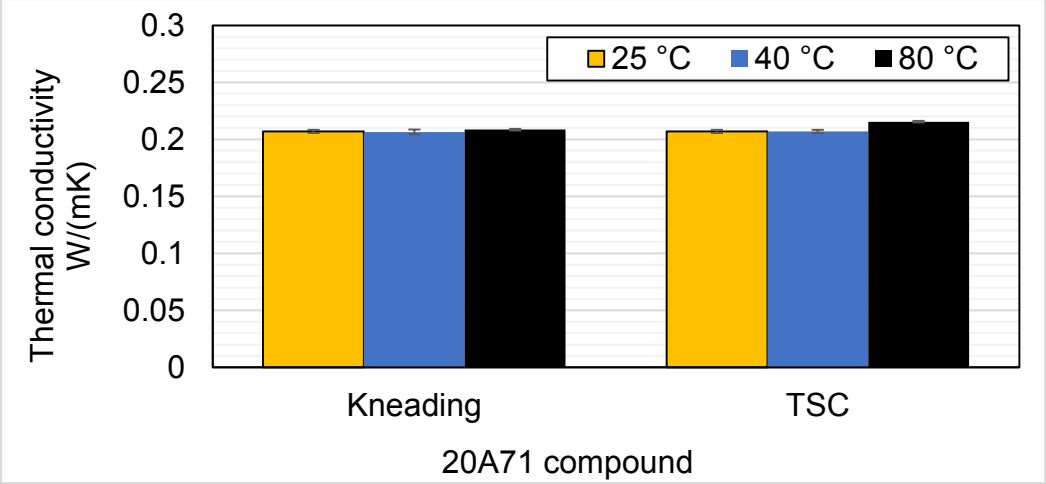

Figure 106: Thermal conductivity of the kneaded/TSCed compounds.

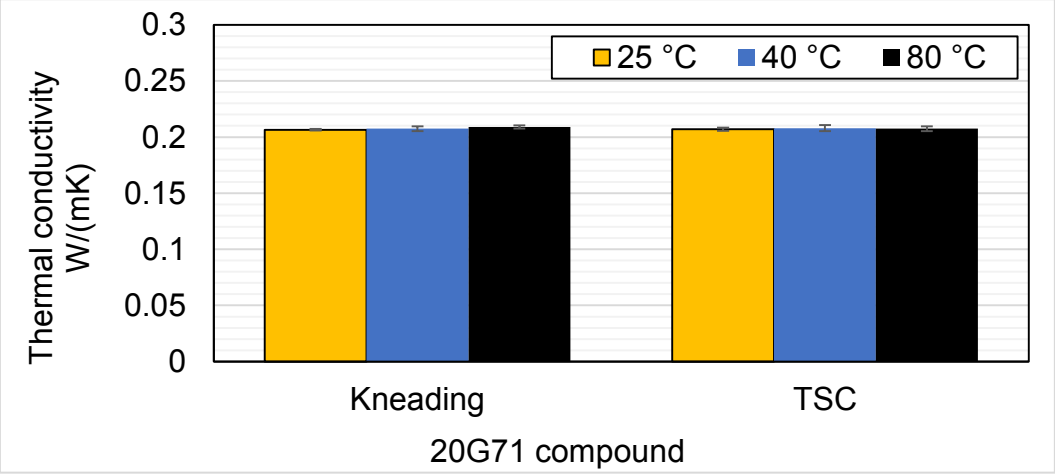

Figure 107: Thermal conductivity of the kneaded/TSCed compounds.

4.2.3.4 Mechanical behavior

The tensile properties of the kneaded- and TSC compounds are presented in Table 36. Nominal stress-strain curves for the compounds are shown in Figure 108. As previously discussed, addition of BFS slightly increased the Young's modulus of PP but decreased its strength and ductility. It was also discussed that the slag morphology and the presence of voids that acted as stress concentration sites were responsible for decreasing the strength and ductility levels of the filled compounds compared to the neat polymer.

Table 36: Mechanical findings of experiment 3.

Code	Young's modulus (MPa)	±D	Ultimate strength (MPa)	±D	Ultimate strain (%)	±D	Strength at break (MPa)	±D	Strain at break (%)	±D
Neat PP	1487	32	23.6	1.1	4.6	0.1	18.2	0.8	94	31
PP20A20	1678	33	21.9	0.2	4.4	0.2	17.1	0.4	43.3	10
PP20A20 TSC	1687	38	21.0	0.5	3.8	0.1	14.9	4.7	31.0	8.7
PP20A71	1794	94	21.8	0.1	3.9	0.2	17.3	0.4	60.5	7.7
PP20A71 TSC	1637	15	19.6	0.2	3.9	0.1	17.2	0.2	29.7	12.7
PP20G71	1742	26	20.3	0.1	3.9	0.1	16.7	0.4	68.7	3.2
PP20G71 TSC	1600	69	19.2	0.2	4.4	0.1	17.1	0.6	43.3	5.5

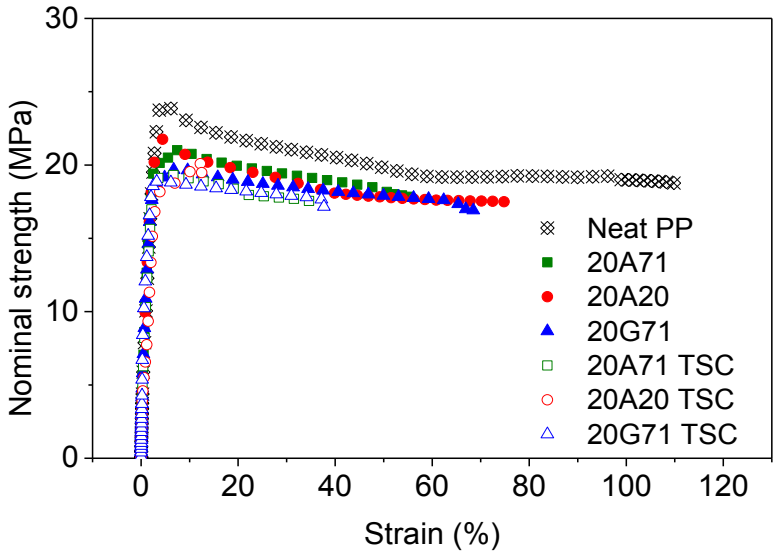

Figure 108: Stress-strain comparisons of the kneaded/TSCed compounds.

Figure 109 compares the tensile stiffness of the kneaded compounds with their TSCed counterparts. For the neat PP, it was observed that the tensile stiffness of the TSCed compound was about 20 % less than that of the kneaded twin. For the rest of the compounds, the stiffness level of the kneaded- and TSC compounds was almost matching considering the margin of error. The ultimate strength level of the TSCed compounds, Figure 110, was observed to be consistently 5 – 10 % less than that of the kneaded ones. This trend was independent of the compound type. For the ductility, Figure 111 indicates that the filled TSC compounds were more brittle than the kneaded ones. It was difficult to assign this pattern to the neat PP due to the latter's large margin of error.

To find a possible reason for the brittleness of TSC compounds compared to their kneaded counterparts, optical and fracture SEM micrographs of both compounds were investigated. The optical micrographs, Figure 112, showed that the BFS was uniformly distributed with the PP matrix in both kneaded- and TSCed compounds. The fracture SEM micrographs are shown in Figure 113. While the TSC compounds showed a rigid PP matrix, the kneaded twins showed a clear PP matrix elongation in the direction of load as well as particle separation wells, which indicates ductility. It is likely that the separation of the BFS particles from the PP matrix was driven by of two factors: (1) building up of stress concentration due to the irregular, sharp-edged BFS particle morphology and (2) the voids surrounding BFS filler particles, which were more evident in the TSC compound. Besides acting as stress concentration sites, these voids prevented any load transfer between the filler and the matrix, causing the material to fail prematurely.

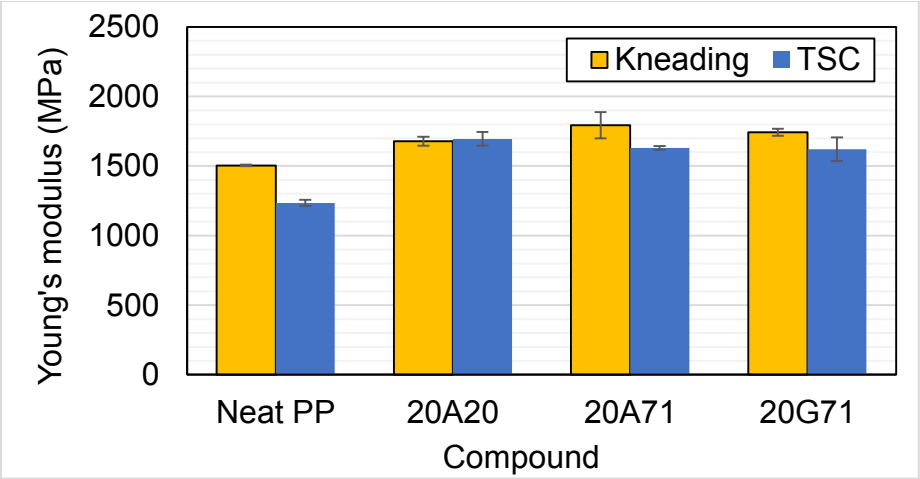

Figure 109: Young's modulus of the kneaded/TSCed compounds.

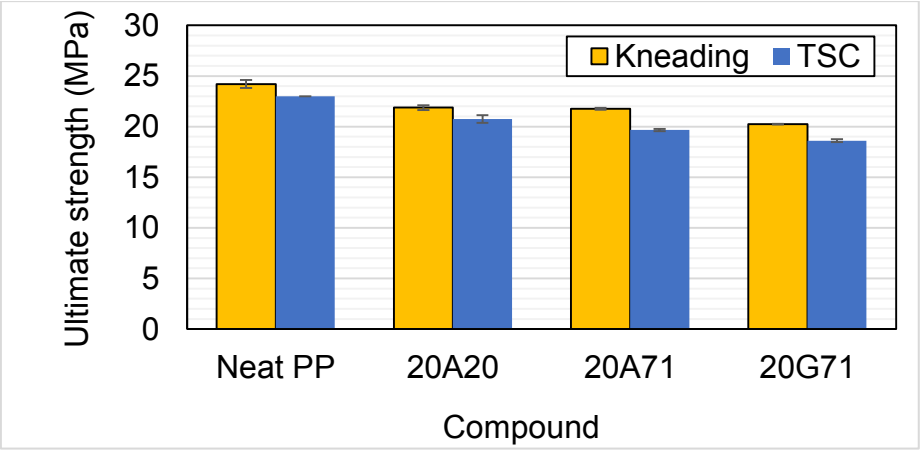

Figure 110: Ultimate strength of the kneaded/TSCed compounds.

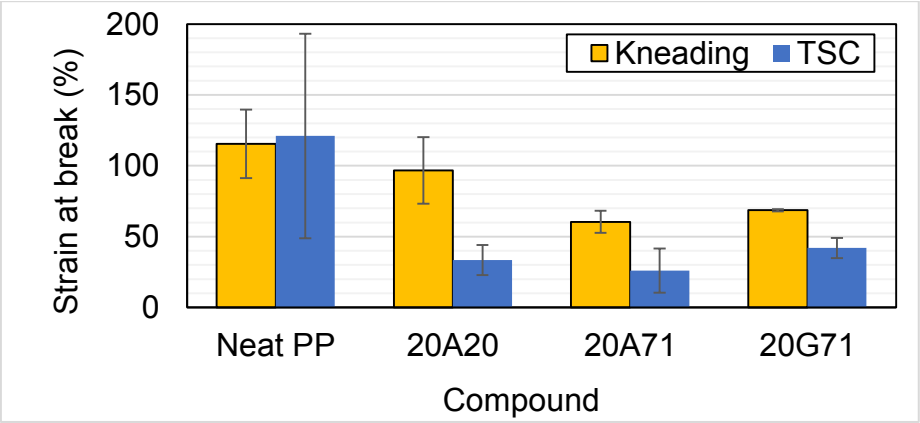

Figure 111: Strain at break of the kneaded/TSCed compounds.

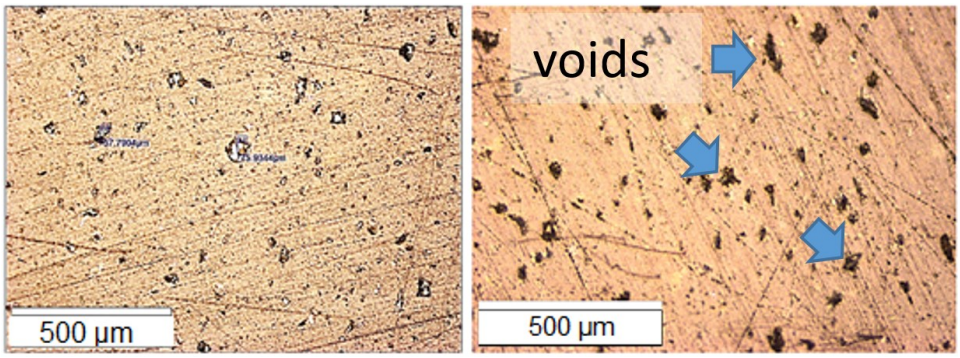

Figure 112: An optical micrograph showing BFS particle distribution in 20A71 compounds processed via kneading (left) and TSC (right).

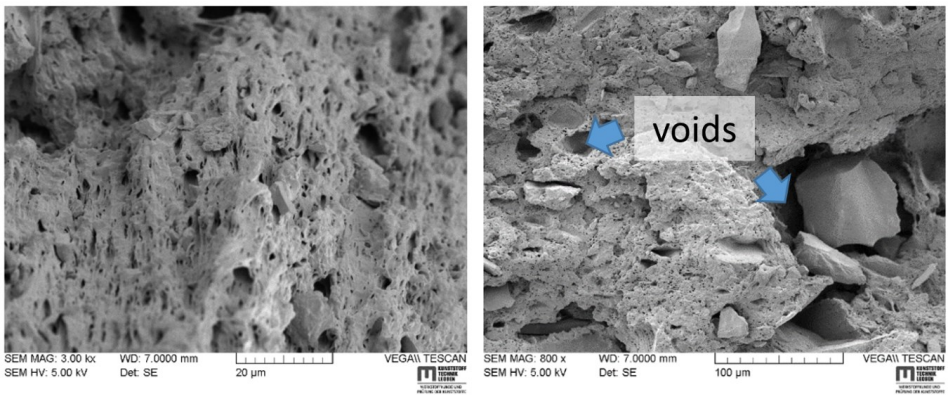

Figure 113: Fracture SEM micrograph for 20A71 compounds kneaded at 175° C, 120 rpm for 20 min (left) and (b)TSCed at 170-200° C, 200 rpm for 1 min.

4.2.3.5 Conclusions

An up-scaling comparison between the laboratory kneading and TSC processes was successfully performed for the three BFS filled PP compounds. While doubled M_d amount was exerted by TSC, it was observed that E_k and E_{TSC} were comparable. It was also shown that the η^* levels of the TSC compounds were 10 % higher than their kneaded correspondents. It was also noticed that the DOC levels of the TSC compounds were above/below their kneaded ones, depending on the compound. The tensile stiffness level of the compounds was comparable, while the ultimate strength and ductility were in favor of the kneaded compounds.

4.3 Findings of the advanced study

4.3.1 Experiment 4: Testing two coupling agents for BFS

This experiment aimed at comparing the influence of two coupling agents for BFS upon the properties of the '20A/G71' compounds. GBS and ACBS were successfully modified by each coupling agent. The modified BFS was then kneaded with PP and the un- and modified-BFS filled compounds were tested and compared.

4.3.1.1 Weight-loss TGA analyses

Thermogravimetric (TGA) analyses were carried out at LCK-MUL to insure effective silanation of both slag types and to identify their respective weight loss. Figure 114 and Figure 115 show the respective TGA curves for the unmodified GBS and ACBS as a function of temperature compared to the modified ones. The curves show that upon silanation, both GBS and ACBS experienced weight loss of 0.9 and 0.8 %, respectively. The decrease in weight % levels for the modified ACBS and GBS compared to the unmodified ones indicated that the silane successfully coated the BFS surface.

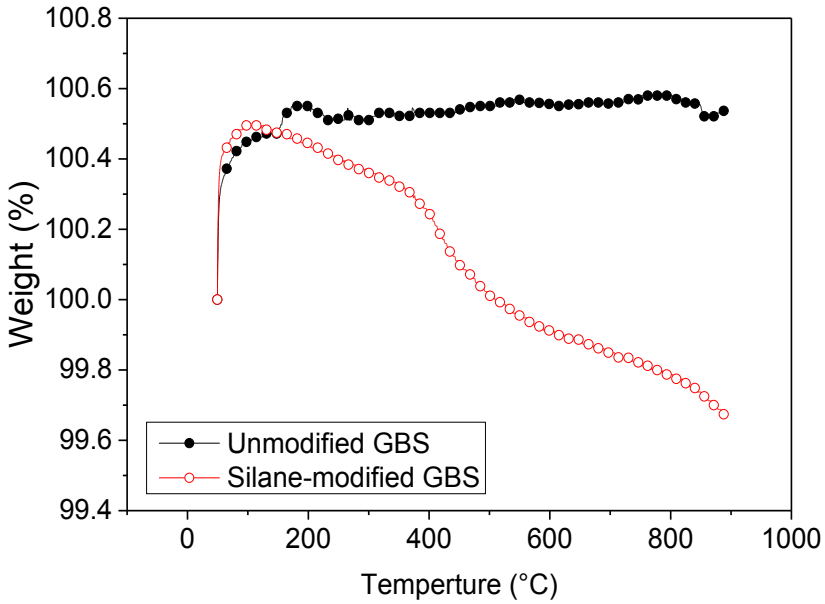

Figure 114: Thermogravimetric analyses of the MPS-modified GBS.

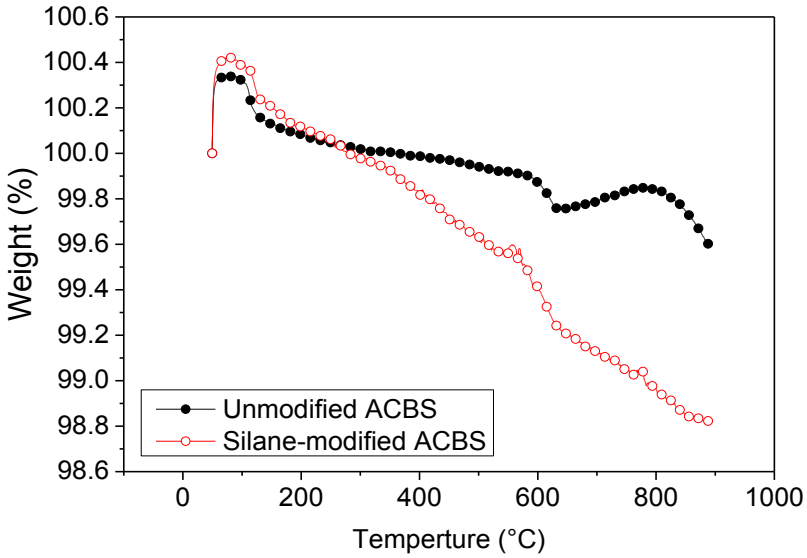

Figure 115: Thermogravimetric analyses of the MPS-modified ACBS.

4.3.1.2 Rheological behavior

The three rheological findings, η*, G´ and G´´, of the un/-modified-BFS compounds as compared to the neat PP are listed in Table 37. It can be observed from Figure 116 and Figure 117 that all compounds exhibited a shear-thinning behavior, where the rheological parameters decreased with increasing the shear rate. Figure 118 shows that modifying the BFS increased the η* of the compounds by almost 10 % regardless of the utilized coupling agent type. In addition, both modified-BFS compound types showed comparable η* levels.

Table 37: Shear rheology findings for experiment 4 (at 200 °C and 0.1 1/s).

Code	Storage modulus (Pa)	±D	Loss modulus (Pa)	±D	Complex shear viscosity (Pa.s)	±D
Neat PP	459	18	1884	69	19390	351
20A71	513	12	2102	59	21630	424
20A71-VES	593	7	2346	65	24200	435
20A71-MPS	578	5	2279	93	23515	202
20G71	528	10	2163	69	22265	502
20G71-VES	588	7	2319	72	23925	313
20G71-MPS	578	14	2267	58	23395	561

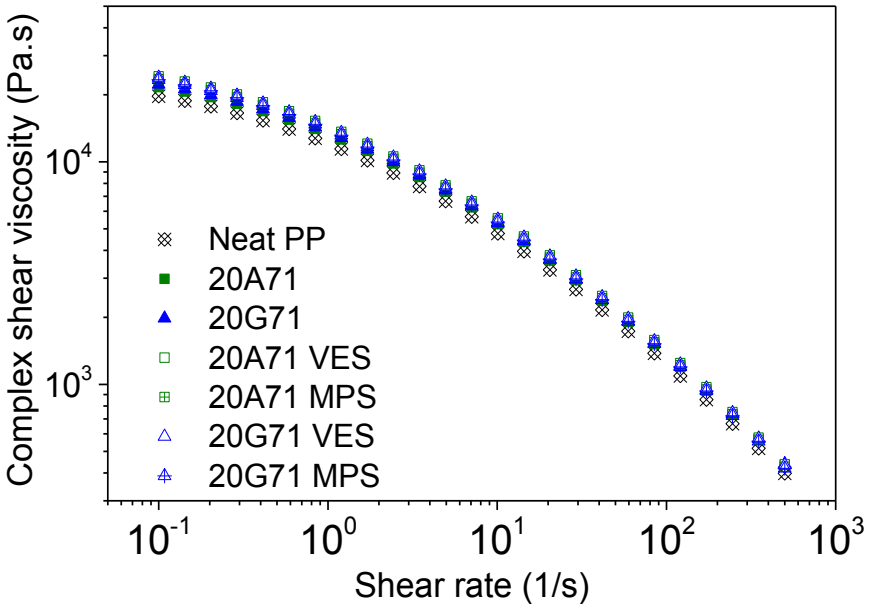

Figure 116: Complex shear viscosity of BFS filled compounds and neat PP.

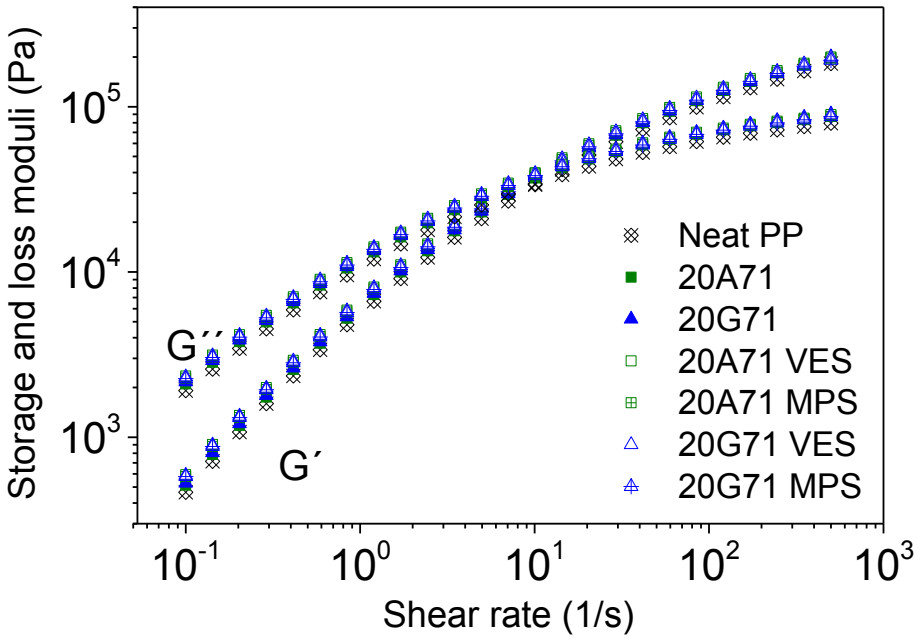

Figure 117: Storage and loss moduli of BFS compounds and neat PP.

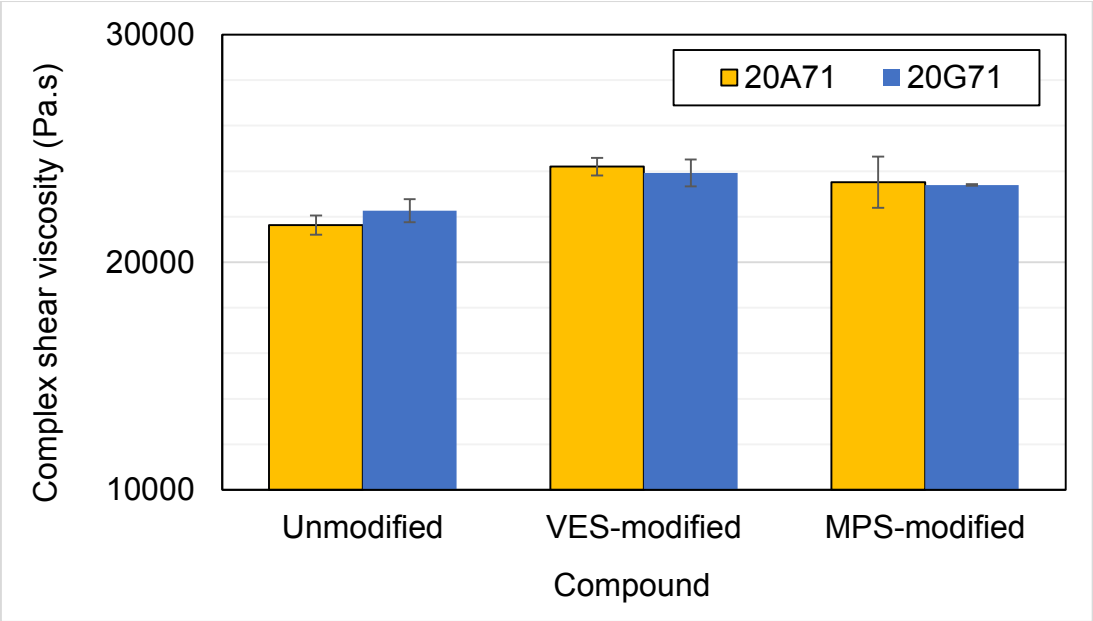

Figure 118: Complex shear viscosity of the non-/modified compounds.

4.3.1.3 Thermal behavior

The thermal findings of the unmodified- and the corresponding modified-BFS filled compounds are listed in Table 38. The data show that the values of T_c and T_m were comparable. As shown in Figure 119, it was observed that the DOC of the modified-BFS filled compounds were 10 – 30 % higher than the corresponding unmodified ones.

Table 38: Thermal findings of experiment 4.

Compound-code	First heating				Cooling				Second heating				DOC (%)	
	T_m (°C)		ΔH_m (J/g)		T_c (°C)		ΔH_c (J/g)		T_m (°C)		ΔH_m (J/g)			
Neat PP	168.2	± 0.6	94.5	± 7	118.9	±0.6	91.6	±13.40	167.6	±0.69	92.5	±11.18	44.7	± 0.7
20A71	167.8	± 0.0	68.3	±5.4	118.8	± 0.2	67.4	± 5.2	167.1	± 0.0	64.2	± 0.3	31.7	± 1.4
20A71-VES	168.2	± 0.3	83.2	± 1.8	119.3	± 0.2	81.1	± 4.9	168.0	± 0.5	82.9	± 1.7	39.7	± 0.1
20A71-MPS	168.5	± 0.1	83.2	± 1.3	118.7	± 0.4	84.0	± 5.0	168.1	± 0.2	87.6	± 4.3	40.8	± 1.5
20G71	167.9	± 0.1	73.5	± 8.3	119.1	± 0.3	73.9	± 8.1	167.5	± 0.6	73.7	± 7.4	35.2	± 0.1
20G71-VES	168.4	± 0.3	79.1	± 5.4	119.1	± 0.6	76.2	± 3.1	168.0	± 0.5	79.9	± 3.4	38.0	± 0.3
20G71-MPS	168.3	± 0.0	81.7	± 0.8	119.6	± 0.1	79.9	± 3.1	168.4	± 0.3	84.7	± 1.2	39.8	± 1.0

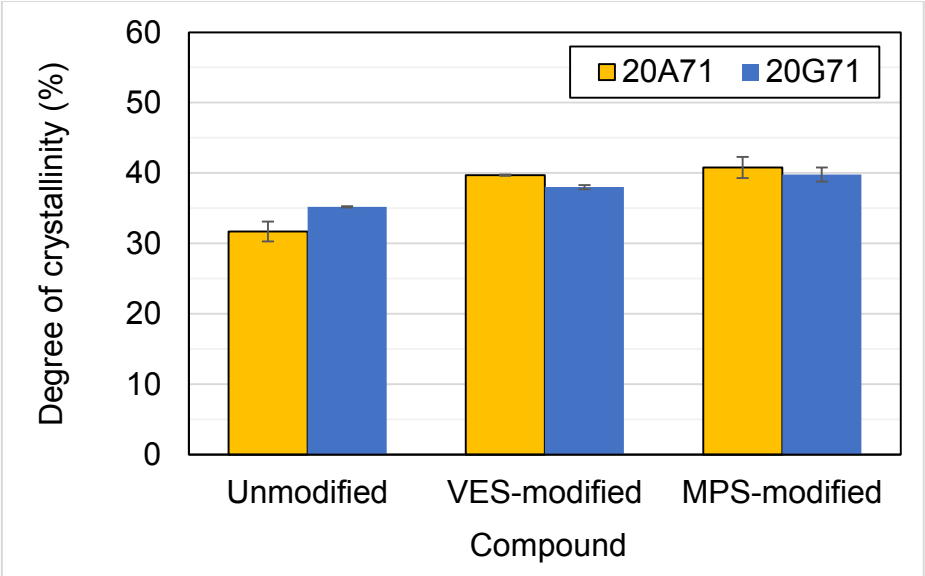

Figure 119: DOC of the un-/modified compounds.

The inspection of Figure 120 and Figure 121 revealed that modifying BFS showed a slight influence on the thermal conductivity of the compounds, where the modified-BFS compounds showed nearly 10 % higher thermal conductivity levels compared to their unmodified counterparts. It was also noticed that for the unmodified-BFS compounds, the thermal conductivity levels were almost stable over the test temperature range. That was not evident, however, for the modified-BFS ones.

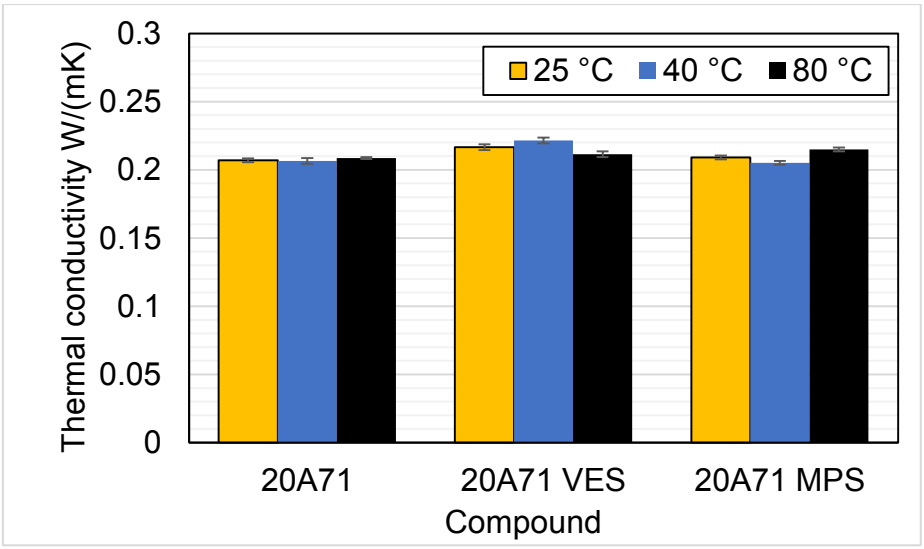

Figure 120: Thermal conductivity of the un-/modified 20A71 compound.

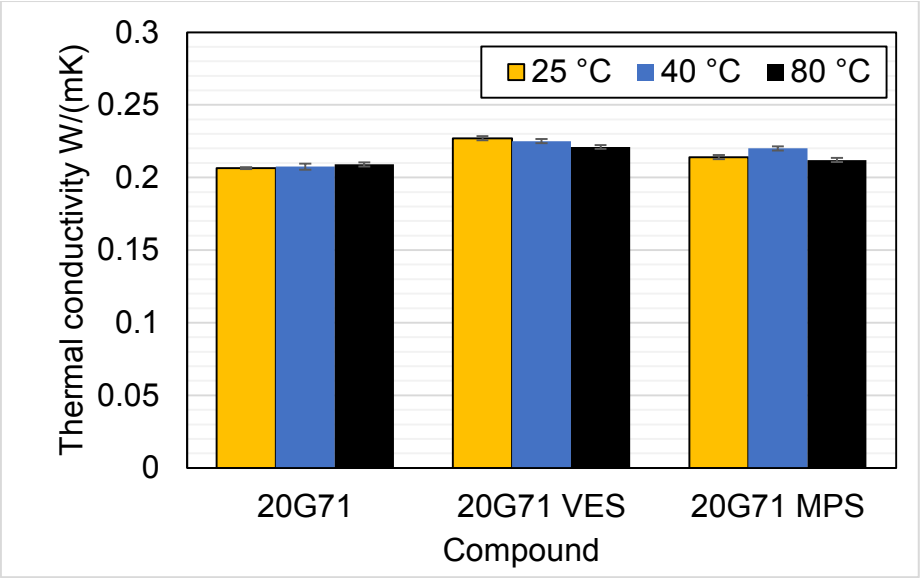

Figure 121: Thermal conductivity of the un-/modified 20G71 compounds.

4.3.1.4 Mechanical behavior

The tensile properties of the different compounds as compared to the neat PP are listed in Table 39. Figure 122 shows the stress-strain diagram for the un/-modified-BFS compounds, while Figure 123 - Figure 126 compare their tensile stiffness, ultimate strength as well as their strength- and strain at break levels. The tensile stiffness and the ultimate strength were hardly affected by BFS modification. On the other hand, the strength at break of the modified-BFS compounds increased by 30 % over the unmodified-BFS ones. The stress – strain diagram revealed that modifying the BFS filler generally improved the ductility in comparison to the neat PP and the unmodified-BFS compounds. The strain at break plots revealed that the ductility of the '20A71' compounds increased by nearly 60 – 120 % compared to the unmodified compound. That was evident, regardless of the utilized coupling agent and considering the relatively large margin of error. On the other hand, the ductility of '20G71' increased by an average of 20 % with VES but almost doubled with MPS. The impact energy plot in Figure 127 demonstrates that the toughness of the compounds was hardly influenced by the modification of BFS.

From the inspection and comparison of the mechanical findings of both MPS- and VES modified BFS compounds, it was clear that both coupling agents equally improved the

strength at break levels. However, the MPS-modified BFS increased the strain at break level of the unmodified '20G71' compound by almost 100 %, while the VES increased it by an average of 20 %. Accordingly, MPS was promoted for the next experiment.

Table 39: Mechanical findings of experiment 4.

Compound-code	Young's modulus (MPa)	±D	Ultimate strength (MPa)	±D	Ultimate strain (%)	±D	Strength at break (MPa)	±D	Strain at break (%)	
Neat PP	1487	32	23.6	1.1	4.6	0.1	18.2	0.8	94	31
20A71	1733	125	21.8	0.1	4.0	0	17.4	0.3	50	10
20A71-VES	1707	140	22.5	0.8	3.8	0.1	22.4	0.9	110	34
20A71-MPS	1683	51	21.4	0.3	3.6	0.5	21.7	0.3	106	17
20G71	1677	112	20.2	0.1	4.0	0.0	16.8	0.3	61	13
20G71-VES	1740	110	21.8	0.4	4.0	0.2	21.7	0.3	86	19
20G71-MPS	1913	366	21.7	0.5	4.0	0.5	21.7	0.5	150	11

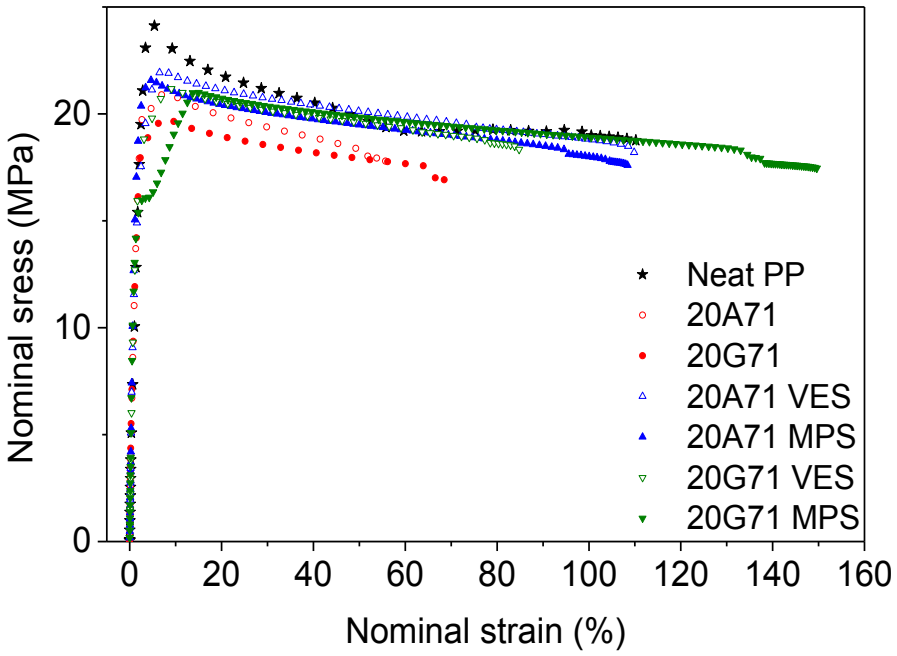

Figure 122: Stress-strain diagram of the un/-modified compounds and neat PP.

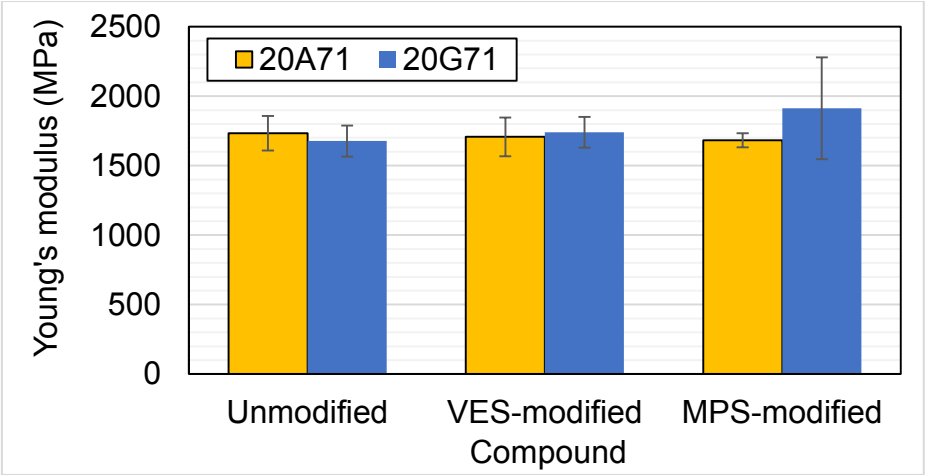

Figure 123: Tensile stiffness of the un/-modified compounds.

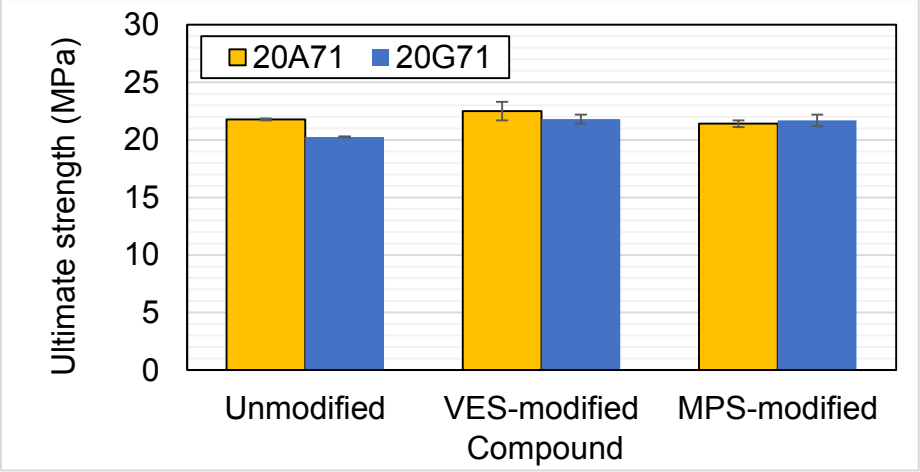

Figure 124: Ultimate strength of the un/-modified compounds.

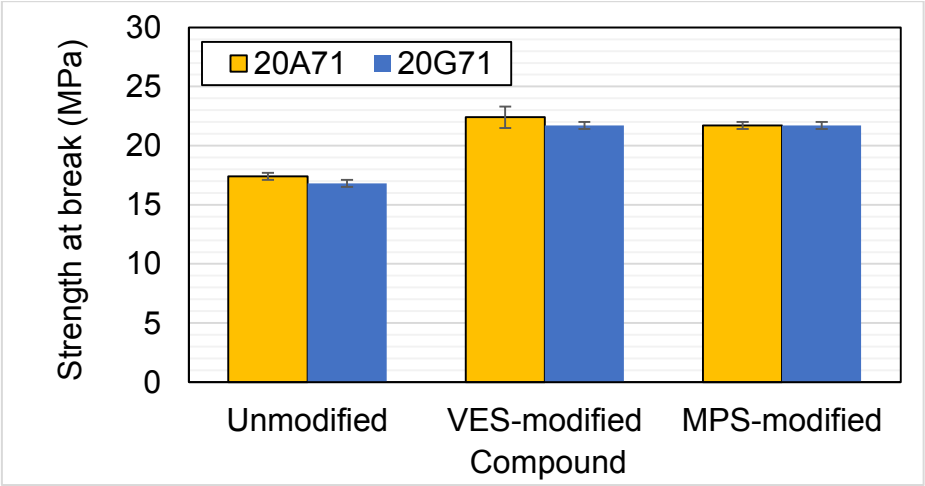

Figure 125: Strength at break levels of the un/-modified compounds.

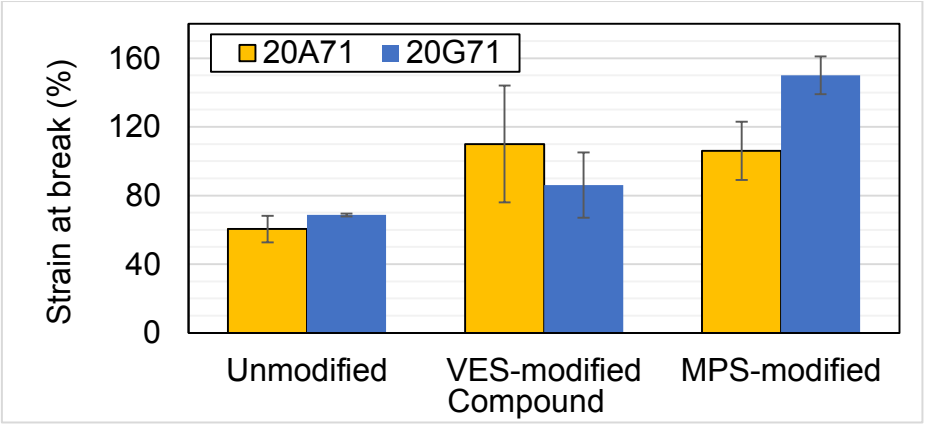

Figure 126: Strain at break levels of the un/-modified compounds.

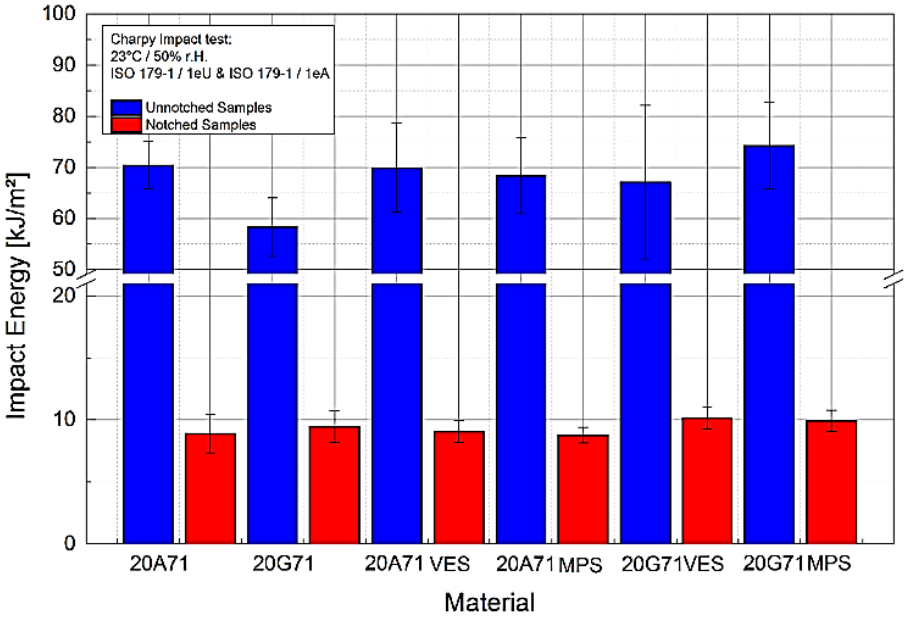

Figure 127: Impact energy levels of the un/-modified compounds at 23 °C.

To possibly explain why the compound strain increased as a result of the BFS modification, the post-tensile fracture surface of the un-/modified BFS-filled '20A71' compounds were characterized via SEM and compared in Figure 128. Except for BFS modification, both compounds shared similar processing history and filling compounds. For the unmodified-BFS compound, the ductile PP matrix was full of deep cavities resulted from the pull out of the unmodified-BFS filler from the matrix. It is implied from the number and depth of the cavities that the BFS was not adhering to the PP matrix. For the modified-BFS compound, less amount of cavities could be seen within the

vicinity of PP matrix. Even the existing cavities were observed to be shallower than those caused by the unmodified filler. It is hence suggested that the modified-BFS adhered well to the PP matrix. The improvement in the interfacial bonding was believed to be the reason behind the high ductility and strength at break levels exhibited by the modified-BFS compounds. Referring to the discussion in section 2.4.3, the coupling mechanism between the modified-BFS and PP was suggested to be similar to the reported interfacial bonding mechanisms of flyash- or nano-silica filled PP systems [110]; [87]. That is, the organofunctional groups of the silanol likely attached to the hydroxyl groups of BFS surface via covalent bonds from one end and to the functional group (R) on PP from the other. Such interfacial bonding was believed to considerably improve the compatibility between the nonpolar PP and polar BFS surfaces, reflecting higher ductility and strength at break levels.

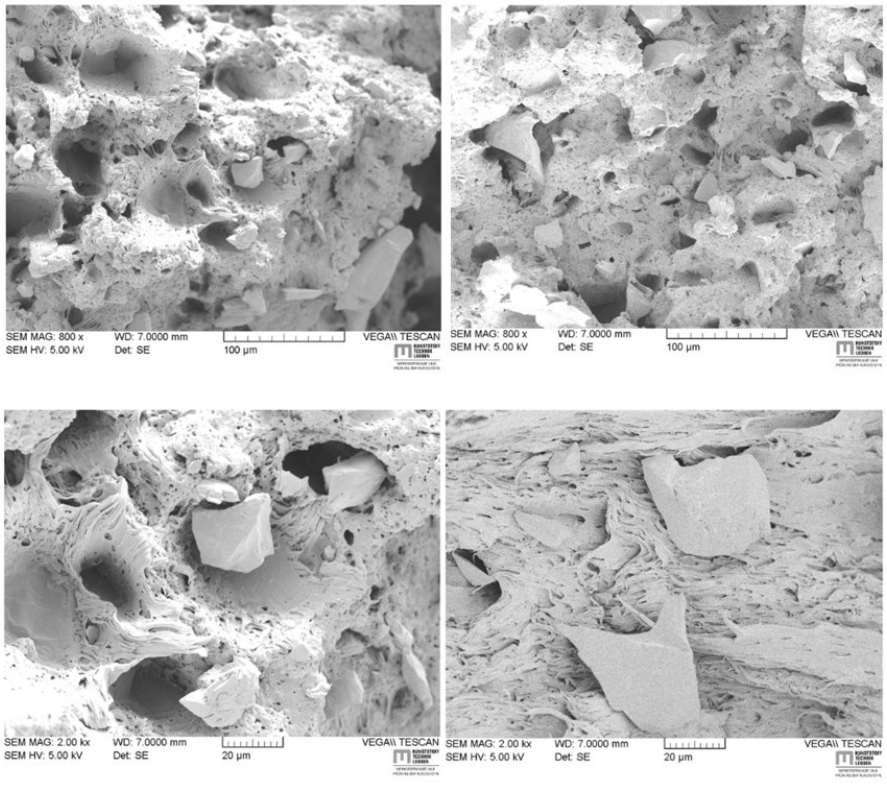

Figure 128: The interaction of unmodified BFS (left) and modified BFS (right) with the PP matrix (low- and high magnifications for up and bottom, respectively).

4.3.1.5 Conclusions

It was observed that both coupling agents equally increased the modified compounds' η^* and thermal conductivity by almost 10 % compared to the unmodified ones. The DOC of the modified compounds was also increased by 10 – 30 %. The tensile stiffness and ultimate strength levels were comparable for all compounds. However, the strength at break of the modified compounds clearly increased by 30 %. MPS type superiorly increased the ductility of the '20G71' compound by almost 100 % and was promoted for the next experiment.

4.3.2 Experiment 5: Final modified-BFS filled compounds

This is the final experiment in this research, aiming at comparing the properties of the final, industrially prepared (MPS-modified BFS, TSCed, compression-/injection molded) 20A/G71 compounds, termed '20mA/G71 TSC CM-/IM'. These final compounds were compared with the neat PP and the 'ME268AI' compound, a mineral filled PP commercial copolymer suited for automotive interior trim applications.

4.3.2.1 Rheological behavior

The rheological data of the compression- (CM) and injection molded (IM) compounds are listed in Table 40. The graphical representation is shown in Figure 129 and Figure 130. All compounds exhibited a shear-thinning behavior, where the rheological parameters decreased with increasing the shear rate.

Table 40: Shear rheology findings for experiment 5 (at 200 °C and 0.1 1/s).

Code	Storage modulus (Pa)	±D	Loss modulus (Pa)	±D	Complex shear viscosity (Pa.s)	±D
Neat PP TSC, CM	466	74	1927	298	19825	3076
20mA71 TSC,CM	526	28	2129	102	21925	1054
20mG71 TSC,CM	591	60	2349	264	24225	2708
ME268AI CM	377	50	401	286	6147	341
Neat PP TSC,IM	432	18	1806	76	18575	785
20mA71 TSC,IM	550	12	2247	54	23125	559
20mG71 TSC,IM	565	34	2310	107	23780	1131
ME268AI IM	210	12	579	31	6396	334

It was shown that the 'ME268AI' condition had the lowest G´ and G´´ levels among the group, with almost 35 and 60 % (in G´) as well as 70 and 80 % decrease (in G´´) compared to the highest levels. Whether CM or IM, the η^* of the commercial 'ME268AI' exhibited nearly 70 % lower η^* levels compared to the neat PP and the slag filled compounds, as shown in the column plot of Figure 131. The plot additionally

demonstrated that both CM and IM compounds exhibited comparable η* levels, regardless of the compound type.

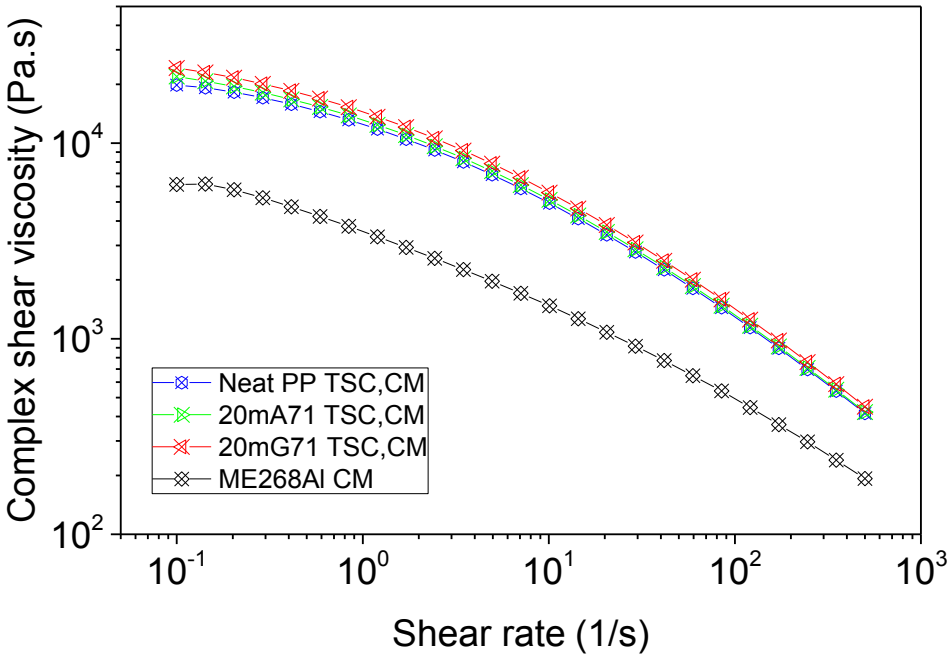

Figure 129: Complex shear viscosity of CM compounds.

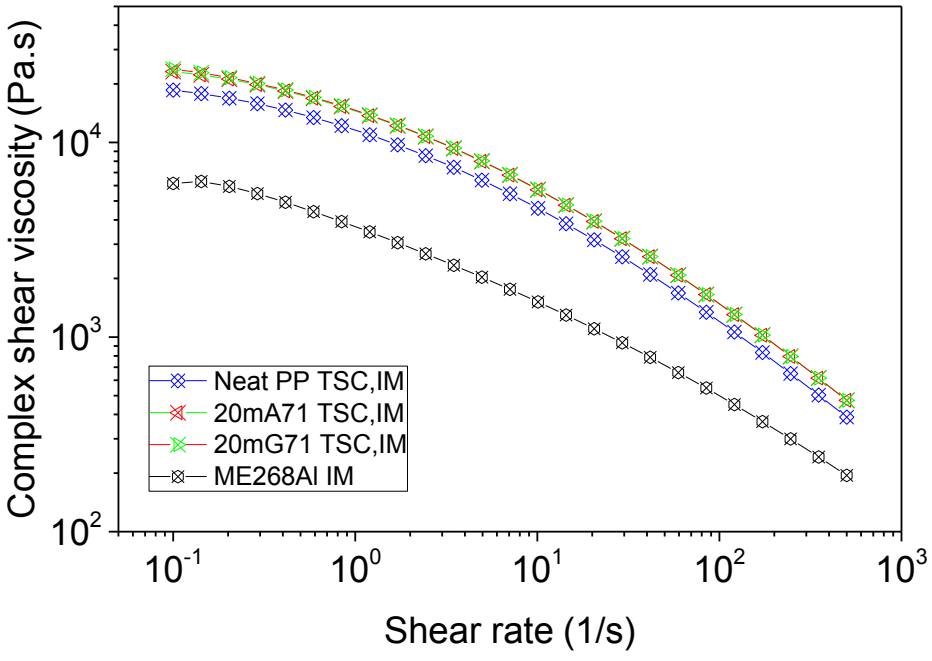

Figure 130: Complex shear viscosity values of IM compounds.

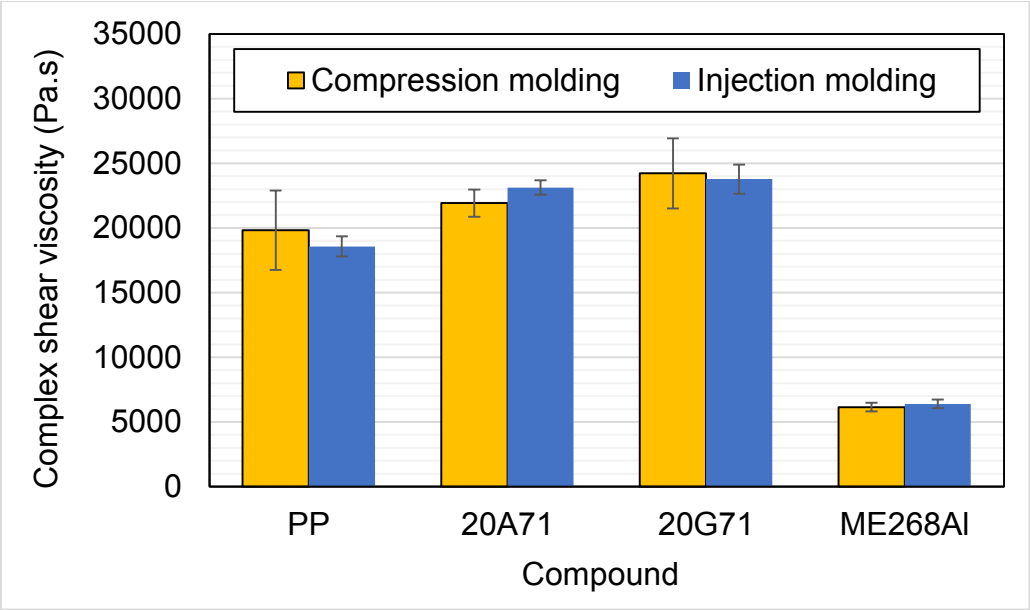

Figure 131: Complex shear viscosity of CM- and IM compounds.

4.3.2.2 Thermal conductivity

Figure 132 - Figure 135 demonstrate the influence of the molding technique, CM or IM, on the thermal conductivity of the four compounds. Figure 132 shows that the thermal conductivity for the neat PP IM compound was nearly 10 % less than its corresponding CM. The '20mA71', Figure 133, decreased by almost the same amount. Unlike the neat PP, an increasing linear pattern in the thermal conductivity level was observed toward the 80 °C setting of the IM compound. For the '20mG71' compound, Figure 134, the pattern took place for CM compound instead, while no pattern showed for the 'ME268AI' compound. It was seen from the four plots that the influence of the molding technique was apparent in only two compounds: 'neat PP' and '20mA71', where the thermal conductivity of the IM compounds decreased by nearly 10 % as compared to CM. The thermal conductivity levels of the CM and IM compounds at 25 °C is shown in Figure 136. The increase or decrease of the thermal conductivity for the IM compounds compared to CM ones followed different patterns, depending on the compound. That is, the thermal conductivity of the IM variants of both neat PP and ACBS filled compound decreased by 10 – 20 % compared to the CM. A contrary increase of almost 5 %, however, was noticed for the GBS filled compound. For the 'ME268AI', CM and IM variants showed comparable levels.

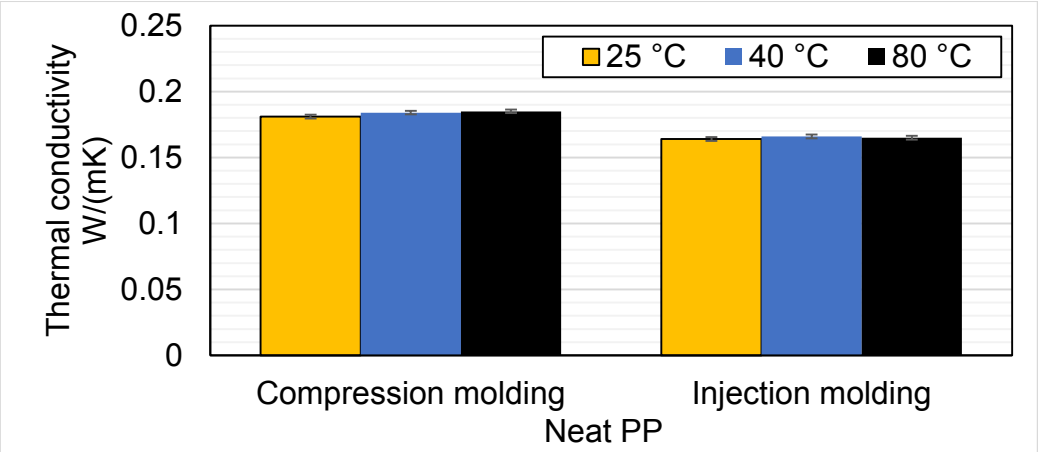

Figure 132: Thermal conductivity of the neat PP TSC, CM- and IM compound.

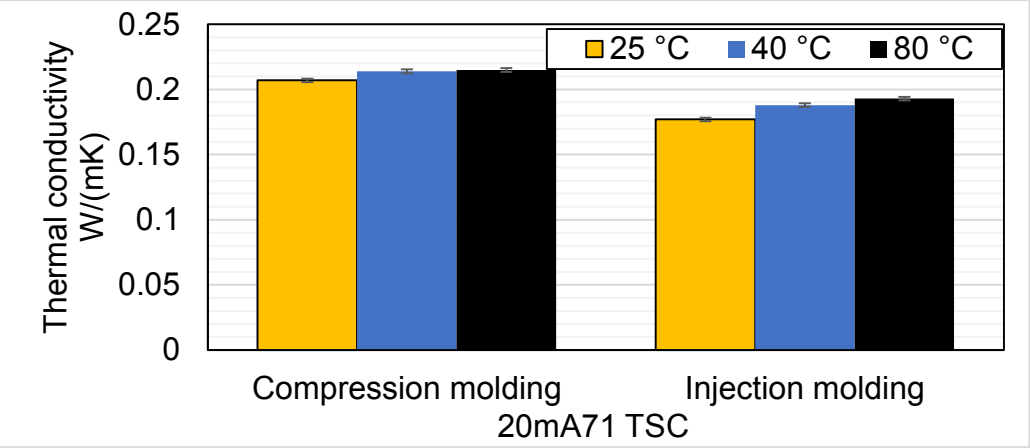

Figure 133: Thermal conductivity of the 20mA71 TSC, CM- and IM compound.

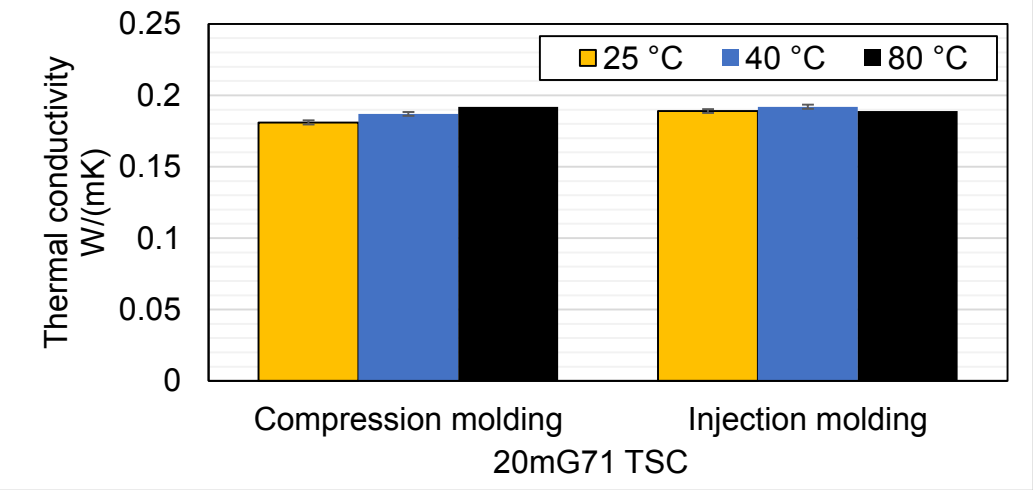

Figure 134: Thermal conductivity of the 20mG71 TSC, CM- and IM compound.

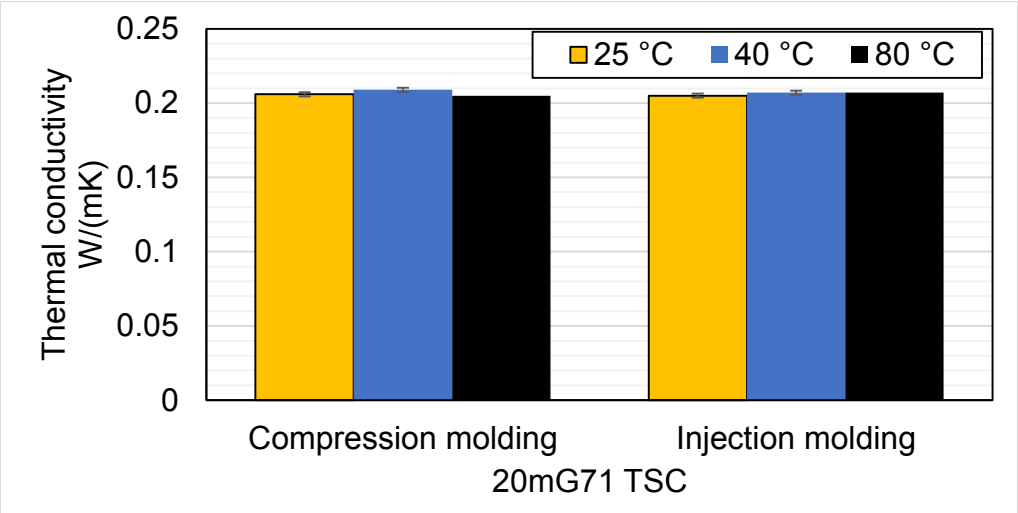

Figure 135: Thermal conductivity of the ME268AI TSC, CM- and IM compound.

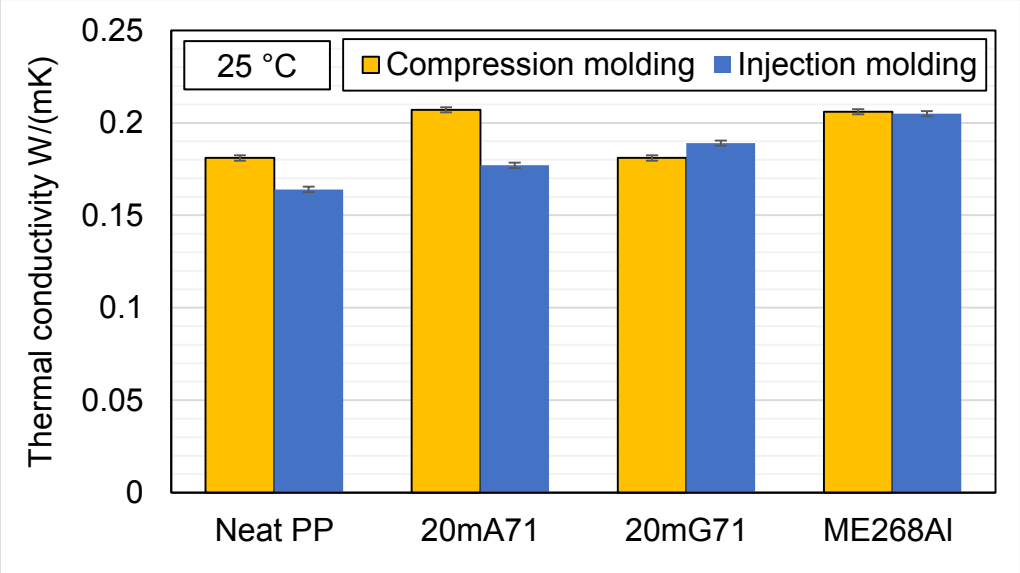

Figure 136: Thermal conductivity of the compounds at 25 °C.

4.3.2.3 Mechanical behavior

The mechanical findings of the compounds are demonstrated in Table 41. The stress-strain diagrams of both CM and IM compounds are demonstrated in Figure 137 and Figure 138. The two diagrams compared to scale the strength and ductility levels of respective CM and IM compounds. The levels were also illustrated in subsequent column plots.

Table 41: Mechanical findings of experiment 5.

Compound code	Young's modulus (MPa)	±D	Ultimate strength (MPa)	±D	Ultimate strain (%)	±D	Strength at break (MPa)	±D	Strain at break (%)	
Neat PP TSC, CM	1235	21	23.0	0.0	6.1	0.8	9.5	8.2	121	72
20mA71 TSC,CM	1655	35	20.8	1.3	4.3	0.2	9.2	7.9	28	8
20mG71 TSC,CM	1610	42	19.8	0.5	5.2	0.8	9.0	7.8	50	17
ME268AI CM	1535	64	15.9	0.3	2.6	0.0	7.3	6.3	2	1
Neat PP TSC, CM	1257	6	25.9	0.1	7.6	0.2	6.5	0.3	62.5	5.8
20mA71 TSC,IM	1503	6	22.7	0.1	6.4	0.1	18.6	0.3	89.8	7.7
20mG71 TSC,IM	1487	21	21.8	0.1	6.8	0.4	20.5	0.2	364.4	2.2
ME268AI IM	2133	15	24.6	0.1	5.1	0.2	13.2	1.2	21.1	5.2

Figure 139 demonstrates the tensile stiffness of both groups. Each compound displayed a unique tensile stiffness pattern. For the neat PP, the tensile stiffness of both CM and IM compounds was comparable. For the BFS-filled compounds, the tensile stiffness of the IM group was 10 % lower than its corresponding CM. The trend was different for the 'ME268AI', where the IM compound experienced an increase of 50 % over the CM one. It is evident that the improved ductility of the slag filled IM compounds came at the cost of this 10 % decrease in their tensile stiffness. For the 'ME268AI', the increase in stiffness after injection molding was surprising and difficult to explain, as no information was provided from the company Borealis GmbH regarding the type of mineral filler(s) or the copolymer of the compound. In Figure 140, it was observed that the ultimate strength levels of the neat PP and the slag filled IM compounds were consistently 10 % higher than their corresponding CM. The increase in the commercial compound, however, was almost 50 %. This pattern was almost replicated for the ultimate strain, Figure 141. The only difference is that, for the first three IM compounds the increase was almost 40 instead of 10 %. In Figure 142, the strength at break of the neat PP IM decreased by 40 %. The other three compounds, in contrast, showed over 100 % increase for the IM compounds, as compared to CM ones. Figure 143, shows that the ductility of the '20mG71' compound was superior to all other compounds with an increase of about 600 % above its twin compound. The

ductility increased by 220% for the ‘20mA71’ compound. Figure 144 and Figure 145 display the impact energy of the un-/notched compounds at 23 and -30 °C, respectively. The toughness of the BFS compounds were at least comparable with ‘ME268AI’.

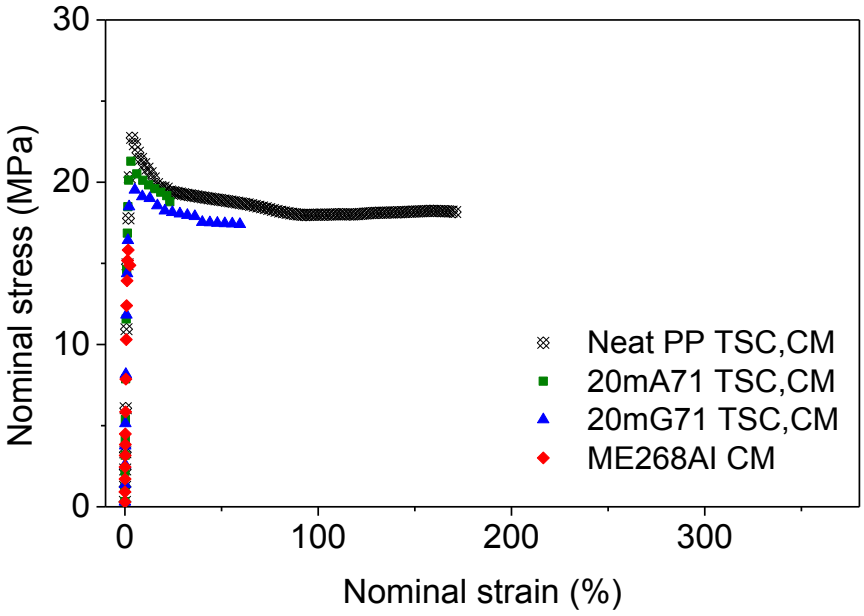

Figure 137: Stress-strain diagram of the CM compounds.

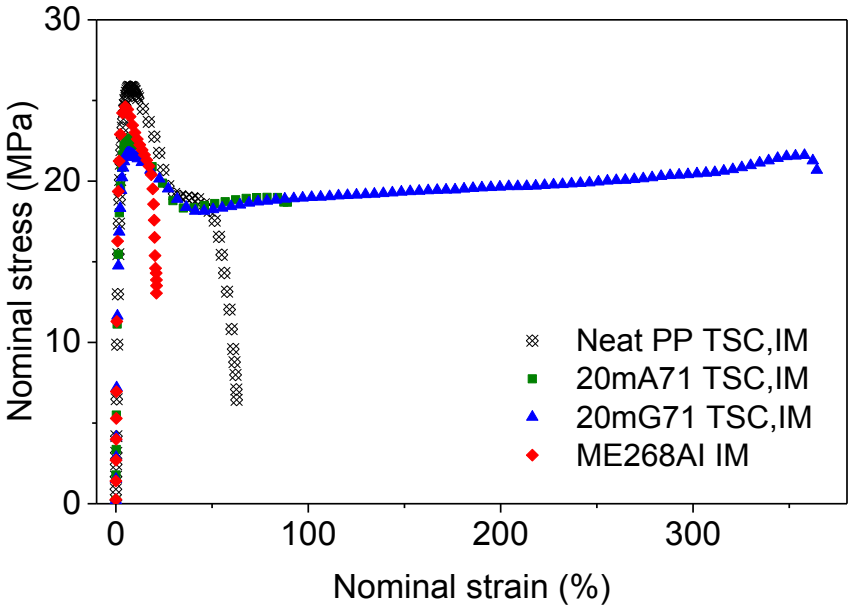

Figure 138: Stress-strain diagram of the IM compounds.

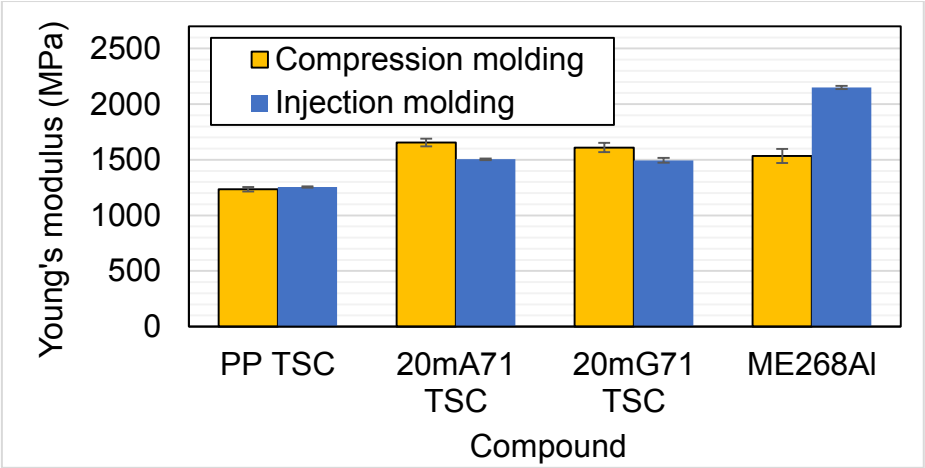

Figure 139: Young's modulus of the CM- and IM compounds.

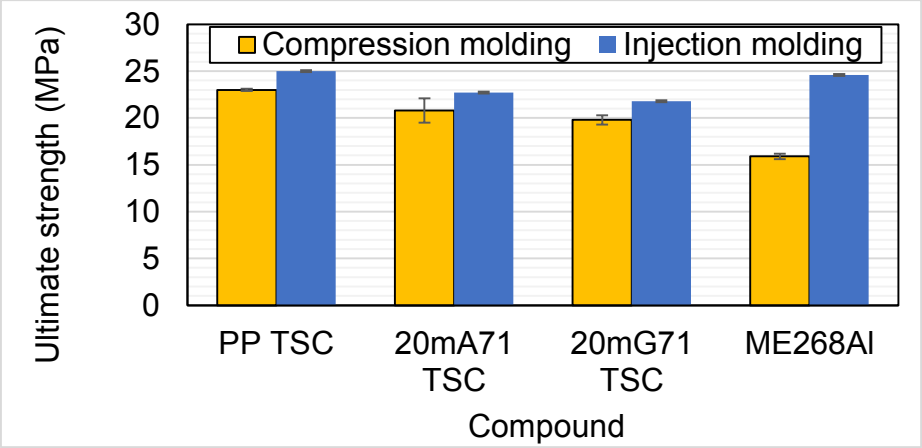

Figure 140: Ultimate strength of the CM- and IM compounds.

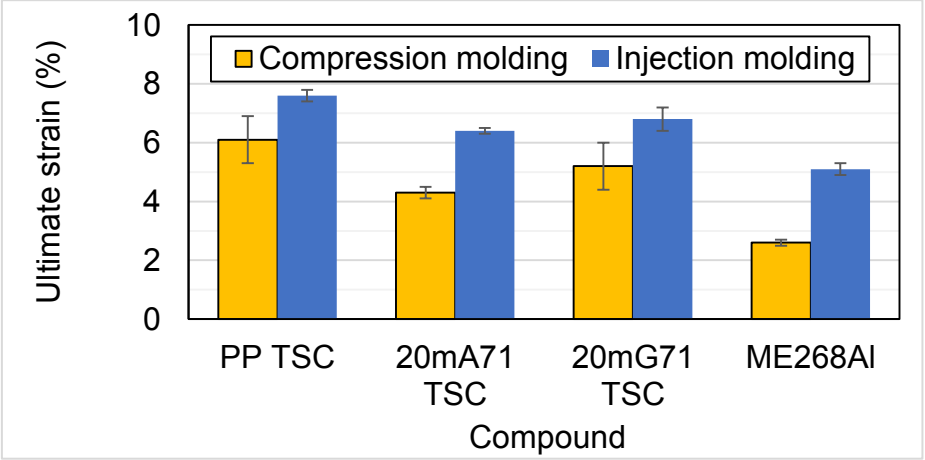

Figure 141: Ultimate strain of the CM- and IM compounds.

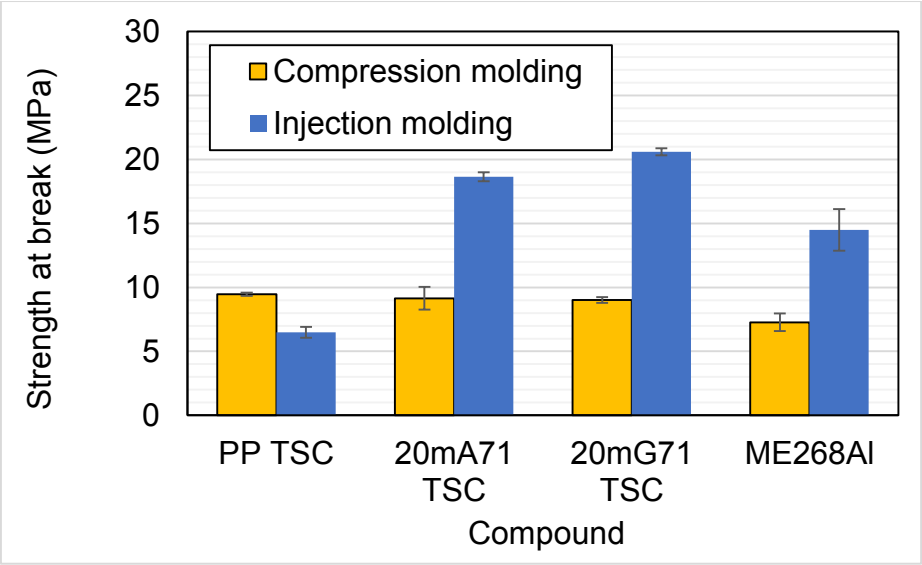

Figure 142: Strength at break of the CM- and IM compounds.

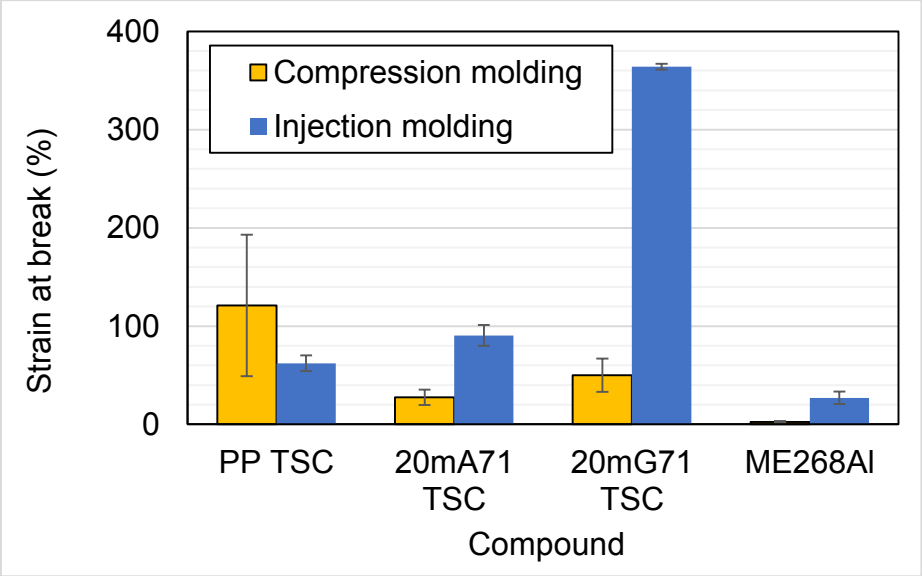

Figure 143: Strain at break of the CM- and IM compounds.

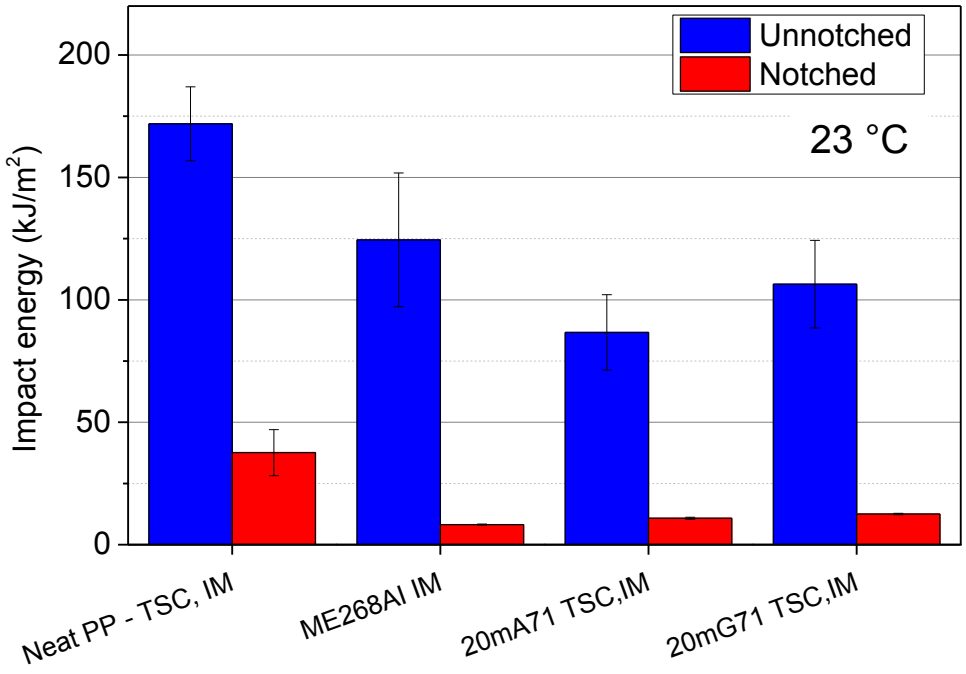

Figure 144: Impact energy of the IM compounds at 23 °C.

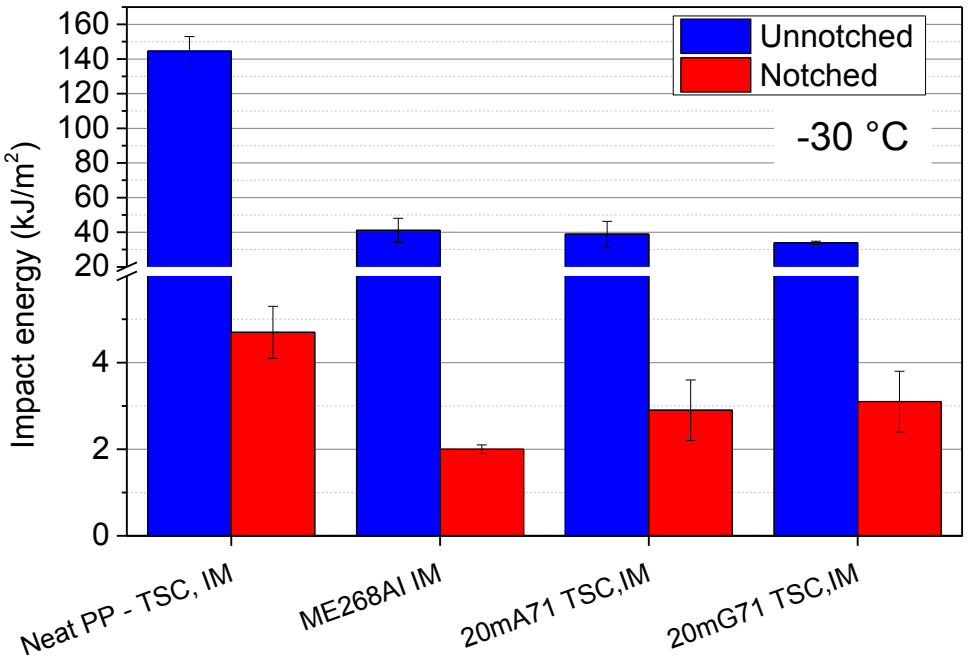

Figure 145: Impact energy of the IM compounds at -30 °C.

4.3.2.4 Conclusions

The η^* levels of the CM and twin IM compounds were comparable. It was noted that the 'ME268Ai' compound had almost 70 % lower η^* compared to the neat PP and BFS filled compounds. It was also noticed that the thermal conductivity of the IM neat PP and ACBS filled compounds decreased by 10 % compared to their CM twins. For the BFS compounds, the IM compound showed 10 % higher levels of stiffness than the CM. For the 'ME268AI', the difference increased to 50 %. The strength at break and ductility levels of the IM compounds were approximately 100 – 200 % higher than the corresponding CM. For the ductility, the '20mG71 TSC,IM' achieved the highest strain at break, nearly 500 – 800% higher than the other compounds.

4.4 General compounds comparisons

This section compares selected rheological, thermal and mechanical properties of the '20G71' and '20A71' variant compounds produced throughout this study. The variation of each compound was based upon three parameters: (1) the compounding equipment used, (2) whether the slag is modified or not and (3) the type of molding: CM or IM. The reader may kindly refer to section 3.6.1 for the terminology explanation.

4.4.1 Rheological behavior

A column plot of all '20A71' and '20G71' variants is demonstrated in Figure 146. It was shown that changing the mixing technique of the unmodified-BFS filled compounds from kneading to TSC resulted into almost 15 % decrease in η^*. BFS modification was observed to hardly influence the η^* levels for the kneaded compounds. However, the BFS modification influence was more apparent in TSC compounds, where the η^* increased by a minimum of 10 %. The choice of the consolidation technique, CM or IM, hardly influenced the η^* level.

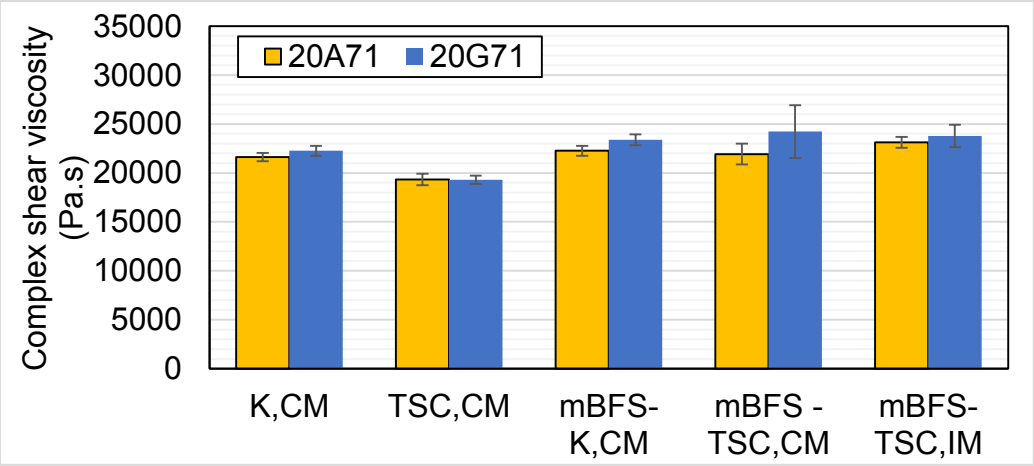

Figure 146: Complex shear viscosity of the 20A71 and 20G71 variant compounds.

4.4.2 Thermal conductivity

Figure 147 shows the thermal conductivity levels for all '20A/G71' compound variants. The graphs indicate that the thermal conductivity levels of all variants were almost comparable. It was also noticed that modifying the BFS filler in the 'K,CM' setting hardly

affected the thermal conductivity. The disparity of the thermal conductivity between the ACBS and GBS compounds was only evident in the '20A/G71 TSC,CM/IM' compounds, where the ACBS compound showed 10 % higher thermal conductivity than the GBS one at the CM group. The trend was reversed, however, at the IM group. For the last two column couples, the disparity of the thermal conductivity between the ACBS- and GBS-filled compounds was nearly 40 %. It was also noticed that the variation of the molding technique had a notable influence on the thermal conductivity. For ACBS compounds, the IM technique corresponded to a lower thermal conductivity level compared to CM, while the opposite was true for GBS compounds.

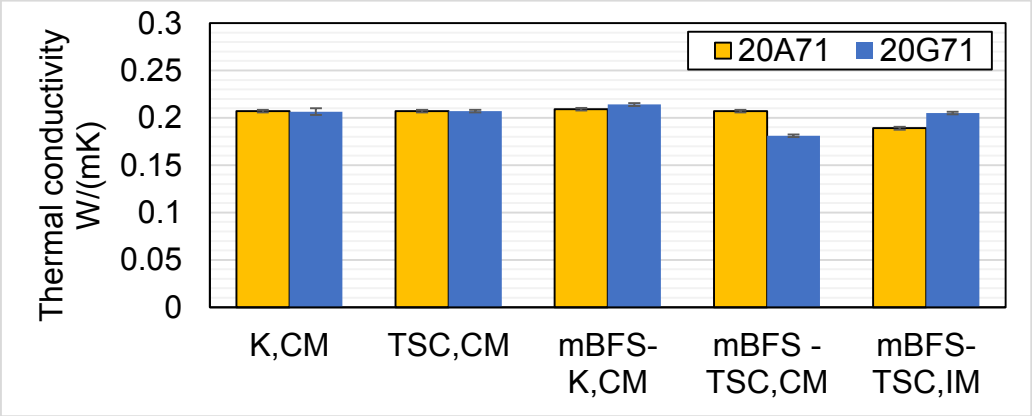

Figure 147: Thermal conductivity values of the 20A71 and 20G71 compounds.

4.4.3 Mechanical behavior

The tensile stiffness levels of the variants are compared in Figure 148. No significant disparity was noticed among the compounds. Recalling the findings of the earlier experiments, it can be concluded that the tensile stiffness was more dependent on the filler loading than on the processing parameters or filler modification. For the ultimate strength, Figure 149, the influence of BFS modification was evident among the un/-modified 'TSC, CM' variants in the second and fourth groups, but the pattern was not evident in the 'K, CM' compounds. It is likely that the MPS exhibited better functionality during TSC than kneading, which allowed the slag filler to better adhere to the PP matrix and hence the ultimate strength was enhanced. For the strain at break, Figure 150, It was noticed that the modification of the BFS was pronounced in the third and fifth group, with surprising increase in ductility for GBS compound in the latter.

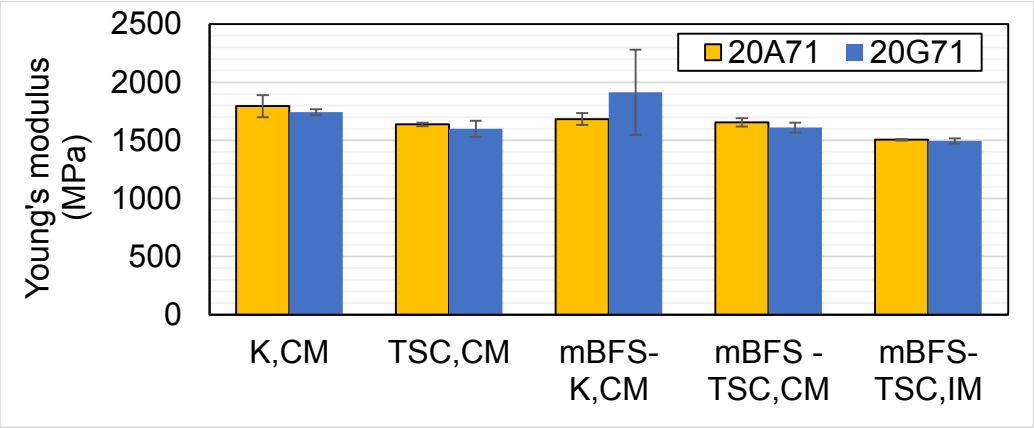

Figure 148: Young's modulus of the 20A71 and 20G71 variant compounds.

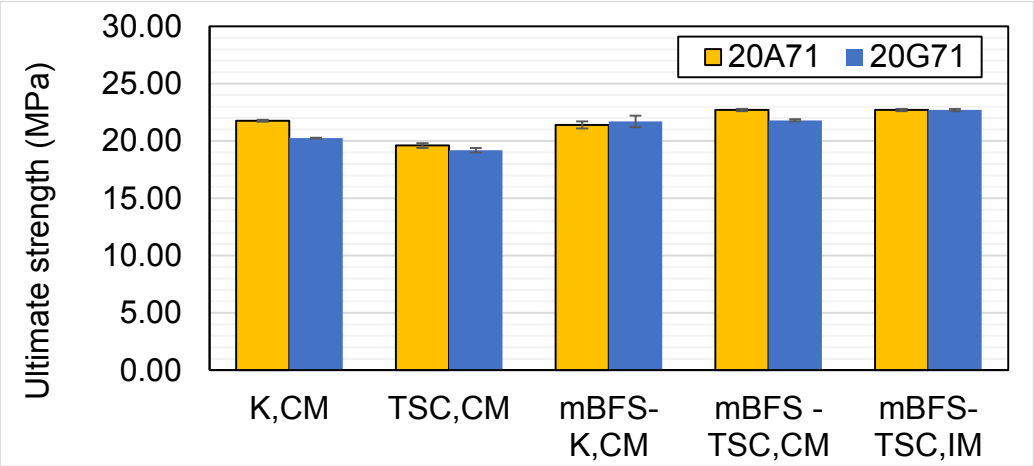

Figure 149: Ultimate strength of the 20A71 and 20G71 variant compounds.

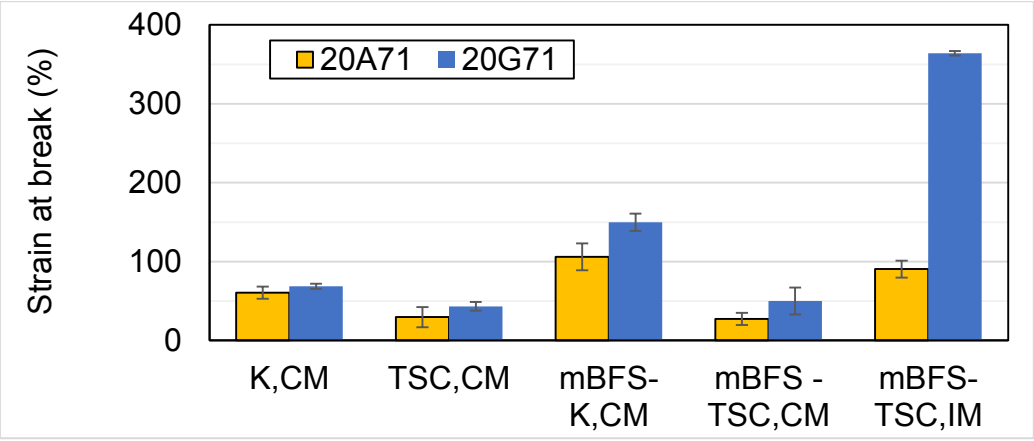

Figure 150: Strain at break of the 20A71 and 20G71 variant compounds.

5 Findings of the ‘Carbon footprint screening’ study

This CFS aimed at comparing the generated CO_2 amount during the production of 1 t of two technical compounds PP - BFS and PP – Limestone, which was handful in reflecting the ecological meaningfulness of BFS as a filler. The presented results were recommended to be a starting point for further LCA activities in this topic. These analyses were compiled and is quoted in this context from the report accomplished by Mr. DDI Matthias Katschnig, LCA-specialist, LKV-MUL [41].

5.1 Evaluation method

Carbon Footprint is applied as single issue evaluation according to ISO 14040ff (IPCC GWP 100a = „Carbon Footprint“, unit: kg CO_2 eq.). This method is selected based on the requirements transparency and comparability in the market.

5.2 Modelling with SimaPro®

SimaPro is a tool for the development of LCA and was developed by PRé Consultants in the Netherlands. In order to analyze and compare a product, raw materials, production, use and disposal are entered as inventory data. The individual environmental impact of the product life-cycle can hence be calculated by SimaPro (impact assessment).

5.3 Basic Model Data

- Impact assessment method: IPCC GWP 100a (unit: t CO_2 eq).
- Function: Supply of 1 t compound (granules) for automotive applications.
- Functional unit: 1 t compound.
- Product 1: 1 t PP/BFS with 20 wt.-% BFS.
- Product 2: 1 t PP/limestone with 20w% Limestone.
- System boundaries: cradle to gate.
- Secondary date: Ecoinvent v3 [70], [102] and additional sources (cp. 2.5).
- Software: SimaPro v8.2 [80], [24].
- Detail level: internal screening.

- Internal peer review: Ass.Prof. Dipl.-Ing. Dr.mont Thomas Lucyshyn.

5.4 System boundaries

The limits of the system were specificed according to the Cradle to Gate principle. It is denoted from the raw material source to the end of the granulate production process (provision of 1 t material). No transport processes were taken into account for the current analyses. The preparation of slag for compounding was not taken into account as well.

An important consideration for the slag production process was the consideration of BFS as a possible plastic filler rather than a waste (by-product scenario). An open-loop recycling approach was hence used in this life cycle assessment [44]. The allocation of the goods and debits between the steel production and the by-product slag were defined by two allocation rules to identify basic tendencies:

- 50/50 rule („50/50“ allocation) – 50,50 scenario
    - Systems are coupled according to the 50/50 method,
- Cut-off rules -
    - Cut-off for steel (“worst for slag” allocation): All CO_2-emissions, that are causally connected to bring slag into existence, are assigned to slag.
    - Cut-off for slag (allocation “best for slag” allocation): All CO_2-emissions, that are causally connected to bring slag into existence, are assigned to steel. Reason is that steel production would take place anyway irrespective of the use of slag as a filler. Thus slag doesn’t need to be solely produced (by-product) in contrast to limestone (main product).

5.5 Data

- Slag: [10]; [42].
- Limestone: [90]; [71]; [72].
- PP [79].
- Compounding: [106]; [70]
- Time interval: 2000 - 2017.

- Region: AT, EU-Ø.

5.6 Findings

Figure 151 shows a comparison between the 1-t generated CO_2 of limestone filled PP to the three BFS compound scenarios corresponding to “50/50” and “cut-off” allocations. The main result impact is the difference of CO_2 eq. content of limestone (75 kg CO2 eq. per t) and slag (450 kg CO_2 eq. per t). Only in the scenario „best for slag“, where all emissions are assigned to the main product steel, PP-BFS (1.9 t CO_2 eq.) is slightly superior to PP/Limestone (1.915 t CO_2 eq.). Drawback here is the lack of CO_2 data with respect to the preparation of slag for compounding. That is, the modification of BFS for compounding is expected to emit an additional amount of CO_2 to the atmosphere, which was already taken into consideration for the PP-limestone compound. This should be taken into account for future studies. The other two scenarios,’50,50’ and ‘worst for slag’, showed higher emitted CO_2 amount than the lime-stone filled PP compound.

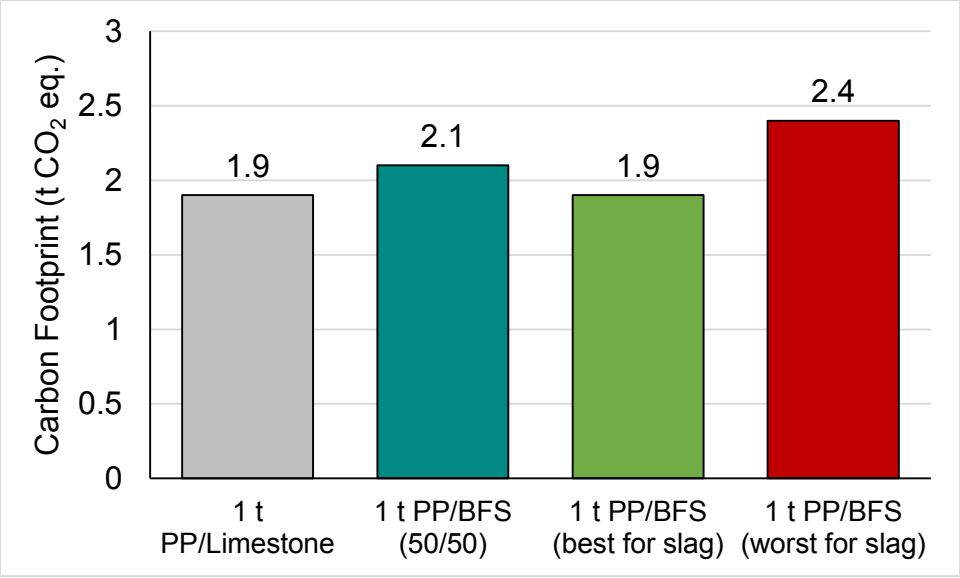

Figure 151: Carbon Footprint for the different BFS filled compound scenarios as compared to Limestone filled compound.

6 Conclusions and future prospects

The findings of this dissertation showed the influence of un-/modified BFS on the properties of PP, compared it to a commercial alternative for a specific industrial application and investigated its carbon footprint. The findings of this study with respect to each category of properties were as follows:

Rheological

Kneading and compression molding of different distributions and loadings of unmodified ACBS and GBS types with PP showed a general shear thinning behavior for all compounds. Comparing with the neat PP, it was observed that η^* proportionally increased with the BFS loading up to an increase 35 % at 30 wt.-% loading, while the BFS distribution or type hardly affected the η^*. It was also observed that the <20 µm group recorded the lowest η^* among the three distributions. In addition, the variation of the kneading process parameters, speed and duration, hardly influenced the η^*. Comparing both kneading and TSC processes showed that the η^* levels corresponding to the TSC compounds were consistently 10 % higher than the kneaded ones. BFS modification by either MPS or VES coupling agents increased the η^* by almost 10 %. For the final compounds, the η^* levels of both CM and corresponding IM counterparts were comparable. Comparing the final BFS – PP compounds with the 'ME268AI' showed that the latter was almost 70 % lower in η^*.

The comparison of all '20A/G71' variants showed that η^* was influenced by (1) the change of the compounding technique from kneading to TSC and (2) the modification of BFS, but only in TSC compounds. For the first case the η^* decreased by 15 %, while an increase of 10 % was rather observed for the second.

Thermal

Compared to the rheological pattern, it was observed that the DOC recorded a linear decrease, compared to the linear increase in η^*, with increasing the BFS loading; the DOC was likewise almost independent of the BFS distribution or type. In addition, incorporating 20 wt.-% of the unmodified-BFS increased the thermal conductivity of PP

by nearly 40 %. Similar to the rheological properties, the thermal properties, i.e. T_c, T_m and DOC, were hardly affected by the variation of the kneading speed and duration. Upon comparing laboratory kneading and TSC techniques, it was noticed that the DOC levels of the TSCed compounds were above or below their kneaded twins depending on the compound type. On the other hand, the variation of the compounding technique did not affect the thermal conductivity. Considering the VES- and corresponding MPS-modified BFS filled compounds, it was observed that the DOC levels of the modified compounds increased by 10 – 30 % compared to the unmodified ones, irrespective of the utilized coupling agent. The thermal conductivity of the modified compounds also increased by 10 % compared to the unmodified ones. For the final compounds, it was noticed that the thermal conductivity of the injection molded neat PP and ACBS filled compounds decreased by 10 % compared to their compression molded twins.

The comparison of the '20A/G71' variants showed comparable thermal conductivity levels. Only for the final compounds, a 10 % difference among the thermal conductivity values between ACBS- and corresponding GBS compounds was evident.

Mechanical

Following the same pattern of η^*, the tensile stiffness increased linearly with the BFS loading up to 15 wt.-% at 30 wt.-% loading; however, almost no influence from BFS type or distribution was recorded. The ultimate strength seemed to decrease, however, with increasing the filler loading except for the <20 µm compounds, where clear disparity was observed among the different loadings. At only 10 wt.-% loading, the ultimate strength showed a linear decreasing trend with the distribution. For the ductility, only at <20 µm the strain at break was comparable to the neat PP, but with wide margins of error resulting from premature failure of the compounds. For the influence of the kneading speed and duration, the tensile stiffness and ultimate strength levels were all comparable, while the strength at break showed different trends depending on the kneading speed settings. Likewise, the tensile stiffness levels of the kneaded and TSCed compounds were comparable, while the ultimate strength and ductility were in favor of the kneaded ones. For the influence of VES and MPS coupling agents, the strength at break of the modified compounds increased by 30 %. However, the MPS type superiorly increased the ductility of the '20G71' compound by

almost 100 % and was promoted for the next experiment. For the final compounds, the tensile stiffness levels of the injection molded modified-BFS - PP and 'ME268AI' compounds were 10 and 50 % higher than their compression molded twins. In addition, the strength at break and ductility levels of the injection molded compounds were 100 – 200 % higher than the compression molded ones. For the ductility, the '20mG71 TSC,IM' compound achieved the highest strain at break level among the group.

The tensile stiffness levels of the '20A/G71' variants were generally comparable. For the ultimate strength, the influence of BFS modification was only observable in the 'TSC, CM' group. For the strain at break, the '20mG71 TSC,IM' compound showed the highest ductility among all.

Process parameters

For the influence of the kneading process parameters on the M_d and E_k, it was witnessed that both factors were proportional to the kneading speed. E_k was also shown to be proportional to the kneading duration. The calculation of both E_k and E_{TSC} indicated that both factors were comparable.

Carbon footprint screening

For the scenario „best for slag", where all emissions were assigned to the main product steel, 1 t of BFS filled PP compound generated a little less CO_2 than the limestone filled PP compound. It is important to emphasize that while limestone was modified and compounding-ready, the BFS was not. In fact, the modification process for BFS is expected to emit extra CO_2 into the atmosphere, which might move the BFS toward the '50,50' scenario.

Future prospects

The investigation of a novel system like PP - BFS could be further elaborated in various directions based on the knowledge provided by this dissertation. Examples of potential investigation areas include but are not limited to:

- Application of BFS as a filler in other thermoplastic systems (PE, PC, etc.)
- Influence of different particle sizes of BFS on PP

- Application of nano-sized BFS
- The influence of other slag types such as BOS.
- Studying other coupling agents for BFS
- Further CFS analyses, where the emitted CO_2 amount corresponding to the modification of the BFS filler is considered

7 Literature

[1] “3-(Trimethoxysilyl)propyl methacrylate 98% | Sigma-Aldrich”. Accessed September 15, 2016. http://www.sigmaaldrich.com/catalog/product/aldrich/440159?lang=de&region=AT.

[2] Antwi, V. 2010. “Use of monte carlo analysis in life cycle assessment: case study–fruits processing plant in Ghana.” Department of Chemical Engineering, Kwame Nkrumah University of Science and Technology Kumasi-Ghana.

[3] Ayswarya, E. P., K. F. Vidya Francis, V. S. Renju, and Eby T. Thachil. 2012. “Rice husk ash – A valuable reinforcement for high density polyethylene.” *Materials & Design* 41: 1–7.

[4] Bayless, E. R., and Schulz M. S. 2003. “Mineral precipitation and dissolution at two slag-disposal sites in northwestern Indiana, USA.” *Environmental Geology* 45 (2): 252–61. doi:10.1007/s00254-003-0875-1.

[5] “BB412E | Borealis”. Accessed September 02, 2016. http://www.borealisgroup.com/en/polyolefins/products/Others/BB412E/.

[6] “BBC - Standard Grade Bitesize Chemistry - Reactivity of metals : Revision, Page 9”. 2015. Accessed May 17, 2016. http://www.bbc.co.uk/bitesize/standard/chemistry/metals/reactivity/revision/9/.

[7] Biron, M. 2007. *Thermoplastics and Thermoplastic Composites: Technical Information for Plastics Users:* Elsevier Science. https://books.google.at/books?id=g_11KTQ-RjYC.

[8] Biswas, A. K. 1981. *Principles of blast furnace ironmaking: Theory and practice / Anil K. Biswas.* Brisbane, Australia: Cootha.

[9] Bower, D. I. 2002. *An introduction to polymer physics.* Cambridge: Cambridge University Press.

[10] Buttiens, k., J. Leroy, P. Negro, T. Jean-Sebastien, and J. de Lasat. 2015. *The carbon cost of slag production in the blast furnace*.

[11] “Calcium Carbonate Price Per Kg, Calcium Carbonate Price Per Kg Suppliers and Manufacturers at Alibaba.com”. Accessed 08.2016. https://www.alibaba.com/showroom/calcium-carbonate-price-per-kg.html.

[12] Callister, W.D. 2007. *Materials science and engineering: An introduction.* 7th ed. New York: Wiley.

[13] CEAST. 2012. “CEAST® Charpy, Izod, and Tensile Impact Testers.” Accessed September 06, 2016. http://www.ccsi-inc.com/p-impact-ceast-resil-impactor-6956.htm.

[14] Chaijareenont, P., H. Takahashi, N. Nishiyama, and M. Arksornnukit. 2012. “Effect of different amounts of 3-methacryloxypropyltrimethoxysilane on the flexural properties and wear resistance of alumina reinforced PMMA.” *Dent. Mater. J.* 31 (4): 623–28. doi:10.4012/dmj.2012-056.

[15] Chow, J. D., and W. L. Chai. 2008. “Recycling and Application Characteristics of the Fly Ashes from Municipal Solid Waste Incinerator Blended with Waste Polypropylene.” *Environmental Engineering Science* 25 (10): 1497–1506. doi:10.1089/ees.2007.0312.

[16] “Cilas - cumulative particle size determination”. 2015. Accessed September 05, 2016. http://www.particle-size.com/.

[17] “Composite material - Wikiwand”. Accessed August 30, 2016. https://www.wikiwand.com/en/Composite_material.

[18] “Copolymer - Wikiwand”. Accessed August 30, 2016. https://www.wikiwand.com/en/Copolymer.

[19] Das, K., D. Ray, K. Adhikary, N. R. Bandyopadhyay, A. K. Mohanty, and M. Misra. 2010. “Development of Recycled Polypropylene Matrix Composites Reinforced with Fly Ash.” *Journal of Reinforced Plastics and Composites* 29 (4): 510–17. doi:10.1177/0731684408099415.

[20] Drew, L. J., W. H. Langer, and J. S. Sachs. 2002. “Environmentalism and Natural Aggregate Mining.” *Nat. Resour. Res.* 11 (1): 19–28.

[21] Francis, A. A. 2004. “Conversion of blast furnace slag into new glass-ceramic material.” *Journal of the European Ceramic Society* 24 (9): 2819–24. doi:10.1016/j.jeurceramsoc.2003.08.019.

[22] Gendron, R., and D. Binet. 1998. “State of dispersion: Polypropylene filled with calcium carbonate.” *J Vinyl Addit Technol* 4 (1): 54–59. doi:10.1002/vnl.10011.

[23] Giles Jr, H. F., E. M. Mount III, and J. R. Wagner Jr. 2005. *Extrusion: The definitive processing guide and handbook.* PDL handbook series. Norwich, N.Y. William Andrew Pub.

[24] Goedkoop, M., M. I Oele, J. Leijting, T. Ponsioen, and E. Meijer. 2016. *Introduction to LCA with SimaPro*.

[25] “Ground granulated blast-furnace slag - Wikiwand”. Accessed August 30, 2016. https://www.wikiwand.com/en/Ground_granulated_blast-furnace_slag.

[26] Gummadi, J., Kumar, G.V. and Rajesh, G. 2012. “Evaluation of flexural properties of fly ash filled polypropylene composites.” *Int J Mod Eng Res* 2 (4): 2584–90.

[27] Hale, Arthur H., and Kenneth M. Cowan. 1994. *Drilling and cementing with blast furnace slag/silicate fluid:* Google Patents.

[28] Heinrich, Wilhelm M. 1952. *Process for the utilization of blast furnace slag in rotary cement furnaces:* Google Patents.

[29] Hemmings, R. T., R. L. Hill, and B. J. Cornelius. 2007. *Filler comprising fly ash for use in composites:* Google Patents. https://www.google.ch/patents/US7241818.

[30] “Home | worldsteel”. Accessed March 27, 2017. https://www.worldsteel.org/.

[31] Huang, X., J. Y. Hwang, and J. M. Gillis. 2003. “Processed low NOx fly ash as a filler in plastics.” *Journal of Minerals and Materials Characterization and Engineering* 2 (01): 11.

[32] Huang, X., J. Y. Hwang, and J. M. Gillis. 2003. “Processed Low NOx Fly Ash as a Filler in Plastics.” *JMMCE* 02 (01): 11–31. doi:10.4236/jmmce.2003.21002.

[33] Huang, X., J. Y. Hwang, and R. J. Tieder, eds. 1995. *Clean Fly Ash as Fillers in Plastics*.

[34] “Interior | Borealis”. Accessed September 28, 2016. http://www.borealisgroup.com/en/polyolefins/automotive/interior/.

[35] Jablonshi, G. J., ed. 1987. *Fly Ash Utilization as an Extender in Plastics and Paints* 2.

[36] Jahani, Y. 2010. “Dynamic rheology, mechanical performance, shrinkage, and morphology of chemically coupled talc-filled polypropylene.” *J. Vinyl Addit. Technol.* 16 (1): 70–77. doi:10.1002/vnl.20209.

[37] Jenkins, A. D., P. Kratochvíl, R. F. T. Stepto, and U. W. Suter. 1996. “Glossary of basic terms in polymer science (IUPAC Recommendations 1996).” *Pure and Applied Chemistry* 68 (12). doi:10.1351/pac199668122287.

[38] Kamigaito, O., Y. Fukushima, and H. Doi. *Composite material composed of clay mineral and organic high polymer and method for producing the same:* Google Patents 1984. http://www.google.com/patents/US4472538.

[39] Karian, H. G. 2003. *Handbook of polypropylene and polypropylene composites.* 2nd ed., rev. and expanded. Plastics engineering 67. New York: Marcel Dekker.

[40] Katschnig, M. 2010. “Vergleichende Ökobilanzierung von polymerem und herkömmlichem Kopierpapier.” Masterarbeit, Institut füt Kunststoffverarbeitung, Montanuniversitaet Leoben.

[41] Katschnig, M. 2016. “Report: Carbon Footprint Screening: PP/BFS vs. PP/Limestone.” Chair of Polymer Processing, Montanuniversitaet Leoben.

[42] Katschnig, M. 2017. *Polyslag: LCA-related discussions, PCCL, 2017*.

[43] Kim, T.-W., S.-Y. Lee, S.-J. Chun, G.-H. Doh, and K.-H. Paik. 2011. “Effect of silane coupling on the fundamental properties of wood flour reinforced polypropylene composites.” *Journal of Composite Materials* 45 (15): 1595–1605. doi:10.1177/0021998310385589.

[44] Klöpffer, W., and B. Grahl. 2009. *Ökobilanz (LCA), Ein Leitfaden für Ausbildung und Beruf:* Wiley-VCH.

[45] Kohlgrüber, K., and M. Bierdel. 2008. *Co-rotating twin-screw extruders: Fundamentals, technology, and applications.* Munich [Germany]: Carl Hanser Publishers.

[46] Kroese, D. P., T. Brereton, T. Taimre, and Z. I. Botev. 2014. “Why the Monte Carlo method is so important today.” *WIREs Comput Stat* 6 (6): 386–92. doi:10.1002/wics.1314.

[47] Laske, S. 2009. “Synthetisches Kopierpapier auf Basis nachwachsender, polymerer Rohstoffe.” Dissertation, Institute der Kunststoffverarbeitung, Montanuniversitaet Leoben.

[48] Laske, S. 2013. “Maschinen und Anlagen für das Extrudieren.” Lecture by Chair of Polymer Processing, Montanuniversitaet Leoben, 2013. Accessed 06.2016.

[49] Lewis, D. W., ed. 1982. *Properties and uses of iron and steel slags*.

[50] “Life-cycle assessment - Wikiwand”. Accessed June 23, 2016. https://www.wikiwand.com/en/Life-cycle_assessment.

[51] Liu, K., W. Stadlbauer, G. Zitzenbacher, C. Paulik, and C. Burgstaller, eds. 2016. *Effects of surface modification of talc on mechanical properties of polypropylene/talc composites.* AIP Conference Proceedings 1713: AIP conference proceedings and publishing.

[52] Lou, J., and V. Harinath. 2004. “Effects of mineral fillers on polystyrene melt processing.” *J. Mater. Process. Technol.* 152 (2): 185–89. doi:10.1016/j.jmatprotec.2004.03.018.

[53] MacMillan, J. H. 2009. “Using silanes as adhesion promoters.” *Computational Chemistry List, disponivel em< www. ccl. net/cca/documents/MacMillan_Papers/adhesion. pdf>, acesso em* 28 (11).

[54] Mansfeldt, T., and R. Dohrmann. 2004. “Chemical and Mineralogical Characterization of Blast-Furnace Sludge from an Abandoned Landfill.” *Environmental Science & Technology* 38 (22): 5977–84. doi:10.1021/es040002.

[55] Mareri, P., S. Bastide, N. Binda, and A. Crespy. 1998. “Mechanical behaviour of polypropylene composites containing fine mineral filler: Effect of filler surface treatment.” *Composites Science and Technology* 58 (5): 747–52. doi:10.1016/S0266-3538(97)00156-5.

[56] Marinelli, A. L., and R. E. S. Bretas. 2003. “Blends of polypropylene resins with a liquid crystalline polymer. I. Isothermal crystallization.” *J. Appl. Polym. Sci.* 87 (6): 916–30. doi:10.1002/app.11386.

[57] Mark, H. F. 2002. *Encyclopedia of Polymer Science and Technology.* Hoboken, NJ, USA: John Wiley & Sons, Inc.

[58] Mattausch, H., S. Laske, I. Đuretek, J. Kreith, G. Maier, and C. Holzer. 2013. “Investigation of the influence of processing conditions on the thermal, rheological and mechanical behavior of polypropylene nanocomposites.” *Polym Eng Sci* 53 (5): 1001–10. doi:10.1002/pen.23350.

[59] Mauhart, M. 2007. “Auswirkung der Prozesskette Roheisen auf den Baustoff Hochofenschlacke.” Diplomarbeit, Hochschule für Technik, Wirtschaft und Kultur, HTWK Leipzig. Accessed 02.2015.

[60] Meng, M. R., and Q. Dou. 2009. “Effect of Filler Treatment on Crystallization, Morphology and Mechanical Properties of Polypropylene/Calcium Carbonate Composites.” *J. of Macromolecular Sc., Part B* 48 (2): 213–25. doi:10.1080/00222340802566184.

[61] Meyers, R. A. 1987. *Encyclopedia of physical science and technology:* Academic Press.

[62] "Mineral Fillers Improve Plastics". Accessed September 01, 2016. http://machinedesign.com/materials/mineral-fillers-improve-plastics.

[63] Mittal, K. L. 2009. *Silanes and other coupling agents. Vol. 5.* Leiden: VSP.

[64] Mohamed, Heba A. 2011. "Effect of fly ash and silica fume on compressive strength of self-compacting concrete under different curing conditions." *Ain Shams Engineering Journal* 2 (2): 79–86. doi:10.1016/j.asej.2011.06.001.

[65] Mori, T., T. Iwai, A. Yoda, and M. Oshima. 1971. *Method of utilizing blast furnace slag as a strength-improving agent for hardened cement:* Google Patents.

[66] Mostafa, A. 2016. "Report: Statistical analyses for determining the influence of BFS parameters on the mechanical properties of BFS-PP compounds." Polymer Competence Center Leoben GmbH.

[67] "Natural Polymers vs Synthetic Polymers | Starch A Natural Polymer". Accessed May 09, 2016. http://byjus.com/chemistry/differentiate-natural-polymers-from-synthetic-polymers-and-properties/.

[68] Nurdina, A. K., M. Mariatti, and P. Samayamutthirian. 2009. "Effect of single-mineral filler and hybrid-mineral filler additives on the properties of polypropylene composites." *J. Vinyl Addit. Technol.* 15 (1): 20–28. doi:10.1002/vnl.20173.

[69] Nurdina, A. K., M. Mariatti, and P. Samayamutthirian. 2009. "Effect of single-mineral filler and hybrid-mineral filler additives on the properties of polypropylene composites." *J Vinyl Addit Technol* 15 (1): 20–28. doi:10.1002/vnl.20173.

[70] o.V. ecoinvent dataset v3. fullupdate820. The ecoinvent Centre 2015.

[71] Omya. *Our journey towards sustainability, o.V., Omya International AG 2017*.

[72] Omya. *Produktübersicht (Technical Polymers Applications), o.V., 2017*.

[73] Padhi, P. K., A. Satapathy, and A. M. Nakka. 2015. “Processing, characterization, and wear analysis of short glass fiber-reinforced polypropylene composites filled with blast furnace slag.” *Journal of Thermoplastic Composite Materials* 28 (5): 656–71. doi:10.1177/0892705713486142.

[74] Park, B-D, and J. J. Balatinecz. 1997. “A comparison of compounding processes for wood-fiber/thermoplastic composites.” *Polym. Compos.* 18 (3): 425–31. doi:10.1002/pc.10294.

[75] Pattara, C., A. Raggi, and A. Cichelli. 2012. “Life cycle assessment and carbon footprint in the wine supply-chain.” *Environmental management* 49 (6): 1247–58. doi:10.1007/s00267-012-9844-3.

[76] Pertsova, C. C. 2007. *Ecological economics research trends:* Nova Publishers.

[77] Plowman, C., and N. B. Shaw. 1984. *Use of Pulverized Fuel Ash as a Filler in Plastics*.

[78] “Polymer - Wikiwand”. Accessed May 09, 2016. https://www.wikiwand.com/en/Polymer.

[79] Polypropylene. *Environmental Product Declarations of the European Plastics Manufacturers, o.V., Brussels 2008*.

[80] PRe: SimaPro v8.2. PRe 2016.

[81] Premalal, H.G.B., H. Ismail, and A. Baharin. 2003. “Effect of Processing Time on the Tensile, Morphological, and Thermal Properties of Rice Husk Powder-Filled Polypropylene Composites.” *Polymer-Plastics Technology and Engineering* 42 (5): 827–51. doi:10.1081/PPT-120024998.

[82] “Product Carbon Footprints (PCF) and Life Cycle Assessments (LCA)”. Accessed September 07, 2016. http://www.myclimate.org/corporate-clients/software-tools/co2-and-resource-management/product-carbon-footprints-pcf-and-life-cycle-assessments-lca/.

[83] Pustak, A., I. Pucić, M. Denac, I. Švab, J. Pohleven, V. Musil, and I. Šmit. 2013. "Morphology of polypropylene/silica nano- and microcomposites." *J. Appl. Polym. Sci.* 128 (5): 3099–3106. doi:10.1002/app.38487.

[84] Repka, M. A., N. Langley, and J. DiNunzio. 2013. *Melt extrusion: Materials, technology and drug product design.* AAPS Advances in the Pharmaceutical Sciences Series. New York: Springer.

[85] Rothon, R. 2003. *Particulate-filled polymer composites.* 2nd ed. Shrewsbury: RAPRA Technology.

[86] Selvin, T. P., J. Kuruvilla, and T. Sabu. 2004. "Mechanical properties of titanium dioxide-filled polystyrene microcomposites." *Mater. Lett.* 58 (3-4): 281–89. doi:10.1016/S0167-577X(03)00470-1.

[87] Sengupta, S., K. Pal, D. Ray, and A. Mukhopadhyay. 2011. "Furfuryl palmitate coated fly ash used as filler in recycled polypropylene matrix composites." *Composites Part B: Engineering* 42 (7): 1834–39. doi:10.1016/j.compositesb.2011.06.021.

[88] "Silane coupling agents". Accessed September 15, 2016. https://www.shinetsusilicone-global.com/products/type/silanecoup/index.shtml.

[89] Şükrü Yildirim, M., Y. Bíçer, and C. Yildiz. 1996. "Utilization of fly ash and polypropylene wastes in the production of a new porous composite material." *J Porous Mater* 3 (3): 189–91. doi:10.1007/BF01134031.

[90] Sustainability in Plastics. *Calcium Carbonate, o.V., 2009*.

[91] Tadmor, Z., and C. G. Gogos. 2006. *Principles of polymer processing.* 2nd ed., Rev. ed. Hoboken, N.J. Wiley; Chichester : John Wiley [distributor].

[92] The European Slag Association. 2012. "Position paper on the status of ferrous slag: complying with the waste framework directive and the REACH regulation." *Euroslag*.

[93] "The European Slag Association (Euroslag)". Accessed January 25, 2016. http://www.euroslag.com/.

[94] “The European Slag Association (Euroslag)”. Accessed May 17, 2016. http://www.euroslag.com/products/absgbs/.

[95] “The European Slag Association (Euroslag), products”. Accessed May 12, 2016. http://www.euroslag.com/products/.

[96] Tripathi, D. 2002. *Practical guide to polypropylene.* Rapra practical guide series. Shrewsbury: RAPRA Technology.

[97] “Vinylethoxysiloxane homopolymer, 4-7 cSt | Gelest, Inc.” Accessed September 16, 2016. http://www.gelest.com/product/vinylethoxysiloxane-homopolymer-4-7-cst/.

[98] voestalpine Stahl GmbH. “Slag products - Metallurgical materials - Products - Products - voestalpine Steel Division.” Accessed May 12, 2016. http://www.voestalpine.com/stahl/en/Products/Products/Metallurgical-materials/Slag-products.

[99] Wagner, J. R., E. M. Mount, and H. F. Giles. 2014. *Extrusion: The definitive processing guide and handbook.* 2nd ed. Amsterdam: William Andrew.

[100] Wang, Y., and W. C. Lee. 2004. “Interfacial interactions in calcium carbonate-polypropylene composites. 2: Effect of compounding on the dispersion and the impact properties of surface-modified composites.” *Polym Compos* 25 (5): 451–60. doi:10.1002/pc.20038.

[101] Wang, Y., and J.J Wang. 1999. “Shear yield behavior of calcium carbonate-filled polypropylene.” *Polym. Eng. Sci.* 39 (1): 190–98. doi:10.1002/pen.11407.

[102] Weidema. 2013. “Overview and Methodology. Data quality guideline for the ecoinvent database ver-sion 3: Ecoinvent report No. 1 (v3).”.

[103] Weninger, J. 2014. “Orientierende Aufbereitungstechnische Untersuchungen an Hochofenschlacken.” Bachelor of Science thesis II Rohstoffingenieurwesen, Montanuniversitaet Leoben, Lehrstuhl für Aufbereitung und Veredlung. Accessed 01.2016.

[104] Wikipedia. 2016. “Carbon footprint - Wikipedia, the free encyclopedia.” Accessed September 07, 2016. https://en.wikipedia.org/w/index.php?oldid=737908955.

[105] Williams, A.S. 2009. “Life cycle analysis: A step by step approach.”.

[106] Wind, C. 2017. Interview by M. Katschnig. Besprechung Ökobilanz. Leoben, Austria.

[107] Xanthos, M. 2005. *Functional Fillers for Plastics.* Weinheim, FRG: Wiley-VCH Verlag GmbH & Co. KGaA.

[108] Yoon, P. J., D. L. Hunter, and D. R. Paul. 2003. “Polycarbonate nanocomposites: Part 2. Degradation and color formation.” *Polymer* 44 (18): 5341–54. doi:10.1016/S0032-3861(03)00523-8.

[109] Zheng, J. Z., X.P Zhou, J.R Ying, X.L Xie, and Y. W. Mai. 2009. “Enhanced mechanical properties of polypropylene/silica nanocomposites with surface modification of nano-silica via in situ copolymerization of methyl methacrylate and butyl acrylate.” *Chinese J. Polym. Sci.* 27 (05): 685. doi:10.1142/S0256767909004382.

[110] Zheng, J.Z, X.P Zhou, X.L Xie, and Y.W Mai. 2010. “Silica hybrid particles with nanometre polymer shells and their influence on the toughening of polypropylene.” *Nanoscale* 2 (10): 2269–74. doi:10.1039/b9nr00344d.

[111] Zhou, J. P. 2005. “The Surface Modification of ZnOw and its Effect on the Mechanical Properties of Filled Polypropylene Composites.” *Journal of Composite Materials* 39 (21): 1931–41. doi:10.1177/0021998305051809.

8 List of Acronyms

ABS - Acrylonitrile butadiene styrene

ACBS - Air-cooled blast furnace slag

BFS - Blast furnace slag

CFS - Carbon footprint screening

DOC - Degree of crystallinity

DOE - Design of experiments

FFG - The Austrian Research Promotion Agency

GBS - Granulated blast furnace slag

GGBS - Ground granulated blast furnace slag

GHG - Greenhouse gas

HDT - Heat deflection temperature

HIPS - High impact polystyrene

IUPAC - International Union of Pure and Applied Chemistry

LAV-MUL - The Chair of Mineral Processing, Montanuniversitaet Leoben

LCA - Life cycle assessment

LCK-MUL - The Chair of Chemistry of Polymeric Materials - Montanuniversitaet Leoben

LKV-MUL - The Chair of Polymer Processing - Montanuniversitaet Leoben

MCS - Monte Carlo Simulation

MPS - Methacryloxypropyltrimethoxysilane

MSWI - Municipal solid waste incineration

PCCL - The Polymer Competence Center Leoben GmbH

PVC - Polyvinyl chloride

RTD - Residence time distribution

SSE - Single screw extruder

TSC - Twin screw compounding extruder

TSE - Twin screw extruder

VES - Vinylethoxysiloxanehomopolymer silicon

WAXD - Wide-angle X-ray diffraction

WD - Working distance

9 List of Figures

10 List of Tables

11 Appendix

Statistical analyses for experiment 1

The mechanical findings of the three properties (responses)

- Tensile stiffness
- Ultimate strength
- Strain at break

, where fed into the JMP® statistical software, where a full factorial DOE was designed, followed by least square fit analyses and steepest accent optimization (prediction profiler). The aim was to investigate the most significant factors affecting the three responses as well as determining the optimized (highest desirability) combination of factors for maximizing them.

The input of BFS factors, levels and responses into the full factorial design of the JMP® DOE software is shown below.

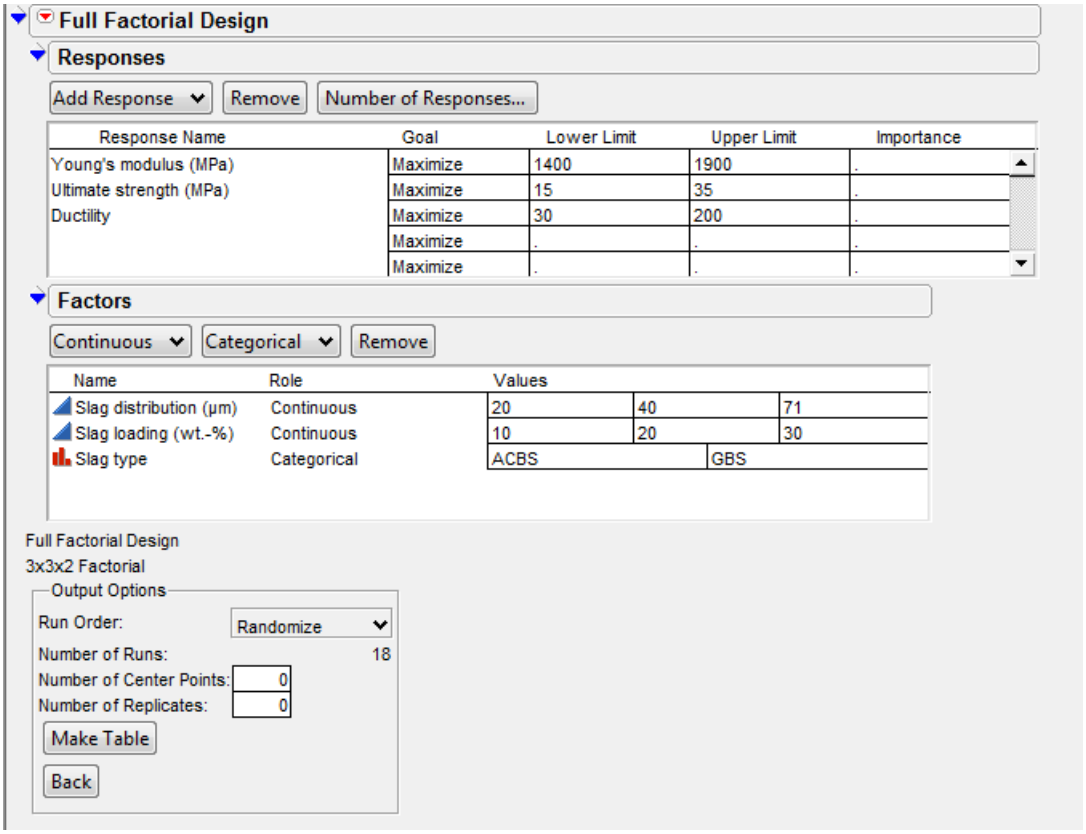

The input of the mechanical findings data into the JMP® software table is shown below.

Mechanical properties table _ full factorial 18 runs

Mechanical properties table
Design 3x3x2 Factorial
Screening
Model

Columns (7/0)
Pattern
Slag distribution (µm) *
Slag loading (wt.-%) *
Slag type *
Ultimate strength (MPa)
Young's modulus (MPa) *
Strain at break (%) *

Rows
All rows 18
Selected 0
Excluded 0
Hidden 0
Labelled 0

	Pattern	Slag distribution (µm)	Slag loading (wt.-%)	Slag type	Ultimate strength (MPa)	Young's modulus (MPa)	Strain at break (%)
1	121	40	20	ACBS	22.0	1669	59
2	132	40	30	GBS	19.9	1818	50
3	131	40	30	ACBS	20.9	1804	47
4	112	40	10	GBS	22.4	1517	72
5	111	40	10	ACBS	23	1429	71
6	122	40	20	GBS	20.6	1684	60
7	311	20	10	ACBS	20.9	1529	193
8	332	20	30	GBS	32.1	1803	127
9	212	71	10	GBS	24.4	1609	100
10	312	20	10	GBS	20.2	1407	122
11	232	71	30	GBS	19.4	1779	37
12	222	71	20	GBS	20.3	1742	69
13	221	71	20	ACBS	21.8	1794	60
14	211	71	10	ACBS	23.6	1605	66
15	331	20	30	ACBS	33.6	1820	89
16	231	71	30	ACBS	20.9	1893	43
17	322	20	20	GBS	34.4	1673	124
18	321	20	20	ACBS	21.9	1678	75

Least square fit analyses

The predicted estimates for the tensile stiffness

The ‘actual by predicted’ plot showing the fitting of the model and the predicted/actual tensile stiffness data.

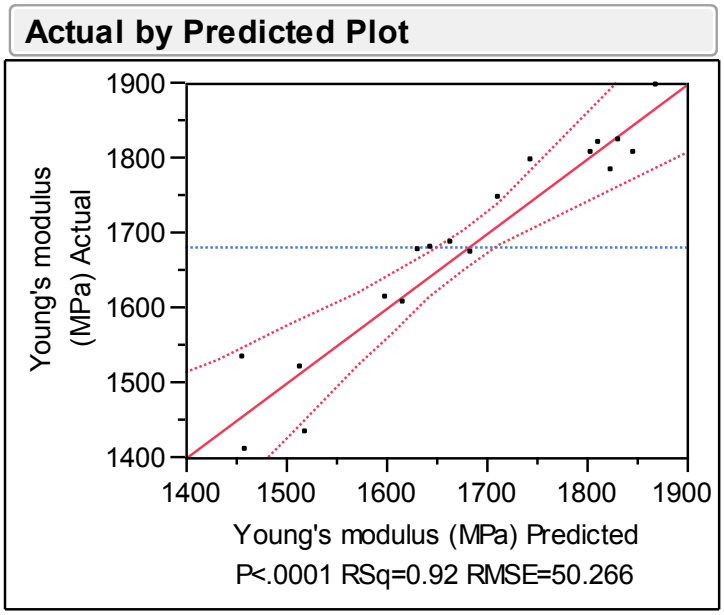

The ‘Pareto plot of estimates’ shows that the significant factor affecting the tensile stiffness was the ‘slag loading’.

Pareto Plot of Estimates

Term	t Ratio
Slag loading (wt.-%)	10.45790
Slag distribution (µm)	3.11862
(Slag distribution (µm)-43.6667)*(Slag loading (wt.-%)-20)	-1.70223
Slag type[ACBS]	0.88624
(Slag loading (wt.-%)-20)*Slag type[ACBS]	0.49964
(Slag distribution (µm)-43.6667)*Slag type[ACBS]	0.32383

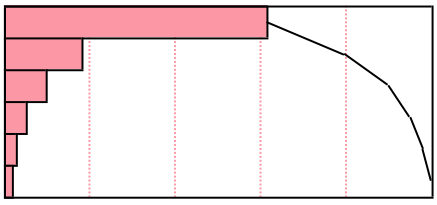

The predicted estimates for the Ultimate strength

The ‘actual by predicted’ plot shows the fitting of the model and the predicted/actual ultimate strength data.

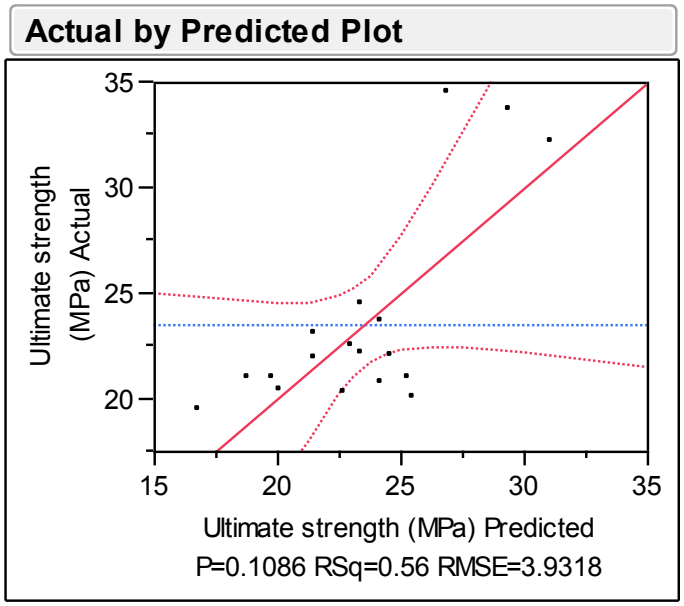

The ‘Pareto plot of estimates’ shows that the significant factors affecting the tensile stiffness were the ‘interaction between the slag loading and distribution’ followed by the ‘slag distribution’.

Pareto Plot of Estimates

Term	t Ratio
(Slag distribution (µm)-43.6667)*(Slag loading (wt.-%)-20)	-2.714766
Slag distribution (µm)	-2.194407
Slag loading (wt.-%)	0.903075
(Slag distribution (µm)-43.6667)*Slag type[ACBS]	0.836867
Slag type[ACBS]	-0.305734
(Slag loading (wt.-%)-20)*Slag type[ACBS]	0.256973

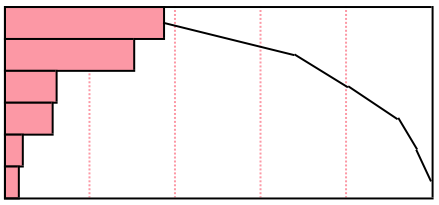

Predicted estimates for the strain at break

The ‘actual by predicted’ plot shows the fitting of the model and the predicted/actual strain at break data, where the large margin of error among the data largely decreased the accuracy of the fit.

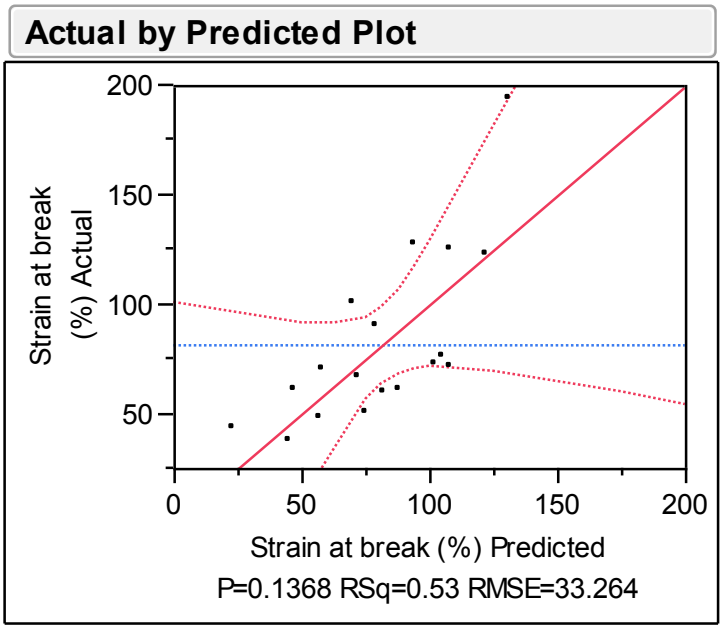

The ‘Pareto plot of estimates’ shows that the significant factors affecting the strain at break were the ‘slag distribution’ followed by the ‘slag loading’.

Pareto Plot of Estimates

Term	t Ratio
Slag distribution (µm)	-2.817557
Slag loading (wt.-%)	-2.004676
(Slag loading (wt.-%)-20)*Slag type[ACBS]	-0.616156
Slag type[ACBS]	-0.410974
(Slag distribution (µm)-43.6667)*Slag type[ACBS]	-0.207470
(Slag distribution (µm)-43.6667)*(Slag loading (wt.-%)-20)	0.066592

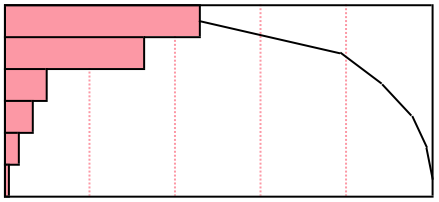

Optimization and prediction profiler analyses

Based on the input findings, the most desirable compound with respect to maximization of the three responses is the ‘30G20’ compound. The interactive profiler also allowed for the prediction of the response value at any possible combination of factors.